APPLICATION OF THE PROPER ORTHOGONAL DECOMPOSITION TECHNIQUES TO AN ANNULAR CASCADE FLOWFIELD

by

Richard L. LeBoeuf

A dissertation submitted to the
Faculty of the Graduate School of State
University of New York at Buffalo
in partial fulfillment of the requirements for the degree of
Doctor of Philosophy

September 1991

Acknowledgements

I would like to thank my wife Bonnie and son Richard for their love, understanding, support, encouragement and sacrifice during the course of my graduate studies. You made me smile in desperate times. I love you.

I thank my faithful mentor Dr. William K. George for his advice, patience and encouragement throughout this work. I am very proud to have been his student. My respect and admiration for him has grown throughout my graduate tenure. His enthusiasm is inspirational; he truly sets the standard as a scientist.

My thanks go to the professors and students who were instrumental in helping me throughout the course of this work including (but not limited to) Dr. W.J. Rae, Dr. C.S. Liu, Dr. D.B. Taulbee, Dr. J.D. Mook, S. Woodward, and J. Sonnenmeier, J. VanOsdol, D. Mollot and E. Graber of SUNY at Buffalo, Dr. M.G. Dunn of Calspan Corp., Dr. M.N. Glauser of Clarkson University and Dr. D.L. Rigby (and Sue), Dr. J. Lee and Dr. L. Tran of Sverdrup Technologies and Dr. A. Shabbir of NASA Lewis Research Center.

I would like to thank Dr. O.P. Sharma of Pratt-Whitney and Dr. R.P. Dring, Dr. M.F. Blair and Dr. H.D. Joslyn of United Technologies Research Center for their help with the development of the windtunnel test section duplication.

I would like to also thank the School of Engineering and Applied Sciences, Engineering Computing Services staff for their invaluable assistance with the data storage and other computational requirements of this study.

I appreciate the financial and emotional support of many members of my family especially my parents: Patricia Healy and Robert LeBoeuf Sr., in-laws: Katherine and Eugene Manning, as well as Dorothy Manning and Bonnie and Clyde Harper. Thanks for opening your homes (and kitchens) in our times of need.

Financial support was obtained through the SUNY at Buffalo, University Teaching and Research Fellowship, the AIAA Gordon C. Oates Air Breathing Propulsion Graduate Scholarship Award and through a grant from the Air Force Office of Scientific Research to the Calspan UB Research Center: "Investigation of Unsteady Flow in an Annular Cascade," Contract No. F49620-87-C-0053.

Contents

List of Figures

Nomenclature

a_i	resistance overheat ratio, dimensionless
$\boldsymbol{A}_i$	derivative of model vector with respect to parameter vector for least squares fit
$A_{l,i}$	polynomial cooling relation parameters $l = 0,1,\ldots$
B_x	stator axial chord, m
C	covariance, $(m/s)^2$
C_p	static pressure coefficient, dimensionless
C_x	mean axial velocity, m/s
d_i	wire diameter, m
$\boldsymbol{D}$	matrix of quadrature weights, s^{-1}
$E_{w,i}$	hot-wire voltage, V
f	frequency, s^{-1}
f_e	frequency limit due to probe spacing, s^{-1}
f_t	frequency limit due to transducer spatial filtering, s^{-1}
$\boldsymbol{f}$	matrix of eigenmodes, dimensionless
$\boldsymbol{F}_i$	angle calibration model vector, dimensionless
FD	full domain (one stator pitch)
h_i	wire heat transfer coefficient, $W/(m^2 \cdot K)$
I	integral scale, s
$\jmath$	square root of -1, dimensionless
$\tilde{k}$	wave number vector, s^{-1} or m^{-1}
k_i	wire i yaw factor, dimensionless
$k_{a,i}$	air thermal conductivity, $W/(m \cdot K)$
$\boldsymbol{K}$	matrix of cross-spectral measurements, $(m/s)^2$
l_s	probe spacing, m
l_t	characteristic transducer size, m
L_i	wire sensor length, m
N	number of angle calibration data pairs
	number of samples per record

N_θ	number of circumferential measurement locations
Nu_i	Nusselt number, dimensionless
OD	outer flow subdomain (excludes the wake region)
p	velocity exponent of polynomial cooling relation
P	airfoil static pressure
	pressure, Pascal
POD	proper orthogonal decomposition
PSD	power spectral density
$\dot{q}_i$	wire heat transfer rate, W/m^2
R	cross-correlation tensor, $(m/s)^2$
	GLSDC relaxation parameter, dimensionless
	Resistance, Ω
Re_i	Reynolds number, dimensionless
S	spectrum, m^2/s
	cross-spectral tensor, m^2/s
t	time, s
T	record length, s
	temperature, K
u	fluctuation of axial velocity component, m/s
	instantaneous velocity, m/s
$\overline{u}$	mean velocity, m/s
U	velocity magnitude, m/s
U_c	characteristic mean velocity, m/s
U_j	velocity component, m/s
$U_{eff,i}$	effective normal velocity magnitude for wire i, m/s
$\vec{U}$	velocity vector, m/s
v	fluctuation of circumferential velocity component, m/s
$\hat{w}_i$	wire orientation unit vector, dimensionless
$\boldsymbol{W}$	angle calibration least squares fit weight matrix, dimensionless
WD	wake subdomain
$\tilde{x}$	spatial coordinate vector, m
X	axial distance from stator leading edge, m
$\boldsymbol{X}_i$	angle calibration parameter vector, dimensionless
$\tilde{y}$	stationary and homogeneous direction coordinate vector, m
$\boldsymbol{Y}_i$	angle calibration measurement vector, dimensionless
α	temperature coefficient of resistivity, K^{-1}

α_j	flow orientation angles with respect to coordinate axes, deg
	POD coefficient, m/s
$\beta_{i,j}$	wire orientation angles with respect to coordinate axes, deg
γ_i	angle between velocity vector and wire i, deg
$\tilde{\gamma}_i$	angle between effective skewed velocity and wire i, deg
$\delta_{p,q}$	Kronecker delta function
$\delta \boldsymbol{Y}_i$	error in least squares model fit, dimensionless
Δf	frequency increment of DFT, s^{-1}
Δt	time increment of digitized signals, s
ϵ	calculus of variations infinitesimal parameter
η	calculus of variations discrepancy from extremum
λ	eigenvalue, $(m/s)^2$
Λ	eigenvalue, m^2/s
ρ	air density, kg/m^3
σ	standard deviation, m/s
τ	time shift of stationary signal, s
	Hermitian matrix eigensystem performance index, dimensionless
ν	air kinematic viscosity, m^2/s
ϕ	eigenfunction, dimensionless
	angle calibration least squares cost function, dimensionless
$\boldsymbol{\Phi}$	eigenmode, dimensionless
$\boldsymbol{\Phi}$	matrix of eigenmodes, dimensionless
ψ	flow coefficient, dimensionless
$\cdot$	arbitrary coordinate vector, m or s

Subscripts

0	at calibration time
1	at inlet measurement plane
	axial
2	at exit measurement plane
	azimuthal
3	radial
a	air
eff	effective normal [velocity]
f	film [temperature]
i	wire designation: 1,2,3

	coordinate direction: 1,2,3
j	coordinate direction: 1,2,3
k	frequency
n	time
old	previous iteration
s	static [pressure]
sa	spanwise averaged
t	total [pressure]
w	wire

Superscripts

(n)	mode
T	transpose
-1	matrix inverse
$*$	complex conjugate
$'$	distinct in time or space

Modifying Marks

$\tilde{}$	vector
	Hermitian matrix eigenvector problem
	skewed [velocity]
$\hat{}$	unit vector
	Fourier transform
$\vec{}$	vector
$\overline{}$	ensemble average

Abstract

The proper orthogonal decomposition (POD) (Lumley 1967) was used to test the hypothesis that there exist a set of functions which characterize a turbine stator exit flowfield and whose dynamics may explain some of the complex behavior in downstream blade rows. The decomposition was applied to three component triple-wire probe measurements of a large-scale annular stator model exit flowfield. This study represents the first application of the orthogonal decomposition to directly measured three component data, and one of the first applications to an applied engineering flow.

The full three-component cross-spectral tensor was produced from simultaneous multi-point triple-wire probe measurements. The measurements were taken across one stator pitch, at the passage midspan, 10% axial chord downstream of the stator trailing edge. The resulting 1089 cross-spectral estimates were then decomposed to obtain the eigenspectra and eigenmodes of the midspan flowfield. In addition, as suggested by Moin and Moser (1989) and George and Glauser (1991), the POD was applied to two subdomains of the passage flowfield in order to increase the convergence rate of the energy representation.

The two subdomains were taken to be the wake and outer flow region because of the large difference in scales between those regions. The wake spanned approximately 20% of the stator pitch at the measurement plane. The decomposition was therefore applied to cross-spectra from 0 to 40% pitch in order to fully capture the wake in the subdomain. The outer flow was decomposed using cross-spectra from 40 to 90% pitch. Five term reconstructions of the power spectral densities (PSD's) were compared to the data in order to gauge the convergence of the expansions.

The first mode of the full domain decomposition represented 25% of the energy of the data

compared to 33% and 17% for the wake and outer flow subdomain first mode energy contributions, respectively. The eigenspectra of the outer flow decomposition were similar to the calculated spectrum of the quasi-homogeneous interior region of the Burgers' equation simulation of Chambers et al. (1988). Consistent with those results was the relatively slower convergence of the PSD reconstructions (four terms to characterize over 50% of the energy). The eigenspectra of the full domain and the subdomain which included the wake region began leveling off at high frequencies (above 200 Hz). This was attributed to the wake contribution to the energy at those frequencies. Contrary to the expected lower frequency/lower mode correspondence (characteristic of the outer flow domain), the wake region was represented at high frequencies by the lowest eigenmodes. The POD modes were so efficient in representing the high frequency energy of the wake region that the behavior of the eigenspectra above mode 4 was similar to the eigenspectra of the outer flow subdomain.

Large distinct low frequency peaks (below 200 Hz) were found in many of the eigenmodes although not consistently at the same frequencies. These peaks were considered the result of either inlet flow disturbances or migration of passage generated flow structures. More detailed measurements are needed however, to determine the nature of the source of these low frequency (apparently large spatial scale) structures.

Chapter 1

Introduction

The flow and heat transfer that occur in a turbine represent one of the most complicated environments seen in a practical machine. The flow is unsteady, transonic, three-dimensional, turbulent, non-isothermal and subject to strong body forces. The principle factor that limits the efficiency of gas turbine engines is the inability of turbine components to withstand high temperatures and large heat transfer rates. Turbine performance is also limited by the aerodynamic losses of the working fluid. Accordingly, attempts to understand, predict, and control these phenomena have played a central role in gas-turbine research.

Satisfactory turbine designs have been achieved due to the development of a sound understanding of the flow and heat transfer mechanisms that define the mean-flow performance and to advances in materials and manufacturing processes. Rising fuel costs and concerns about noise and combustion emissions spurred a flurry of more detailed turbine research activities especially since the early 1980's. Current research activities have been directed at moving beyond the mean-flow mechanics into investigations of the time-dependent aspects of the flow. Some of these aspects lie in the realm of deterministic unsteady fluid mechanics, while others belong to the subject of turbulence.

Examination of the flow through a stationary row of blades has been carried out for a number of blade row geometries, both annular and linear, using a broad range of experimental techniques. These methods have included both qualitative and quantitative measures of the flow. Qualitative

measures have primarily consisted of flow visualization utilizing smoke in the mainstream and oils and other substances on surfaces (summarized by Sieverding 1985). Quantitative measurements have primarily consisted of five and three hole pressure probe measurements of static pressure, total pressure, and mean velocity (examples include Dring et al. (1986), Moustapha et al. (1985), Gregory-Smith and Graves (1983), Moore and Adhye (1985), and Sieverding et al. (1984)). In addition, hot-wire anemometry with single and multiple hot-wire and film probes (for example, Sharma et al. 1985, Hodson 1985, Gregory-Smith and Graves 1983, Gorton and Lakshminarayana 1976 and Raj and Lakshminarayana 1973) and laser-Doppler velocimetry (LDV) (Bailey 1979) have been used to determine flow velocities and Reynolds stresses. The results of the former studies of turbine passage flow have illucidated the non-uniformity and unsteadiness including the production of passage and horseshoe vortices. The appearance of these flow structures results in high loss regions in blade row exit flowfields as illustrated by total pressure loss contours (v. Dring et al. 1986).

To complement the studies of turbine aerodynamics, turbine heat transfer investigations have been carried out by a number of researchers. One of the most important influences on the local heat transfer to a turbine blade or vane is the time-unsteady condition of the flow as it enters the blade row (Graham 1980). A categorization of the different contributions to the unsteadiness was given by Evans (1975) as a separation of the random turbulence from the inherent periodicities of a flowfield. The aggregate affects of such flow unsteadiness on heat transfer has been shown to have a significant effect on the heat transfer through experimental studies using thermocouple instrumented airfoils (e.g. Graziani, et al. 1980 and Blair et al., 1989a,b). Higher resolution turbine rotor heat transfer measurements (Dunn 1986, Dunn et al. 1986 and later Guenette et al. (1989) and Dunn, et al. 1990) clearly demonstrate the importance of the random velocity components to the unsteady heat transfer. It is expected that the flow seen by a given blade would contain the blade passing periodicities (along with its harmonics). However, strong heat transfer signals are seen across a wide frequency spectrum, both above and below that of blade passage.

Even in the absence of viscosity, the pressure fields generated by interactions between rotor and stator blade rows can be expected to produce time varying phenomena whose frequency spectrum

will contain more than harmonics of the blade passing frequency. When viscous effects are added to this picture, even at the level of laminar flow, a wide variety of new time dependent phenomena can be expected which originate from wake and secondary flow generation. These non-uniformities, when cut by a moving blade row propagate downstream carrying with them pressure and velocity distributions of great complexity. The boundary layers which then develop in response to this time dependent outer flow are themselves unsteady, and exhibit phenomena of transition, separation and reattachment (v. Mayle 1991).

The real turbine flowfield contains the additional complexity of turbulence. Any attempt to interpret flowfield measurements on the basis of deterministic frequency content will be inadequate, no matter how faithfully it models the physics of the inviscid and laminar-viscous aspects of the flow. To understand properly what is happening, it is essential to know how the turbulence is generated, how it propagates, and how it modifies the flow. It is possible of course, to apply time averaging and phase locked averaging to identify steady mean and periodic components while identifying the remainder of signals as the contribution to turbulence. This procedure, however, leaves unanswered questions about the turbulence itself, especially regarding its spatial and temporal character.

It was hypothesized at the beginning of this investigation that there exist typical wake and passage flows which possess characteristics important to the rotor dynamics. Thus, applying a technique for identifying the migration and content of coherent structures comprising the turbulence contribution to the overall velocity signals was deemed necessary for a more complete understanding of turbine flowfields. An application of the proper orthogonal decomposition (Lumley 1967) to simultaneous multi-point hot-wire measurements was used to investigate the hypothesized existence of coherent structures in an annular stator exit flowfield.

The application of the Karhunen-Loéve expansion (Loéve 1955) to flowfields was recommended by Lumley (1967) to objectively identify coherent structures. The expansion, referred to as the proper orthogonal decomposition (POD), identifies the coherent structure as the function for which the mean square projection on the field will be maximized. For a field of finite extent and energy, such as the flow analyzed in this study, the POD yields an infinite number of such candidate structures

where each successive mode contains less energy. Therefore, although in general an infinite number of modes result from the POD, a finite (and often small) number of modes is generally sufficient to characterize the flowfield. An exception is that the POD for stationary or homogeneous 'directions' degenerates to a harmonic decomposition where the modes are continuous functions of frequency or wavenumber.

The traditional techniques of identifying coherent flowfield structures include Conditional Averaging (CA) (see Antonia 1981) and Stochastic Estimation (SE) (Adrian 1979). Both CA and SE require a subjective condition on which to base the average or estimate. It is not always apparent what the choice should be and different selections can strongly affect the analysis result. Stochastic Estimation and Conditional Averaging yield an identification of coherent structure whose usefulness is unclear. The identification of coherent structures in fluid flows is useful only if the dynamics of such structures can be determined. Application of Dynamical Systems Theory to the equations resulting from the Galerkin Projection of the POD modes on the Navier Stokes equations has been shown to be a useful tool for determining the dynamics of flow structures (v. Sirovich 1987, Aubry et al. 1988 and Glauser et al. 1989).

The proper orthogonal decomposition has, since Lumley first proposed its use, been applied to pipe flows (Bakewell and Lumley 1967, Herzog 1986), axisymmetric free shear flows (Glauser 1987), and more recently, to the lobed mixing layer flowfield (Ukeiley et al. 1991). The application of the POD to measurements of an annular stator exit flowfield is the subject of this study. It is hoped that this coherent structure identification will result in an increased understanding of the turbine flowfield dynamics.

Applying the POD to experimental data requires the measurement of the cross-correlation tensor. It was originally thought that it would be necessary to use flying cross-wire probes in order to measure the stator exit flowfield without the rectification brought on by the expected high turbulence intensities. The choice of cascade and some preliminary measurements using a stationary cross-wire probe justified the use of stationary probes, since the turbulence intensity was low to moderate. In order to eliminate the cross-flow errors associated with measuring three dimensional flows with

cross-wires, and to measure directly all three velocity components, triple-wire probes were used for this study. The flowfield was traversed with two triple-wire probes in order to measure the three-component cross-correlation tensor. A unique multiple-wire probe calibration technique was developed for the application of the triple-wire probes used for this study and is outlined within.

Chapter 2

Proper Orthogonal Decomposition

2.1 Theory

Lumley (1967) proposed the use of the proper orthogonal decomposition (POD) to objectively identify coherent structures in flowfields. George (1988) provided a useful summary of the application of the POD technique to turbulence. Some of the details applicable to this application are included below.

Formulation of the POD consists of maximizing the mean squared projection of the candidate structures on the flowfield. The normalized projection of a candidate structure $\hat{\phi}$ on the field u is given by the inner product

$$\alpha = \frac{\int \hat{\phi}_i^*(\cdot) u_i(\cdot) d(\cdot)}{[\int \hat{\phi}_j(\cdot) \hat{\phi}_j^*(\cdot) d(\cdot)]^{\frac{1}{2}}} \tag{2.1}$$

where the asterisk denotes the complex conjugate. The subscript (i or j) indicates coordinate direction while the independent variable $(\cdot)$ is a representation of the appropriate spatial or temporal 'location'. The projection is normalized to eliminate amplitude dependence and emphasize instead the degree of projection.

Maximization of the mean squared projection

$$\lambda = \overline{\alpha^2} = \frac{\overline{\int \hat{\phi}_i^*(\cdot) u_i(\cdot) d(\cdot) \int \phi_i(\cdot') u_i(\cdot') d(\cdot')}}{\int \phi_j(\cdot) \phi_j^*(\cdot) d(\cdot)} \tag{2.2}$$

yields the proper orthogonal decomposition (Lumley 1967). Noting that the ensemble average (denoted by the overbar) can be applied directly to the integrand, this equation simplifies to

$$\lambda = \frac{\int\int \phi_i^*(\cdot)\phi_i(\cdot')R_{i,j}(\cdot,\cdot')d(\cdot)d(\cdot')}{\int \phi_j(\cdot)\phi_j^*(\cdot)d(\cdot)} \tag{2.3}$$

where

$$R_{i,j}(\cdot,\cdot') = \overline{u_i(\cdot)u_j(\cdot')} \tag{2.4}$$

is the two-point cross-correlation tensor of the field u.

The Calculus of Variations can be used to achieve the maximization in a straight forward way as outlined in appendix (A). The characteristic eddies represented by the functions ϕ can be found from the resulting integral equation

$$\int R_{i,j}(\cdot,\cdot')\phi_j(\cdot')d(\cdot') = \lambda\phi_i(\cdot). \tag{2.5}$$

This is a homogeneous linear integral equation of the second kind and furthermore for fixed integration limits, (as for experimental data), the equation is referred to as Fredholm's equation in the context of linear integral equation theory (Lovitt 1950).

Since the kernel $(R_{i,j}(\cdot,\cdot'))$ of this integral equation is symmetric, Hilbert-Schmidt theory provides several important properties of the eigenvalues and eigenvectors (Lovitt 1950). The immediately useful of these applications to turbulence study are summarized below (Lumley 1967).

- There are a denumerable set of solutions to Eq. (2.5) (denoted as $\phi_i^{(n)}$ corresponding to the eigenvalues $\lambda^{(n)}, n = 1, 2, \ldots$).

- The set of solutions can be chosen such that the functions $\phi_i^{(n)}, n = 1, 2, \ldots$) are ortho-normal:

$$\int \phi_i^{(p)}(\cdot)\phi_i^{(q)}(\cdot)d(\cdot) = \delta_{p,q}. \tag{2.6}$$

- The vector field u_i can be expressed as a linear combination of the eigenfunctions $\phi_i^{(n)}$ as

$$u_i(\cdot) = \sum a_n\phi_i^{(n)}(\cdot) \tag{2.7}$$

  where the random coefficients given by

$$a_n = \int u_i(\cdot)\phi_i^{(n)*}(\cdot)d(\cdot) \tag{2.8}$$

are uncorrelated (i.e. $\overline{a_p a_q^*} = \lambda^{(n)}\delta_{p,q}$). This representation converges optimally fast in the mean square sense.

- The kernel ($R_{i,j}(\cdot,\cdot')$) can be expressed as a bilinear combination of the eigenfunctions $\phi_i^{(n)}$ as

$$R_{i,j}(\cdot,\cdot') = \sum_n \lambda^{(n)}\phi_i^{(n)}(\cdot)\phi_j^{(n)*}(\cdot') \tag{2.9}$$

which is uniformly and absolutely convergent.

- The eigenvalues are positive, their sum is finite and they may be arrranged in order of their magnitudes, i.e.

$$\lambda^{(n)} \geq 0 \tag{2.10}$$

$$\sum_n \lambda^{(n)} < \infty \tag{2.11}$$

and

$$\lambda^{(1)} > \lambda^{(2)} > \cdots. \tag{2.12}$$

Lumley (1970) referred to the eigenfunctions (or modes) identified through the POD as the characteristic eddies. Subsequent advances in relating the eigenmodes to flowfield dynamics were summarized by George (1988) and Moin and Moser (1989). The significance of the eigenvalues can be found by evaluating the total energy in terms of the field given by Eq. (2.7)

$$\overline{u_i(\cdot)u_i(\cdot)} = \overline{\sum_n a_n\phi_i^{(n)}(\cdot)\sum_m a_m\phi_i^{(m)}(\cdot)}. \tag{2.13}$$

Since the eigenfunctions are orthonormal, this reduces to

$$\overline{u_i(\cdot)u_i(\cdot)} = \sum_n \overline{a_n^2} = \sum_n \lambda^{(n)}. \tag{2.14}$$

Thus the eigenvalues are the energy in the various modes and the sum is the total energy of the field being considered.

2.1.1 Stationary and Homogeneous Directions

Let $\tilde{y}$ represent all the coordinates for which the random vector field is stationary or homogeneous (henceforth referred to as statistically steady (Tennekes and Lumley 1972) for brevity) and let $\tilde{x}$

comprise all the coordinates for which the field is inhomogeneous. In view of these definitions, Eq. (2.5) can be written as

$$\int\int R_{i,j}(\tilde{x},\tilde{x}',\tilde{y}'-\tilde{y})\phi_j^{(n)}(\tilde{x}',\tilde{y}')d(\tilde{y}')d(\tilde{x}') = \lambda^{(n)}\phi_i^{(n)}(\tilde{x},\tilde{y}). \tag{2.15}$$

Note that the expression

$$\int R_{i,j}(\tilde{x},\tilde{x}',\tilde{y}'-\tilde{y})\phi_j^{(n)}(\tilde{x}',\tilde{y}')d(\tilde{y}')$$

in Eq. (2.15) is a convolution integral (Lumley 1970). Taking the Fourier Transform of both sides of Eq. (2.15) and employing the convolution property to transform the convolution integral (v. Oppenheim and Willsky 1983) yields

$$\int S_{i,j}(\tilde{x},\tilde{x}',\tilde{k})\Phi_j^{(n)}(\tilde{x}',\tilde{k})d(\tilde{x}') = \Lambda^{(n)}(\tilde{k})\Phi_i^{(n)}(\tilde{x},\tilde{k}) \tag{2.16}$$

where

$$S_{i,j}(\tilde{x},\tilde{x}',\tilde{k}) = \int R_{i,j}(\tilde{x},\tilde{x}',\tilde{r})e^{-\jmath 2\pi\tilde{k}\cdot\tilde{r}}d(\tilde{r}) \tag{2.17}$$

is the cross-spectral tensor ($\tilde{r} = \tilde{y}' - \tilde{y}$). The solutions $\Phi_i^{(n)}(\tilde{x},\tilde{k})$ to Eq. (2.16) are spectral representations of the original eigenvectors

$$\Phi_i^{(n)}(\tilde{x},\tilde{k}) = \int \phi_i^{(n)}(\tilde{x},\tilde{y})e^{-\jmath 2\pi\tilde{k}\cdot\tilde{r}}d(\tilde{r}). \tag{2.18}$$

and are designated eigenmodes.

The POD has been shown to degenerate to a harmonic decomposition for field directions which are statistically steady. This is consistent with the traditional analysis of homogeneous turbulence using spectral methods. In periodic directions, the Fourier transform reduces to a Fourier series and the spectra would no longer be a continuous function of frequency. The dimensionality of the POD can thus be reduced by first using Fourier analysis in the stationary, homogeneous and periodic directions before solutions in the inhomogeneous directions are pursued.

2.1.2 This Application

The stator exit velocity field cross-correlation measurements were taken at the midspan across one stator pitch. The velocity field was considered stationary in time and inhomogeneous in the azimuthal

direction. Equation. (2.16) was therefore reduced to

$$\int S_{i,j}(\theta,\theta',f)\Phi_j^{(n)}(\theta',f)d\theta' = \Lambda^{(n)}(f)\Phi_i^{(n)}(\theta,f) \tag{2.19}$$

where the frequency f arose from the Fourier transform of the correlation tensor $R_{i,j}(\theta,\theta',t'-t)$ as indicated by Eq. (2.17). Three velocity components were measured at each location so that the indices i and j take on the values 1,2 and 3.

2.2 Numerical Approximation

The discrete nature of experimental data necessitate a numerical approximation to Eq. (2.19). Since the kernel is known for only discrete values of the independent variable, a quadrature rule must be applied to the integral. In addition, digitization of the velocity signals result in a discretization of the spectral tensor. Consequently, the resulting equation for N_θ circumferential locations is

$$\sum_{m=1}^{N_\theta} W_m S_{i,j,k}(\theta_l,\theta_m)\Phi_{j,k}^{(n)}(\theta_m) = \Lambda_k^{(n)}\Phi_{i,k}^{(n)}(\theta_l) \qquad (l=1,\ldots,N_\theta) \tag{2.20}$$

where

$$S_{i,j,k}(\theta_l,\theta_m) = S_{i,j}(\theta_l,\theta_m,k\Delta f) \qquad (k=0,\ldots,N-1). \tag{2.21}$$

is the spectral tensor defined by Eq. (3.9) where Δf is given by Eq. (3.11). For each frequency (indicated by the subscript k), Eq. (2.20) can be written in the nomenclature of matrix eigenvalue problems as (v. Baker 1977)

$$\boldsymbol{KDf} = \Lambda_k \boldsymbol{f} \tag{2.22}$$

where

$$\boldsymbol{K} = \begin{bmatrix} \boldsymbol{S}_{1,1} & \boldsymbol{S}_{1,2} & \boldsymbol{S}_{1,3} \\ \boldsymbol{S}_{2,1} & \boldsymbol{S}_{2,2} & \boldsymbol{S}_{2,3} \\ \boldsymbol{S}_{3,1} & \boldsymbol{S}_{3,2} & \boldsymbol{S}_{3,3} \end{bmatrix} \tag{2.23}$$

$$\boldsymbol{D} = \begin{bmatrix} \boldsymbol{W}_1 & \mathbf{o} & \mathbf{o} \\ \mathbf{o} & \boldsymbol{W}_2 & \mathbf{o} \\ \mathbf{o} & \mathbf{o} & \boldsymbol{W}_3 \end{bmatrix} \tag{2.24}$$

and

$$\boldsymbol{f} = \begin{bmatrix} \boldsymbol{\Phi}_1 \\ \boldsymbol{\Phi}_2 \\ \boldsymbol{\Phi}_3 \end{bmatrix}. \tag{2.25}$$

The submatrices $\boldsymbol{S}_{i,j}$ are $N_\theta \times N_\theta$ matrix representations of the measured spectral tensors $S_{i,j,k}(\theta_l, \theta_m)$. The subvectors $\boldsymbol{\Phi}_j$ are vector representations of the eigenmodes at each of the measurement locations:

$$\boldsymbol{\Phi}_j = \begin{bmatrix} \Phi_{j,k}(\theta_1) & \Phi_{j,k}(\theta_2) & \cdots & \Phi_{j,k}(\theta_{N_\theta}) \end{bmatrix}^T. \tag{2.26}$$

The weight matrix $\boldsymbol{D}$ comprises the submatrices

$$\boldsymbol{W}_j = diag(w_1, w_2, \cdots, w_{N_\theta}) \tag{2.27}$$

which are determined by the choice of quadrature rule used. There are N_θ eigenvalues $\Lambda_k^{(n)}$ and corresponding eigenvectors $\boldsymbol{f}^{(n)}$ satisfying Eq. (2.22).

The success of the approximation of Eq. (2.19) by Eq. (2.22) hinges to a great extent on the choice of quadrature rule (Baker 1977). Since $\boldsymbol{K}$ is Hermitian, choosing a rule with $w_j > 0 \ \forall j$ such that $\boldsymbol{D} > \mathbf{o}$ is advantageous. For although $\boldsymbol{KD}$ is not Hermitian, the matrix $\boldsymbol{D}^{\frac{1}{2}}\boldsymbol{K}\boldsymbol{D}^{\frac{1}{2}}$ is Hermitian and is similar to $\boldsymbol{KD}$. So multiplying both sides of Eq. (2.22) by $\boldsymbol{D}^{\frac{1}{2}}$ yields

$$\tilde{\boldsymbol{K}}\tilde{\boldsymbol{f}} = \Lambda_k \tilde{\boldsymbol{f}} \tag{2.28}$$

where

$$\tilde{\boldsymbol{K}} = \boldsymbol{D}^{\frac{1}{2}}\boldsymbol{K}\boldsymbol{D}^{\frac{1}{2}} \tag{2.29}$$

is a Hermitian matrix, and

$$\tilde{\boldsymbol{f}} = \boldsymbol{D}^{\frac{1}{2}}\boldsymbol{f}. \tag{2.30}$$

The numerical solution of this reformulated problem can exploit the symmetry properties of the Hermitian matrix involved. After obtaining an eigenvector $\tilde{\boldsymbol{f}}$ the desired function, $\boldsymbol{f}$ can be recovered from

$$\boldsymbol{f} = \boldsymbol{D}^{-\frac{1}{2}}\tilde{\boldsymbol{f}}. \tag{2.31}$$

Since $\boldsymbol{D}$ is diagonal, $\boldsymbol{D}^{\frac{1}{2}}$ and $\boldsymbol{D}^{-\frac{1}{2}}$ are easily produced once a quadrature rule has been chosen.

The trapezium quadrature rule with the weights

$$\boldsymbol{W}_j = diag(\frac{\Delta\theta}{2}, \Delta\theta, \ldots, \Delta\theta, \frac{\Delta\theta}{2}) \tag{2.32}$$

was used for the numerical POD application of this study. The azimuthal probe spacing

$$\Delta\theta = \theta_{l+1} - \theta_l \tag{2.33}$$

arises in this context from the numerical approximation of the integral with data at $\Delta\theta$ intervals.

Solution of the Hermitian matrix eigenvalue/eigenvector problem was achieved using the IMSL Inc. subroutine EVEHF. The routine EVEFH can be used to solve for any number (up to the matrix order) of the largest or smallest eigenvalues and their corresponding eigenvectors. Since the modes with the highest energy were of interest in this study, a number of the largest eigenvalues and corresponding eigenvectors were determined. Another IMSL Inc. subroutine, EPIHF, was used to compute the performance index for the complex Hermitian matrix eigensystem after EVEHF was executed. Although the performance index is machine dependent, the eigensystem analysis is considered excellent if the function EPIHF returns a value less than one and good if the performance index is between one and 100 (Smith et al. 1976). When the POD was applied on the data of this study, the performance index was typically less than one and always much less than 100 so the results of the eigensystem analysis were assumed to have reasonable numerical accuracy based on the input data.

Chapter 3

Spectral Analysis

Since the flow is assumed stationary in time, it is appropriate, as discussed in section 2.1.2, to first transform the time series using spectral analysis. The Fourier transform of a signal $u_i(\tilde{x},t)$ is defined as

$$\hat{u}_i(\tilde{x},f) = \int_{-\infty}^{\infty} e^{-\jmath 2\pi f t} u_i(\tilde{x},t)dt. \tag{3.1}$$

Since the Fourier transform of the random signal $u(\tilde{x},t)$ is also random, it is useful examine

$$\overline{\hat{u}_i(\tilde{x},f)\hat{u}_j^*(\tilde{x}',f)} = \int_{-\infty}^{\infty}\int_{-\infty}^{\infty} e^{-\jmath 2\pi f t} e^{\jmath 2\pi f t'} \overline{u_i(\tilde{x},t)u_j(\tilde{x}',t')}dtdt'. \tag{3.2}$$

where the overbar denotes the ensemble average and the asterisk denotes complex conjugation. For stationary processes, the cross-correlation is given by

$$R_{i,j}(\tilde{x},\tilde{x}',\tau) = \overline{u_i(\tilde{x},t)u_j(\tilde{x}',t')} \tag{3.3}$$

where $\tau = t' - t$. Substitution of this expression into Eq. (3.2) yields

$$\overline{\hat{u}_i(\tilde{x},f)\hat{u}_j^*(\tilde{x}',f)} = \int_{-\infty}^{\infty}\int_{-\infty}^{\infty} e^{-\jmath 2\pi f(t'-t)} R_{i,j}(\tilde{x},\tilde{x}',\tau)dtdt'. \tag{3.4}$$

A change of variables to $\xi = t' + t$ and $\tau = t' - t$ transforms the integral to

$$\begin{aligned}\overline{\hat{u}_i(\tilde{x},f)\hat{u}_j^*(\tilde{x}',f)} &= \lim_{T\to\infty}\frac{1}{2}\int_{-T}^{0}\left[\int_{-T-\tau}^{T+\tau} d\xi\right] R_{i,j}(\tilde{x},\tilde{x}',\tau)e^{-\jmath 2\pi f\tau}d\tau + \\ &\lim_{T\to\infty}\frac{1}{2}\int_{0}^{T}\left[\int_{-T+\tau}^{T-\tau} d\xi\right] R_{i,j}(\tilde{x},\tilde{x}',\tau)e^{-\jmath 2\pi f\tau}d\tau.\end{aligned} \tag{3.5}$$

Chapter 4

The Experiment

4.1 Experimental Facility

4.1.1 Windtunnel

The measurements of this study were taken in a newly developed large-scale annular stator cascade windtunnel constructed in the State University of New York at Buffalo, Turbulence Research Laboratory (TRL). The facility (shown schematically in Fig. (4.1) was operated in the open loop suction mode. The nose cone and test section geometry are duplications of the United Technologies Research Center (UTRC) Large Scale Rotating Rig (LSRR) nose cone and first stage stator. The LSRR is a large-scale one and one-half stage turbine model (See Dring et al. 1986 for more details). A duplication of the first stage stator of the LSRR at UTRC was chosen for this study because its large size provides good spatial resolution measurements and because it is heavily documented with both heat transfer and aerodynamic data. The five foot diameter test section contained twenty-two cast epoxy stator airfoils and had a hub-to-tip ratio of 0.8. The nominal operating conditions are summarized in Table (4.1). The vanes accelerate the incoming axial flow through approximately seventy degrees of turning. The six inch annular test section was unobstructed for five axial chord downstream of the airfoils before entering an eight foot long conical annulus leading to a centrifugal blower. The Buffalo Forge Co., BL 730, Class 3 blower was driven by a Wer Industrial, 50 hp dc

motor, controlled with a Fincor, Class 3000, dc Motor Controller.

The blower inlet section was designed to have less than six percent area change overall in order to minimize flow separation. To optimize the blower performance, eighteen straightening vanes were placed at the beginning of the inlet cones and the blower inlet vanes were reversed. The flow exited the tunnel through a straight angle diffuser into the laboratory. To facilitate transducer implementation within the passage, the test section was separable from the conical blower inlet section and both were mounted on wheels on a track. A flexible coupling between the blower and the inlet cones was used in order to minimize blower induced vibrations upstream. A steel cable connection to the floor was used to keep the blower inlet cones from making direct contact with the blower.

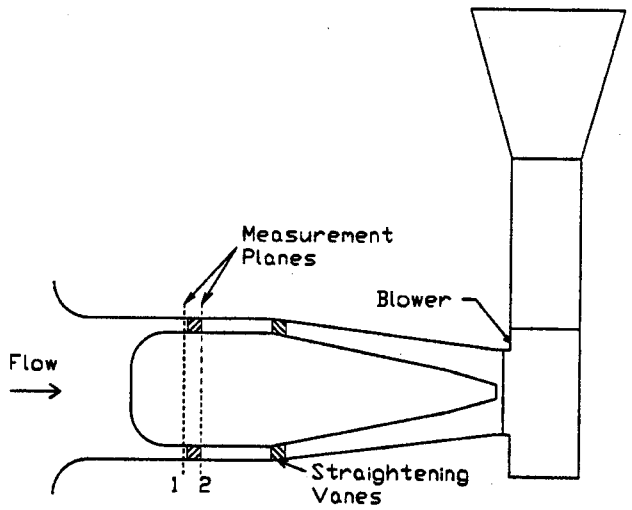

Figure 4.1: Windtunnel schematic (top view).

4.1.2 Probe Traverses

A four inch thick disk equal in diameter to the hub, located two inches downstream of the stator trailing edge was used to traverse the transducers. Two traverses were located on the disk in order to locate two probes within the annulus. One traverse (Traverse 1, Fig. (4.2)) provided only radial probe motion and was fixed to the disk. The second traverse (Traverse 2, Fig (4.2)) provided

Table 4.1: Test Section Geometry and Nominal Operating Conditions

Number of Airfoils	22
Axial Chord	150.6 mm
Aspect Ratio	1.01
Tip Diameter	1.52 m
Hub/Tip Ratio	0.8
Inlet Flow Angle	90.0 deg
Exit Flow Angle	22.5 deg
Average Inlet Velocity	20 m/s
Chord Based Reynolds Number	5.2×10^5

both radial and circumferential probe motion, relative to the disk. The traversing of each of these motions was performed using computer controlled stepper motors. The disk was positioned by hand through a gear box from outside the tunnel. A Litton shaft encoder output was used to infer the circumferential orientation of the disk to within 0.01 degrees. This arrangement of traverses facilitated two-point cross-correlation measurements using two probes. Since Traverse 2 positioning was dependent on Traverse 1 circumferential positioning, circumferential movement of Traverse 1 was added to the Traverse 2 position before relocating Traverse 2. The data collection software was written to account for any such dependencies between traverses so that no motion was repeated for a given pair of probe locations.

4.2 Instrumentation

The triple-wire probes used for this study were molded using techniques similar to those of Ukeiley et al. (1990). Tempered steel music wire with a diameter of 0.020 inches was used as prong material. The prongs were suspended in the mold in order to have an exact match to the probe holder electrical sockets. Two plexiglass mold halves with the cylindrical probe shape machined into them and aluminum end plugs with identical hole patterns for the prong suspension comprised the mold.

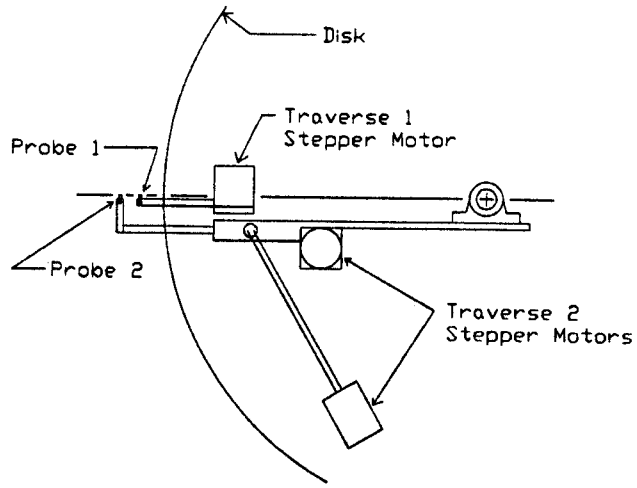

Figure 4.2: Windtunnel probe traversing mechanism.

The probe diameter was offset so that the surface would be flush with the outside of the probe holder when in place (see Fig. (4.4)). A 10 cc syringe was used to inject the epoxy resin (Araldite AW 106/HV 953) into the mold. The probes were removed from the mold in as little as six hours and were hard within a day at room temperature.

After molding, the probe body was tapered on a lathe in order to minimize flow blockage. The prongs were bent approximately 70 degrees to be aligned with the mean stator exit flowfield as shown in Fig. (4.4). To eliminate sensor breakage due to prong vibration (primarily caused by the calibration rig), a sewing thread reinforced epoxy ring (not shown in Fig. (4.4)) was placed around the prongs between the prong ends and the probe body. Alignment of the prongs in the circular pattern shown in Fig. (4.4) after bending was assisted by using an aluminum template with a corresponding circular hole pattern. One of the template surfaces was ground at an angle $\cos^{-1}(1/\sqrt{3})$ ($\simeq 54.7$) degrees relative to the prongs so that it could be used as a guide in grinding the prong ends. Each pair of prongs was ground approximately 0.005 inches shorter than the previous pair so that the overlapping wires would not touch. To insure integrity of the prong bends and grinding, the template was left on the prongs while the epoxy reinforcing ring hardened.

Probe holders were made of gold plated lead sockets (Samtec SC-1W1-GG-1) epoxied within a 1/4

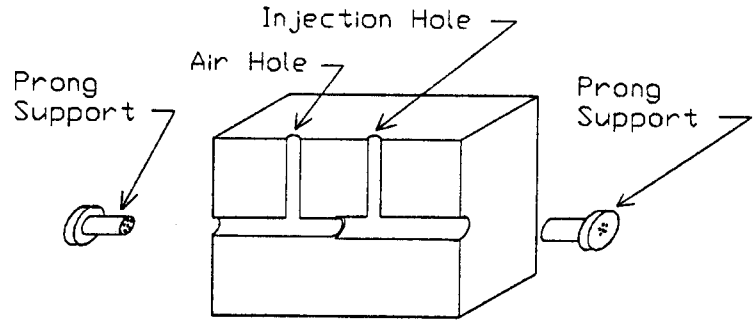

Figure 4.3: Triple-wire probe mold, (mating plexiglass part not shown).

inch diameter brass tube. The lead sockets were permanently co-axial wired to three BNC female bulkhead receptacles mounted on a small rectangular fiberglass plate. The electrically insulating fiberglass plate maintained anemometer ground isolation.

The probes were wired with 6.35 mm long, 5 micron diameter tungsten wires which were copper plated for a sensor length to diameter ratio close to 200. Each hot-wire was operated in the constant temperature mode at an overheat ratio of 0.8 using a DISA 55M01 Main Unit, 55M10 CTA Standard Bridge, and 5m Cable Compansation units. To minimize temperature drift, the anemometer electronics were housed in a chamber maintained within one half degree of 30°C. It was found that the wires did not have consistent constant angle calibrations for typically two days after the initial heating. This anemometer output drift was attributed to relaxation of internal stresses and oxidation of the wires (Fabris 1978). Thus, no wire was used until after it was heated for at least two days, and until constant angle calibrations before and after the two hour long angle calibration were essentially identical. This check, of course, also verified the angle positioning accuracy. The problem of constant angle response drift over time seems to be less important for cross-wire and single wire probes but common for triple-wire probes. It is suspected that the short duration of the calibration of single- and cross-wire probes precludes noticing response drift except when recalibrations during

and after measurements are compared to previous calibrations.

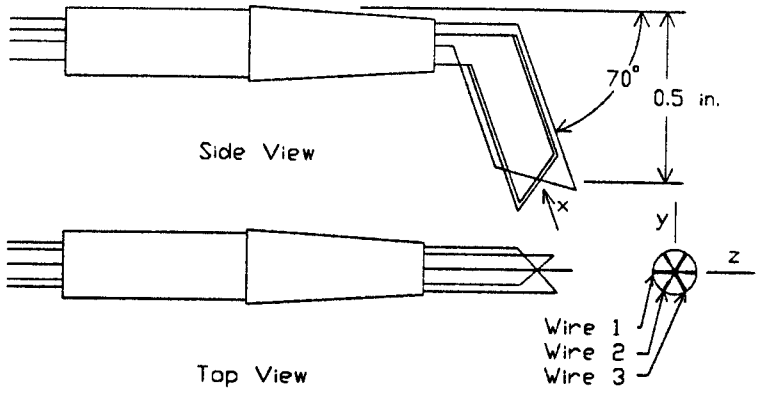

Figure 4.4: Triple-wire probe schematic.

The velocity of the calibration jet was inferred from the plenum pressure using Bernoulli's equation. The pressure was digitized from a Validyne DP103-14 pressure transducer and Model CD23 Carrier Demodulator. The pressure transducer was calibrated against a Meriam Instrument Co., Model 34FB2, micromanometer which has an accuracy of 0.001 inch of water. The calibration jet and test gas operating temperatures were measured using the digitized output of a Chromel-Alumel thermocouple with an ice water reference junction. The thermocouple output was amplified for digital recording using an Analog Devices, Model 2B5A4, Four Channel Isolated Thermocouple/mV Conditioner which had a maximum gain of 1000. The thermocouple was calibrated versus a mercury thermometer. Both the pressure transducer and the thermocouple calibrations were represented by a least squares fit to a quadratic equation and were verified repeatable over the course of weeks of measurements.

All digitized data were recorded using a SUN Microsystems minicomputer via a Phoenix Data Inc., simultaneous sample and hold, 15 bit A/D system after analog filtering using phase matched 8-pole Bessel low-pass anti-aliasing filters manufactured by Frequency Devices (v. Glauser 1987). To eliminate the problem of ground loops, the analog ground of all devices was connected to one

source via a bank of isolated ground electrical receptacles.

4.3 Sampling Criteria

The A/D used for this study had a maximum sampling rate of 325 KHz which, when divided by the number of channels to be sampled, yields the maximum sampling rate of any of the channels. Using two triple-wire probes, a pressure transducer and a thermocouple limited the sampling frequency to just above 40 KHz. The acceptability of this limited sampling frequency was investigated via consideration of the physical limitations imposed by the flow and probe geometry.

The probe dimensions set a restriction on the frequencies of the flow fluctuations due to their spatial filtering. The smallest spatial scale resolvable by a probe is twice the spatial dimensions of the transducer. This imposes a limit on the frequencies resolvable by the probe of

$$f_t = \frac{U_c}{2l_t} \tag{4.1}$$

where U_c is the characteristic mean convective velocity, and l_t is the characteristic transducer size. In this experiment, $l_t \simeq 2$ mm and $U_c \simeq 55$ m/s. This would suggest that the measurements should be low-pass filtered with a 13.8 KHz cutoff frequency before recording due to the limited probe spatial resolution.

Similar to the time scale associated with transducer spatial filtering is that associated with multiple-probe measurements of eddies. The spatial extent of the eddies simultaneously sensed by two probes is determined by the probe spacing (l_s) and the characteristic mean convection velocity (U_c). Assuming the turbulence field is effectively "frozen" as it passes the probes, the minimum eddy time-scale resolvable by both probes is given by

$$\frac{1}{f_e} = \frac{l_p}{U_c} \tag{4.2}$$

where f_e is the associated maximum frequency. For this experiment the apparatus limited the spacing to 1.4 cm. Thus the maximum resolvable flow frequency was reduced to approximately 3.9 KHz.

Preliminary measurements using one triple-wire probe, at 60 KHz while filtering at 25 KHz were used to determine the extent of the energy content at high frequencies. It was found that below 5 KHz, the spectra had approximately one decade of -5/3 character. Above 5 KHz there was broadband noise which was identified to be a combination of prong and/or wire vibration and electronic noise at 12 KHz and 16 KHz. The proposed frequency limit set by the minimum probe spacing was deemed acceptable and so the anti-aliasing filters were set to cut-off at 4 KHz. In order to more than satisfy the Nyquist criterion, a 10 KHz sampling frequency was then used.

The record length and number of blocks were determined from the integral scale and the statistics required for the ensuing analysis (v. George et al. 1978). The integral scale

$$I = \int_0^\infty r(\tilde{x}, \tau) d\tau \tag{4.3}$$

can be expressed in terms of the correlation coefficient

$$r(\tilde{x}, \tau) = \frac{C(\tilde{x}, \tau)}{\sigma^2} \tag{4.4}$$

where

$$C(\tilde{x}, \tau) = \overline{[u(\tilde{x}, t) - \overline{u}][u(\tilde{x}, t+\tau) - \overline{u}]} \tag{4.5}$$

is the covariance and

$$\sigma^2 = C(0) = \overline{[u(\tilde{x}, t) - \overline{u}]^2} \tag{4.6}$$

is the variance of the signal $u(\tilde{x}, t)$. Combining Eqs. (4.4) and (4.3) yields

$$I = \frac{\int_0^\infty C(\tilde{x}, \tau) d\tau}{\sigma^2} \tag{4.7}$$

For experimental data, it is convenient to calculate the integral scale from the spectrum

$$S(\tilde{x}, f) = \int_{-\infty}^{\infty} C(\tilde{x}, \tau) e^{-j2\pi f \tau} d\tau \tag{4.8}$$

which is the Fourier transform of the correlation. Since $C(\tilde{x}, \tau)$ is even and real, the spectrum is also even and real, so that Eq. (4.8) reduces to

$$S(\tilde{x}, f) = 2 \int_0^\infty C(\tilde{x}, \tau) \cos 2\pi f \tau d\tau \tag{4.9}$$

Since $S(0)$ is exactly twice the integral in Eq. (4.7), the integral scale can be written in the form

$$l = \frac{S(\tilde{x}, 0)}{2\sigma^2} \tag{4.10}$$

The spectrum of the digitized experimental data was found using Eqs. (3.8) and (3.9) as outlined in Chapter (3). The spectrum at the origin was extrapolated from the first two points of the spectrum since the dc value was zero for the spectrum of the fluctuations $(u(\tilde{x}, t) - \overline{u})$.

The resulting evaluation of Eq. (4.10) yielded an integral scale of approximately 0.6 ms. Thus recording 1024 samples per record at 10 KHz results in over 100 integral scales per record. Waiting one record length between blocks insured statistical independence of the ensembles. In reality, the processing of each block increased the interblock temporal spacing to several record lengths.

The accuracy of measurements of statistical quantities such as spectra are dependent on the number of ensembles used for the estimate. The second order statistics required for the POD implementation can be estimated with good accuracy using 300 or more blocks (v. George et al. 1978 and Tan-atichat and George 1985). In light of the computational requirements, the spectral estimates derived in this study were ensemble averages of 300 individual spectra.

4.4 Hot-Wire Implementation

Calibration of cross and triple-wire probes is commonly performed in two parts: a normal wire calibration of each wire and a subsequent angle calibration. The normal wire calibration consists of a measurement of the wire voltage for many (typically twenty or more, v. Swaminathan, Rankin and Sridhar 1984) velocities normal to the wire for each wire. A response equation such as a version of King's Law (King 1914, Sidall and Davies 1972) or a polynomial (George et al. 1987) is fit to normal wire calibration data. The angle calibration data consists of measurements of wire voltages for a large range of velocity directions (at a number of velocity magnitudes for low speed applications). The angle calibration voltage data is then converted, via the normal response equation, to effective normal velocities. The yaw (and sometimes pitch) parameters of an angle response equation (such as Jorgenson's, (1971) or a cosine law (Hinze 1959) are then determined using a regression technique.

The usual multiple-wire calibration techniques using the aforementioned procedure require the wire angles to be known *a priori*. Mutually orthogonal wires are often assumed in order to have an analytical decoding algorithm for triple-wire probes. Orthogonality of cross-wires need not be assumed in order to have an analytical decoding scheme, however. The errors incurred by calibrating non-orthogonal triple-wire probes using the response equations assuming mutually orthogonal wires may exceed 10% (Lekakis et al. 1989). Successful calibration of non-orthogonal triple-wire probes has been achieved using sophistocated curve fits (Butler and Wagner 1983) and iterative solutions to Jorgenson's equations (Lekakis et al. 1989). The analyses discussed by these researchers also requires prior knowledge of the wire angles.

The wire angles of commercially available probes are given only to some known tolerance by the manufacturers, and independently made or repaired probes have unknown wire angles. Determination of flow-wire orthogonality is consequently determined using optical techniques or maximization of the anemometer voltage for a given velocity. A calibration method which determines wire angles and yaw factors, without the use of normal wire calibrations, would eliminate a source of error and save time.

A calibration method for multiple-wire probes which determines wire angles and yaw factors, without the use of normal wire calibrations was developed. This improved calibration technique, eliminates the error associated with either wire measurements or assumed wire orthogonality. Additionally, this new method saves time since a constant angle calibration can be performed on all wires at once in lieu of the traditional normal wire calibrations of each wire. The development of such a calibration using the modified cosine law (Hinze 1959) is outlined below.

4.4.1 Response Equations

The wire orientations can be expressed in terms of the direction cosines in cartesian coordinates as

$$w_i = \cos\beta_{i,1}\,i + \cos\beta_{i,2}\,j + \cos\beta_{i,3}\,k. \tag{4.11}$$

Similarly, the normalized velocity is given by

$$\frac{\vec{U}}{U} = \cos\alpha_1 i + \cos\alpha_2 j + \cos\alpha_3 k. \tag{4.12}$$

Taking the dot product of the wire orientation and the normalized velocity yields an expression for the angle between the flow and each wire orientation (γ_i) given by

$$\cos\gamma_i = \sum_{j=1}^{3} \cos\alpha_j \cos\beta_{i,j}. \tag{4.13}$$

For low speed flows ($U < 5m/s$) the yaw sensitivity of a hot-wire is largely velocity dependent (Beuther et al. 1987), and due to the increased relative effect of the prongs for low speed applications, the pitch sensitivity of the wires comprising the probe is significant (Jorgenson 1971). For high speed flow applications however, the yaw sensitivity of a hot-wire is virtually independent of velocity and the pitch sensitivity is negligible. Thus for high speed flows (for which the calibration described below was used), Jorgenson's (1974) equations reduce to the modified cosine law of Hinze (1959). Thus, the angle calibration required for the analysis presented herein can be performed at a velocity magnitude representative of the application flow speed. The modified cosine law for each wire can be expressed as

$$\left(\frac{U_{eff,i}}{U}\right)^2 = 1 + (k_i^2 - 1)\cos^2\gamma_i \tag{4.14}$$

where $U_{eff,i}$ is the effective normal velocity of wire i and γ_i is the angle between wire i and the instantaneous velocity. The yaw factor k_i account for heat transfer due to the velocity component along the wire.

Substitution of Eq. (4.13) into Eq. (4.14) yields the angle response equation

$$\left(\frac{U_{eff,i}}{U}\right)^2 = 1 + (k_i^2 - 1)\left(\sum_{j=1}^{3} \cos\alpha_j \cos\beta_{i,j}\right)^2. \tag{4.15}$$

Traditional measurements of normal wire and yaw calibration data can be used to determine (via, for example, a Least Squares optimization) the yaw factors (k_i) and the wire orientation angles ($\beta_{i,j}$). This was the approach used by LeBoeuf and George (1990) for cross-wire probes and LeBoeuf (1990) for triple-wire probes. However without prior knowledge of the wire angles and since the implementation flow should never be normal to any of the wires (since it would typically be at too

high a yaw angle on other wires) it is advantageous to use constant angle calibrations at known probe angles without assuming orthogonality to each wire.

The final derivation of the response equations requires the use of a normal wire response equation such as King's Law (King, 1914) or the more general polynomial (v. George et al., 1987):

$$Re_i^{\frac{1}{n}} = \sum_{l=0}^{m} A_{l,i} Nu_i^{\frac{1}{2}} \tag{4.16}$$

where, for best accuracy (Beuther 1980), the Reynolds number

$$Re_i = \frac{U_{eff,i} d_i}{\nu} \tag{4.17}$$

is evaluated at the ambient temperature (T_a) and the Nusselt number

$$Nu_i = \frac{h_i d_i}{k_{a,i}} \tag{4.18}$$

is evaluated at the film temperature ($T_{f,i} = \frac{T_a + T_{w,i}}{2}$, $T_{w,i}$ = wire operating temperature). The heat transfer coefficient (h_i) can be eliminated from the Nusselt number in terms of the wire voltage $E_{w,i}$ since

$$h_i = \frac{\dot{q}_i}{(T_{w,i} - T_a)\pi d_i L_i} \tag{4.19}$$

and

$$\dot{q}_i = \frac{E_{w,i}^2}{R_{w,i}}. \tag{4.20}$$

The Nusselt number can then be expressed as

$$Nu_i = \frac{E_{w,i}^2}{\pi R_{w,i} L_i k_{a,i} (T_{w,i} - T_a)} \tag{4.21}$$

where

$$R_{w,i} = \text{resistance} \tag{4.22}$$

$$d_i = \text{diameter} \tag{4.23}$$

$$L_i = \text{length} \tag{4.24}$$

and

$$k_{a,i} = \text{thermal conductivity of air at the film temperature} \tag{4.25}$$

of wire i. The kinematic viscosity (ν) is, as noted above, evaluated at the ambient temperature.

The unknown wire temperature ($T_{w,i}$) can be eliminated from Eq. (4.21) in terms of known quantities. For constant temperature anemometry (CTA), the wire temperature ($T_{w,i}$) (and consequently resistance ($R_{w,i}$)) is constant. The resistance overheat ratio is given by

$$a_i = \frac{R_{w,i} - R_{w_0,i}}{R_{w_0,i}} \tag{4.26}$$

where $R_{w_0,i}$ is the wire resistance at the setup ambient temperature ($T_{a,0}$). The wire resistance can be expressed to a first approximation as

$$R_{w,i} = R_{w_0,i}[1 + \alpha(T_{w,i} - T_{a,0})] \tag{4.27}$$

in terms of the temperature coefficient of resistivity (α). Combining Eqs. (4.26) and (4.27) and solving for the wire resistance yields

$$T_{w,i} = \frac{a_i}{\alpha} + T_{a,0}. \tag{4.28}$$

Substitution of Eqs. (4.17), (4.21) and (4.28) into Eq. (4.16) yields

$$\left(\frac{U_{eff,i}d_i}{\nu}\right)^p = \sum_{l=0}^{m} A_{l,i}\left[\frac{E_{w,i}^2}{\pi R_{w,i}L_i k_{a,i}(\frac{a_i}{\alpha} + T_{a,0} - T_a)}\right]^{\frac{l}{2}}. \tag{4.29}$$

The constant wire geometry parameters (d_i and L_i) and the wire resistance ($R_{w,i}$) can be factored into the polynomial parameters such that the normal wire response equation reduces to

$$(U'_{eff,i})^p = \sum_{l=0}^{m} A'_{l,i}\,(E'_{w,i})^l \tag{4.30}$$

where

$$U'_{eff,i} = \frac{U_{eff}}{\nu} \tag{4.31}$$

$$E'_{w,i} = \frac{E_{w,i}}{[k_{a,i}(\frac{a}{\alpha} + T_{a,0} - T_a)]^{\frac{1}{2}}} \tag{4.32}$$

and

$$A'_{l,i} = \frac{A_{l,i}}{d_i^p}(\pi R_{w,i}L_i)^{\frac{l}{2}}. \tag{4.33}$$

A fourth order polynomial with p equal to 0.5 has been found to be consistent with the normal wire data obtained at the Turbulence Research Laboratory (TRL) and hence has been used for this study.

Combining Eq. (4.30) and Eq. (4.15) and solving for U/ν yields

$$\frac{U}{\nu} = \frac{\left[\sum_{l=0}^{m} A'_{l,i} \left(E'_{w,i}\right)^l\right]^{\frac{1}{p}}}{[1 + (k_i^2 - 1)(\sum_{j=1}^{3} \cos\alpha_j \cos\beta_{i,j})^2]^{\frac{1}{2}}}. \tag{4.34}$$

Calibration measurements taken with the flow at a constant angle relative to the probe (represented by $\alpha_j = \tilde{\alpha}_j$ = constant) can be fit to

$$\left(\tilde{U}'_{eff,i}\right)^p = \sum_{l=0}^{m} \tilde{A}'_{l,i} \left(E'_{w,i}\right)^l \tag{4.35}$$

where

$$\tilde{A}'_{l,i} = \frac{A'_{l,i}}{[1 + (k_i^2 - 1)(\sum_{j=1}^{3} \cos\tilde{\alpha}_j \cos\beta_{i,j})^2]^{\frac{l}{2}}} \tag{4.36}$$

and

$$\tilde{U}'_{eff,i} = \frac{\tilde{U}_{eff,i}}{\nu}. \tag{4.37}$$

The effective *skewed* (instead of normal) velocity, $\tilde{U}_{eff,i}$ is the velocity magnitude at the angle

$$\tilde{\gamma}_i = \sum_{j=1}^{3} \cos\tilde{\alpha}_j \cos\beta_{i,j} \tag{4.38}$$

with respect to the wire, which would give the same wire response voltage as the true velocity.

The relationship between the effective normal velocity and the effective skewed velocity can be derived by combining Eqs. (4.30), (4.35) and (4.36):

$$U_{eff,i} = \tilde{U}_{eff,i}[1 + (k_i^2 - 1)(\sum_{j=1}^{3} \cos\tilde{\alpha}_j \cos\beta_{i,j})^2]^{\frac{1}{2}}. \tag{4.39}$$

The final angle response equation can be found by substituting Eq. (4.39) into Eq.(4.15) and rearranging to get

$$\left(\frac{\tilde{U}_{eff,i}}{U}\right)^2 = \frac{1 + (k_i^2 - 1)\left(\sum_{j=1}^{3} \cos\alpha_j \cos\beta_{i,j}\right)^2}{1 + (k_i^2 - 1)\left(\sum_{j=1}^{3} \cos\tilde{\alpha}_j \cos\beta_{i,j}\right)^2}. \tag{4.40}$$

The calibration parameters in this equation include in addition to the yaw factor (k_i), the wire direction cosines ($\beta_{i,j}$). The data required for such a calibration consist of constant angle calibration data (analogous to normal wire data) and yaw angle calibration measurements which are described in a later section.

If the fluid temperature is assumed constant, then the coefficients of Eq. (4.30) would absorb the temperature dependent factors of Eqs. (4.31) and (4.32) and all primed quantities except $A'_{l,i}$

in the preceding analysis would be equal to their unprimed counterparts. A common argument for assuming isothermal flow is that the test flow is left running long before beginning the experiment so that thermal equilibrium is reached. Caution is recommended regarding such an assumption however, since the calibration flow (whether in the test facility or a separate calibration facility) is probably not at the same temperature as the test flow during the experiment. In this study for example, the calibration jet temperature was found to be a function of both the blower running time and the blower speed and would vary by as much as 2°C over the course of a single constant angle calibration.

To exemplify the potential problems regarding an isothermal calibration assumption, a small set of constant angle calibration measurements were recorded and fit with Eq. (4.35) and with the polynomial response equation

$$U_{jet}^{\frac{1}{2}} = \sum_{l=0}^{4} A_l E_w^l \tag{4.41}$$

for isothermal flow. The calibration set was unusual since the blower speed was increased between half of the data points and without shutting down, decreased between the second half of the data points. For the same jet velocity, the temperature of the airstream was higher for the second half of the calibration data than for the first half of the data. The results of a least squares fit to Eq. (4.41) is shown in Fig. (4.5). The effect of the jet temperature change resulted in curve fit errors up to 3.8%. The least squares fit of Eq. (4.35) for the same data is shown in Fig. (4.6) with a maximum error of 1.2%. The collapse of the data is remarkably good, contrary to some researchers condemnation of relationships between Nusselt and Reynolds numbers for practical hot-wire use (Bruun 1979). The assumption of isothermal flow was therefore not used for this study and Eq. (4.35) was used to model the wire voltage response to the effective skewed velocity.

4.4.2 Parameter Optimization

The optimized calibration parameters based on the method of Least Squares are determined by minimizing the functions

$$\phi_i = (\boldsymbol{Y}_i - \boldsymbol{F}_i(\boldsymbol{X}_i))^T \boldsymbol{W} (\boldsymbol{Y}_i - \boldsymbol{F}_i(\boldsymbol{X}_i)) \tag{4.42}$$

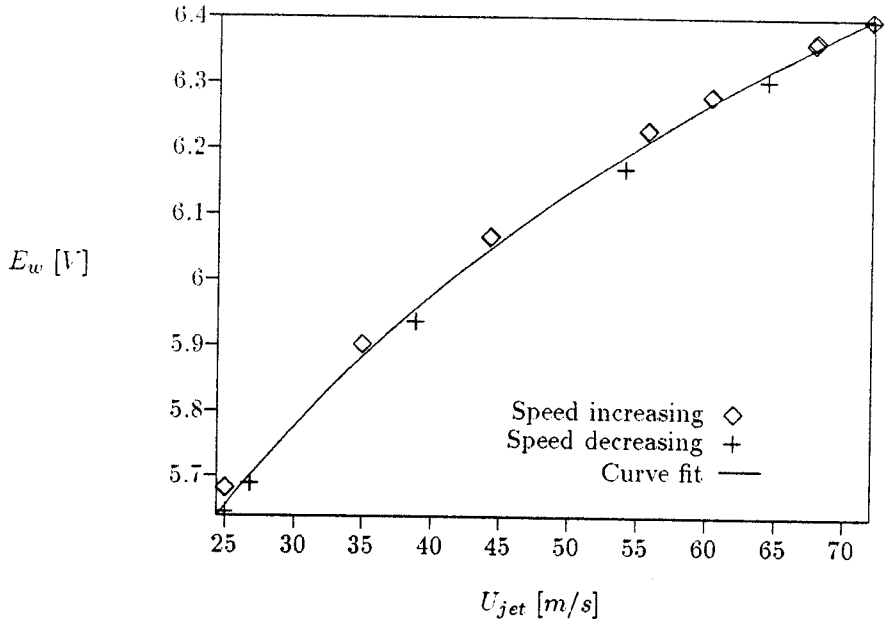

Figure 4.5: Sample constant angle response assuming the jet temperature is constant.

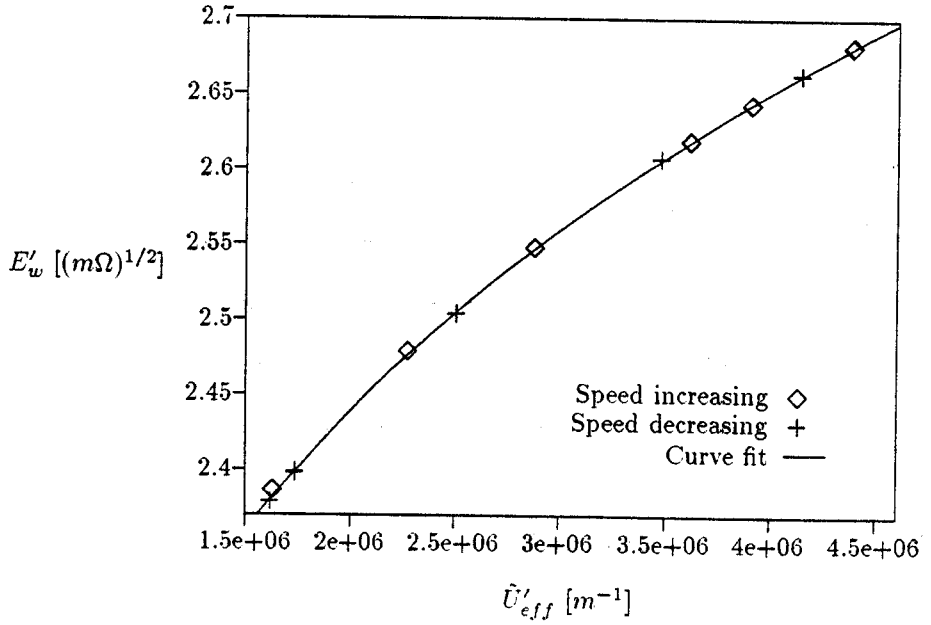

Figure 4.6: Sample constant angle response without isothermal jet assumption.

for each wire i. The superscript T indicates transpose. For the wire angles to be physically consistent the direction cosines of each wire orientation must satisfy

$$\sum_{j=1}^{3} \cos^2 \beta_{i,j} = 1. \tag{4.43}$$

This constraint was applied numerically by including it with the N data pairs in the definitions of $\boldsymbol{Y}_i$ and $\boldsymbol{F}_i$ such that

$$\boldsymbol{Y}_i = \begin{bmatrix} \left(\frac{\tilde{U}_{eff_{i,1}}}{U}\right)^2_1 \\ \vdots \\ \left(\frac{\tilde{U}_{eff_{i,1}}}{U}\right)^2_N \\ 1 \end{bmatrix} \tag{4.44}$$

and

$$\boldsymbol{F}_i = \begin{bmatrix} \left(\frac{1+(X^2_{i,4}-1)(\sum_{j=1}^{3} \cos\alpha_j X_{i,j})^2}{1+(X^2_{i,4}-1)(\sum_{j=1}^{3} \cos\tilde{\alpha}_j X_{i,j})^2}\right)_1 \\ \vdots \\ \left(\frac{1+(X^2_{i,4}-1)(\sum_{j=1}^{3} \cos\alpha_j X_{i,j})^2}{1+(X^2_{i,4}-1)(\sum_{j=1}^{3} \cos\tilde{\alpha}_j X_{i,j})^2}\right)_N \\ \sum_{j=1}^{3} X^2_{i,j} \end{bmatrix} \tag{4.45}$$

which is a function of the parameter vector

$$\boldsymbol{X}_i = \begin{bmatrix} \cos\beta_{i,1} \\ \cos\beta_{i,2} \\ \cos\beta_{i,3} \\ k_i \end{bmatrix} \tag{4.46}$$

for each wire i. A diagonal weight matrix ($\boldsymbol{W}$) is appropriate for this application. The first N entries of $\boldsymbol{W}$ can in general be set to unity. To deweight high uncertainty data however, the corrresponding weight can be set lower. In order to numerically apply the constraint of Eq. (4.43), the last entry of $\boldsymbol{W}$ can be set larger than the weighting of the data. Unity constraint weighting was found to be sufficient however, so that in general the weight matrix can be set equal to the identity matrix.

If the data and model vectors are redefined to be

$$\boldsymbol{Y}_i = \begin{bmatrix} 1 \\ \vdots \\ 1 \end{bmatrix} \tag{4.47}$$

and

$$\boldsymbol{F}_i = \begin{bmatrix} \left(\frac{U}{U_{eff,i}}\right)^2_1 \left(\frac{1+(X^2_{i,4}-1)(\sum_{j=1}^{3}\cos\alpha_j X_{i,j})^2}{1+(X^2_{i,4}-1)(\sum_{j=1}^{3}\cos\tilde{\alpha}_j X_{i,j})^2}\right)_1 \\ \vdots \\ \left(\frac{U}{U_{eff,i}}\right)^2_N \left(\frac{1+(X^2_{i,4}-1)(\sum_{j=1}^{3}\cos\alpha_j X_{i,j})^2}{1+(X^2_{i,4}-1)(\sum_{j=1}^{3}\cos\tilde{\alpha}_j X_{i,j})^2}\right)_N \\ \sum_{j=1}^{3} X^2_{i,j} \end{bmatrix} \tag{4.48}$$

respectively, then a minimization of the sum squared relative error is performed. This was deemed more appropriate since it produces a more uniform fit for a larger range of flow angles.

The non-linear Least Squares data fit defined by Eq. (4.42) through (4.46) (or Eqs. (4.46) through (4.48) can be solved by Gaussian Least Squares Differential Correction (GLSDC) (see for example Junkins, 1987). The complexity of the optimization, however, necessitates the use of a gradient search prior to applying GLSDC if the initial parameter vector deviates too much from the optimum. The following iteration comprises the GLSDC calculation.

$$\boldsymbol{X}_i = (\boldsymbol{A}_i^T \boldsymbol{W} \boldsymbol{A}_i)^{-1} \boldsymbol{A}_i^T \boldsymbol{W} \delta \boldsymbol{Y}_i + \boldsymbol{X}_{i,old} \tag{4.49}$$

where

$$\boldsymbol{A}_i = \frac{\partial \boldsymbol{F}_i}{\partial \boldsymbol{X}_i} \Big|_{\boldsymbol{X}_{i,old}} \tag{4.50}$$

and

$$\delta \boldsymbol{Y}_i = \boldsymbol{Y}_i - \boldsymbol{F}_i \Big|_{\boldsymbol{X}_{i,old}} . \tag{4.51}$$

The superscript -1 indicates matrix inversion. The parameter vector $\boldsymbol{X}_{i,old}$ must be initialized to perform the first iteration and subsequently is the result of the prior iteration.

Due to the extreme nonlinearity of the response function, Eq. (4.49) resulted in an increase in the cost function (Eq. (4.42)) for some values of $\boldsymbol{X}_{i,old}$. To overcome such an increase, the iterative correction to $\boldsymbol{X}_i$ was relaxed as illustrated by Eq. (4.52).

$$\boldsymbol{X}_i = R(\boldsymbol{A}_i^T \boldsymbol{W} \boldsymbol{A}_i)^{-1} \boldsymbol{A}_i^T \boldsymbol{W} \delta \boldsymbol{Y}_i + \boldsymbol{X}_{i,old} \tag{4.52}$$

The relaxation parameter (R) was decrease by a factor of two until the cost function decreased for a given $\boldsymbol{X}_{i,old}$, then update of the parameter vector was performed.

4.4.3 Calibration Procedure

Calibration measurements were performed with the probe at the exit of a 1 inch diameter low turbulence (Tu = 0.35%) open jet (See Glauser 1987) which was capable of producing flows up to at least 75 m/s. All required probe orientations were set using computer controlled stepper motors. A calibration rig was built (See Fig. (4.7)) to provide rotation of the probe holder in two directions. The probe was rotated in the probe holder/flow plane (Motor 1) and independently about the probe holder axis (Motor 2). The uncertainty in the angle measurements was estimated to be 0.1 degrees. One block of 1000 voltages were sampled at 1 KHz and averaged to obtain each calibration voltage.

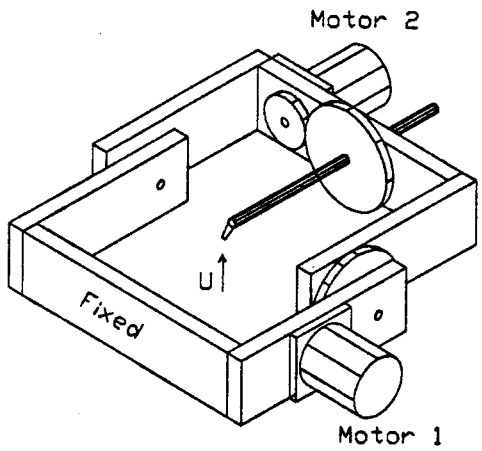

Figure 4.7: Computer controlled calibration rig.

To carry out the constant angle calibration, it is recommended that the probe be oriented in the implementation mean flow direction and the calibration be performed on all the wires at once. The flow was oriented along the x axis (see Fig. (4.4)) and at least 35 velocity/voltage pairs over the velocity range 25 m/s to 75 m/s were recorded for each constant angle calibration. Following George

et al. (1987), a fourth order polynomial response equation was used to relate the wire voltages to the effective skewed velocities (Eq. (4.35). The kinematic viscosity (ν) and thermal conductivity ($k_{a,i}$) required for the evaluation of $\tilde{U}'_{eff,i}$ (via Eq. (4.37)) and $E'_{eff,i}$ (via Eq. (4.32)) were obtained using a quadratic interpolation at the measured air or film temperature. The tabulated properties used for the interpolation were those of Touloukian et al. (1975) and Touloukian. et al. (1970). The parameters of the calibration ($\tilde{A}'_{0,i}, \ldots, \tilde{A}'_{4,i}$) were determined for each wire i using a linear least squares fit. Typically the wires used for this study had maximum constant angle calibration curve fit errors less than 0.5%.

For high velocity applications (the topic of this paper), the yaw angle calibration consists of recording the voltage of each wire for a number of probe orientations while the probe is exposed to a flow representative of the maximum application velocity. Angle calibration data was obtained with the probe exposed to nearly constant (but not assumed so) velocity flow at approximately 60 m/s. The probe was rotated about the probe holder and swept through the probe holder/flow direction plane in 5 degree increments. For each probe orientation, the jet velocity and the wire voltages were recorded. The resulting 124 measurement directions are indicated on Fig. (4.8) as a plot of $\frac{U_3}{U_1}$ versus $\frac{U_2}{U_1}$ in which a circle of radius $\tan 30^o$ ($\simeq 0.6$) would encompasses all velocity vectors within a 30 degree cone aligned with the x axis. The angle calibration data was used in conjunction with the constant angle response to obtain values of $\tilde{U}_{eff,i}/U$ which were modeled by Eq. (4.40) as described above.

An exemplary angle calibration curve fit of a wire is shown in Fig. (4.9) as $\left(\frac{\tilde{U}_{eff,i}}{U}\right)^2$ versus $\cos^2\gamma_i$ ($= (\sum_{j=1}^{3} \cos\tilde{\alpha}_j \cos\beta_{i,j})^2$) with the curve fit of Eq. (4.40) for one wire. The response represented in this form is a straight line with slope

$$\frac{k_i^2 - 1}{1 + (k_i^2 - 1)\left(\sum_{j=1}^{3} \cos\tilde{\alpha}_j \cos\beta_{i,j}\right)^2} \tag{4.53}$$

and intercept

$$\frac{1}{1 + (k_i^2 - 1)\left(\sum_{j=1}^{3} \cos\tilde{\alpha}_j \cos\beta_{i,j}\right)^2}. \tag{4.54}$$

The curve fit shown had an average error of 1.6% with a maximum error of 6% which was typical of

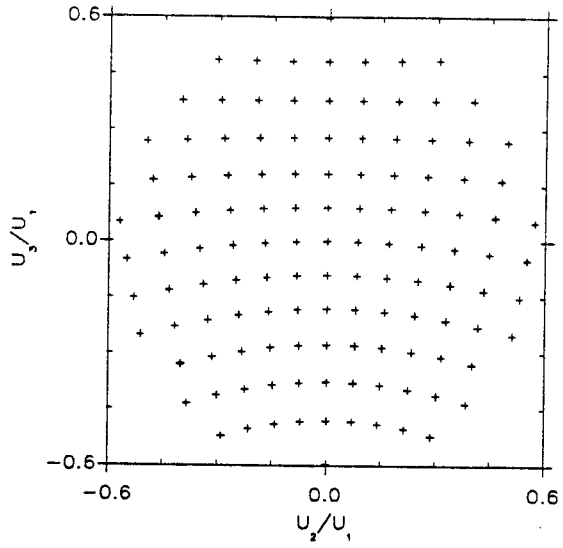

Figure 4.8: Distribution of angle calibration data.

all wires used for this study. The Least Square optimal curve fits were typically achieved with less than ten iterations for eight significant digits of accuracy of the parameters. The initial calibration parameter values included yaw factors equal to 0.15 and orthogonal wire orientations corresponding to the geometry shown in Fig. (4.4). The higher errors at low values of $\cos^2\phi$ are due to the neglected pitch sensitivities at the larger flow angles. This reinforces the desirability of effective skewed velocity calibrations instead of the typical normal-to-wire calibrations since the normal wire calibrations are subject to more prong interference.

Webster (1962) found that typical yaw factors for heated wires in a low speed cross flow are typically 0.2 ± 0.01. Champagne (1967) later determined using a velocity range of 7-35 m/s that the yaw factor strongly depends on the length to diameter ratio ($\frac{l}{d}$). For platinum wires with $\frac{l}{d} = 200$, the yaw factor was equal to 0.2. The yaw factors in the range of 0.2 to 0.3 for the tungsten wires ($\frac{l}{d} = 200$) used on the probes for this work were considered consistent with those studies.

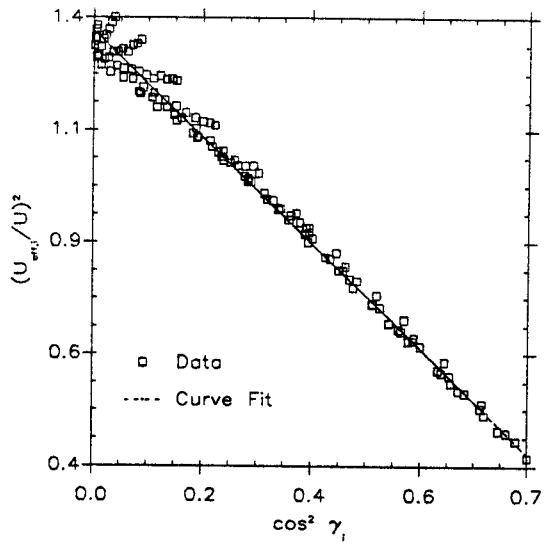

Figure 4.9: Angle calibration curve fit.

4.4.4 Triple-Wire Decoding

Determination of the velocity components based on given wire voltages can be achieved by solving Eq. (4.16) for the effective normal velocities and subsequently Eq. (4.15) subject to the constraint

$$\sum_{j=1,3}^{3} \cos^2 \alpha_j = 1 \tag{4.55}$$

for the velocity magnitude (U) and angles (α_1, α_2, and α_3). The nonlinear set of Eq. (4.15) and (4.55) can be simplified by multiplying each equation by U^2, eliminating U^2, and noting that $U_j = U \cos \alpha_j$. Performing these operations and rearranging yields the following equation

$$(k_i^2 - 1)(\sum_{j=1}^{3} U_j \cos \beta_{i,j})^2 + \sum_{j=1}^{3} U_j^2 - U_{eff,i}^2 = 0 \tag{4.56}$$

for each wire i, which can be solved for the three velocity components. To obtain the squared effective normal velocity $U_{eff,i}^2$ from measurements, Eqs. (4.32), (4.35), (4.37) and (4.39) are combined to yield

$$U_{eff,i}^2 = \nu^2 \left\{ \sum_{l=0}^{m} \tilde{A}_{l,i}^{l} \left(\frac{E_{w,i}}{[k_{a,i}(\frac{a}{\alpha} + T_{a,0} - T_a)]^{\frac{1}{2}}} \right)^l \right\}^{\frac{2}{r}} [1 + (k_i^2 - 1)(\sum_{j=1}^{3} \cos \tilde{\alpha}_j \cos \beta_{i,j})^2] \tag{4.57}$$

where all quantities on the right hand side are known once measurements of $E_{w,i}$ are aquired.

The nonuniqueness of the solutions to the nonlinear equation set (4.56) (examined in detail by Lekakis et al. (1989)) can be overcome by orienting the probe in the mean flow direction such that the velocity vector fits within a cone containing only one solution to these equations. This overcomes the ambiguity associated with the axisymmetry of the wires. Requiring the flow to remain within a certain range of angles of course limits the turbulence intensities acceptable during implementation. The problem of rectification (the mapping to the presumed solution quadrant of velocities outside that quadrant) has been studied by Andreopoulos (1983). Andreopoulos (1983) determined, using simulated data, that a reasonable limit for the turbulence intensity is 30% in order to minimize the statistical effects of rectification. The flow under consideration here had a maximum turbulence intensity well below the 30% proposed bound.

Successive approximation was demonstrated for Jorgenson's equations (1971) in essentially the form of Eq. (4.56) by Andreopoulos (1983). Successive approximation was determined to be an unstable solution technique for this application however, even with the coordinate axes oriented such that the velocity components were all the same sign (as suggested in private communication). In fact, several methods of successive substitution were attempted only to prove ustable also. Because of its stability, Newton's method was implemented for the solution of Eq (4.56). Typically three or four iterations were required to achieve four decimal (five or six digit) accuracy when the last velocity components were used as the initial iterate.

Chapter 5

Preliminary Measurements

Preliminary measurements were performed in order to establish the average flow conditions in the newly developed windtunnel. Time averaged inlet and exit flowfield and airfoil surface static pressures were included in these measurements. Inlet flow measurements consisted of average streamwise velocity at eleven spanwise locations at each of four pitchwise locations. A cross-wire probe was used to perform unsteady two component velocity measurements of the exit flowfield. The cross-wire measurements were used to determine the spatial distribution of Reynolds stresses and local turbulence intensity. The exit flowfield was also traversed with a five-hole pressure probe over one vane pitch in order to measure total pressure, static pressure, and velocity.

5.1 Inlet Flowfield

The time averaged streamwise velocity measurements were obtained with a single hot-wire in a plane 23% axial chord upstream of the stator leading edge at 11 spanwise locations for each of four pitchwise locations. The results, normalized by the mean streamwise velocity have been plotted as spanwise distributions in Fig. (5.1). The inlet flow was found to be nearly uniform over approximately sixty percent of the span at each of the four pitch locations. The hub boundary layer was less than five percent of the span while the shroud boundary layer appears to include ten percent of the span. This difference in boundary layer thickness is due to the significantly longer shroud entrance

duct compared to the hub nose cone development length (see Fig. (4.1)). The short inlet duct and lack of flow conditioners upstream of the test section is apparently responsible for the differences between the velocity distributions shown in Fig. (5.1) and those reported by Dring et al. (1986). The measurements of Dring et al. (1986) at the same locations relative to the airfoil leading edge plane are nearly uniform over approximately ninety percent of the span at each pitch location and do not intersect as the results of this study indicate. In spite of these differences in the spanwise distributions of streamwise velocity, the spanwise averaged streamwise velocities plotted in Fig. (5.2) along with the results of Dring et al. 1986) indicate identical trends but different magnitudes.

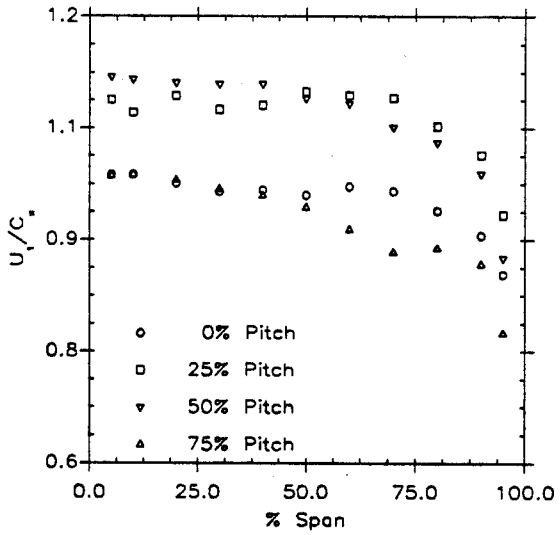

Figure 5.1: Spanwise distribution of time averaged streamwise velocity.

5.2 Exit Flowfield

5.2.1 Cross-Wire

Unsteady two component velocity measurements were performed using a cross-wire probe at 10 spanwise locations at each of 11 pitchwise locations at the exit of the test section. The cross-wire

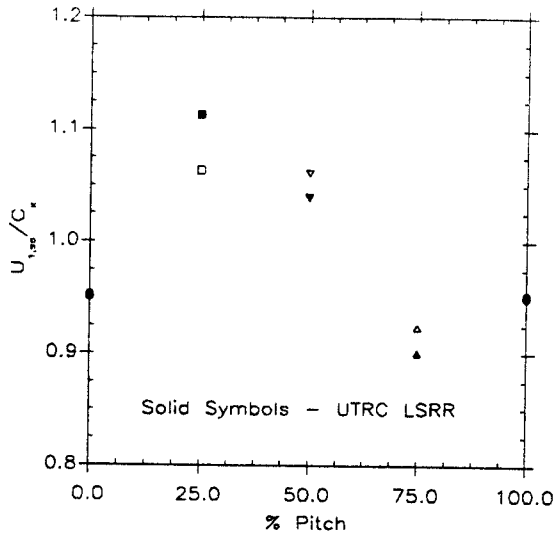

Figure 5.2: Spanwise averaged streamwise velocities.

calibration, instrumentation and implementation was outlined by LeBoeuf and George (1990). The orientation of the wires in the circumferential/axial plane resulted in the neglect of the radial velocity component. The local turbulence intensity distribution is shown in Fig. (5.3). The distributions of axial and azimuthal Reynolds stresses normalized by the square of the mean axial velocity are presented in Figs. (5.4) and (5.5), respectively. Clearly discernable are the high turbulence (or apparent turbulence) and high Reynolds stresses in the wake and hub/suction surface corner regions. The triple-wire probe measurements described in Section (6.1) corroborate these findings. In spite of the difference in the inlet conditions, these results resemble those of Sharma et al. (1985) in which the Reynolds stresses and turbulence intensities were measured in the UTRC LSRR using a three element hot-film probe.

5.2.2 Five-Hole Probe

A United Sensors DC-120 five-hole pressure probe was used survey the exit flowfield in a plane 10% axial chord downstream of the stator trailing edge. The probe was used in the non-nulled mode using the methods outlined by Treaster and Yocum (1979). A complete description of the five-hole probe calibration was given by Treaster and Houtz (1986) and the data reduction was outlined fully

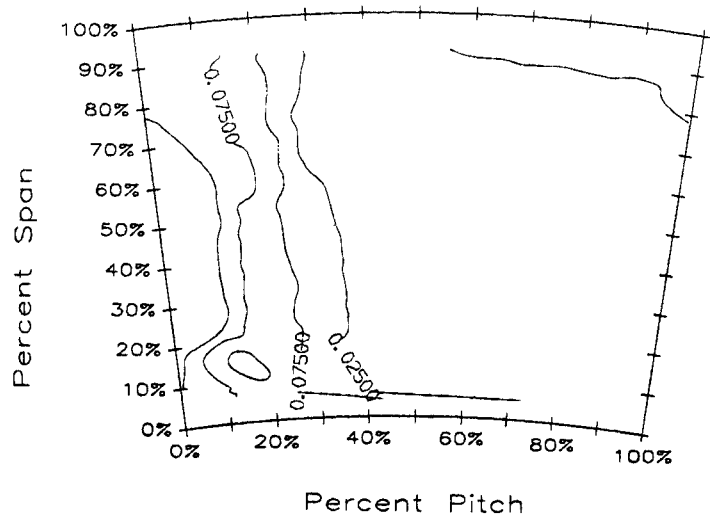

Figure 5.3: Local turbulence intensity distribution.

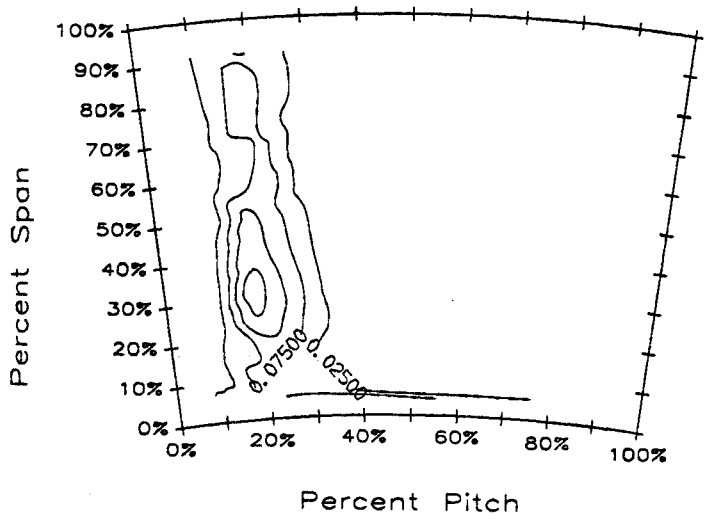

Figure 5.4: Axial Reynolds stress distribution: $\frac{\overline{u^2}}{C_f^2}$.

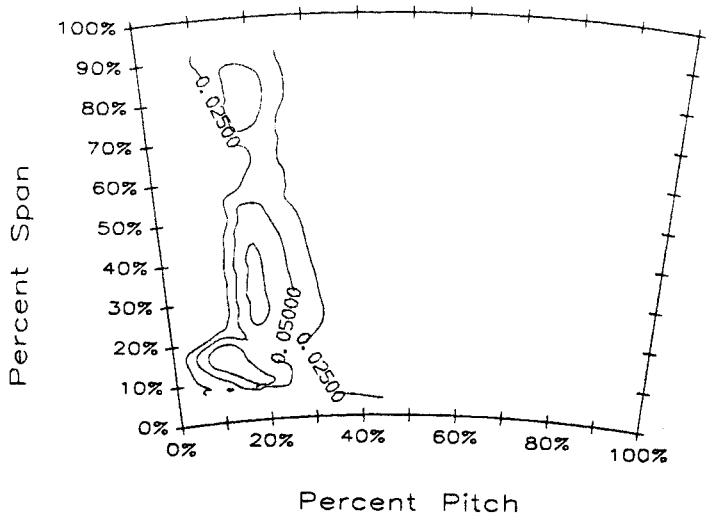

Figure 5.5: Azimuthal Reynolds stress distribution: $\frac{\overline{v'^2}}{C_x^2}$.

by Welz (1986).

The measurement locations encompassed a grid of 11 pitchwise locations by 9 spanwise locations at the exit of one vane passage. Due to probe geometry, the measurements were limited to the lower 80% of the span. The results of the exit plane measurements are shown in Figs. (5.6) through (5.12) in the form of plots of exit lateral velocities, lateral secondary flow velocities, pitch angle contours, yaw angle contours, and static pressure contours, respectively. The view in all of these figures is from downstream toward upstream with trailing edges at the left and right margins. Thus the flow exits the vanes from left to right as shown in the lateral velocity plot (Fig. (5.6)) which includes only the radial and azimuthal components of the exit velocity. Note that an extension of the vane mean camber line at any blade cross-section intersects the measurements plane just beyond 20% of the passage pitch in the azimuthal direction from the left side of the plots; ie. just beyond the third pitchwise measuring location.

Small scale variations from the spatially averaged flow can be determined by subtracting from the radial and azimuthal velocity components, the mean flow in those directions. The result of doing so is the lateral secondary velocity plot shown as Fig. (5.7). The most striking feature of Fig. (5.7) is the strong inward radial component of velocity in the wake region where the centrifugal force on

the relatively low velocity fluid cannot compensate for the pressure gradient from the hub to the tip. The large negative pitch angle regions in the pitch angle contours of Fig. (5.8) coinciding with the wake region also clearly indicate the inward tendency of the flow in that region. This phenomena has been reported by Sieverding et al. (1984) to occur even 68% axial chord downstream of the trailing edge in a similar cascade. Another noteworthy feature of the lateral secondary velocity plot (Fig. (5.7)) is the large negative offset in the third pitchwise measurement location values. This appears in spite of the moderate yaw angle of the flow in that region (approximately the exit metal angle; see Fig. (5.9)). It is due instead to the low velocity in that region as seen in Fig. (5.10).

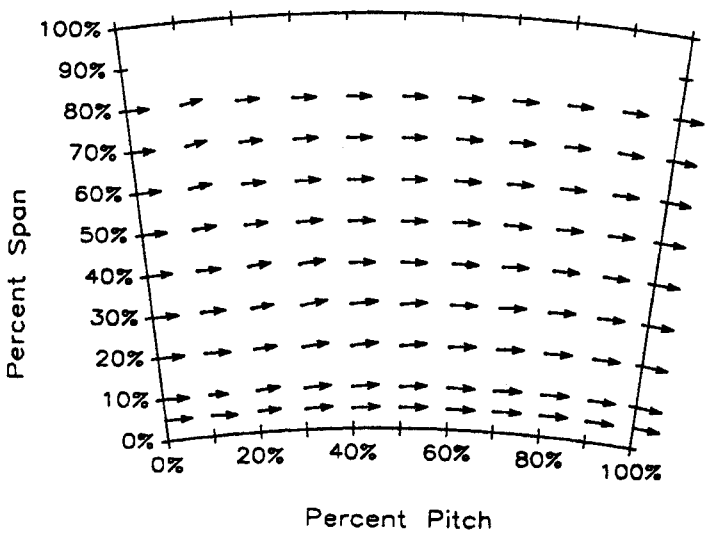

Figure 5.6: Exit lateral velocity field.

The velocity magnitude normalized by the average axial velocity is provided in the contour plot of Fig. (5.10). A low velocity region appears in the vane wake as well as in the hub/suction side corner of the passage. Although the inlet flow is significantly different than the flow established in the UTRC LSRR, the results still resemble the findings of Sharma et al. (1985) where, using a

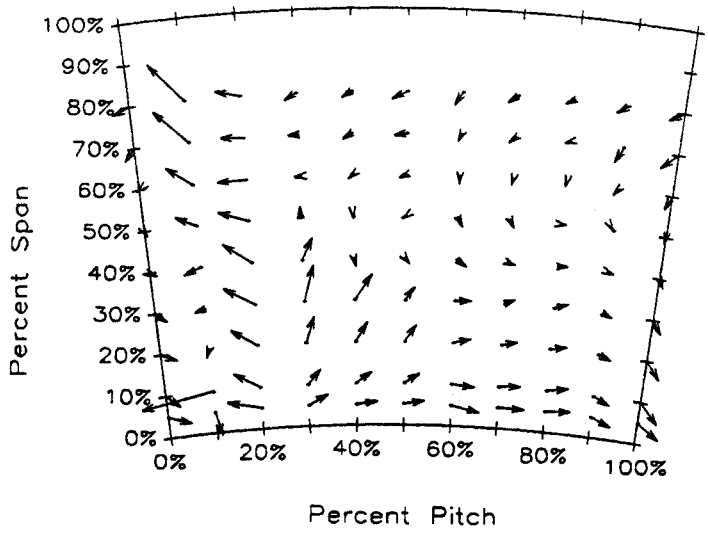

Figure 5.7: Exit lateral secondary velocity field.

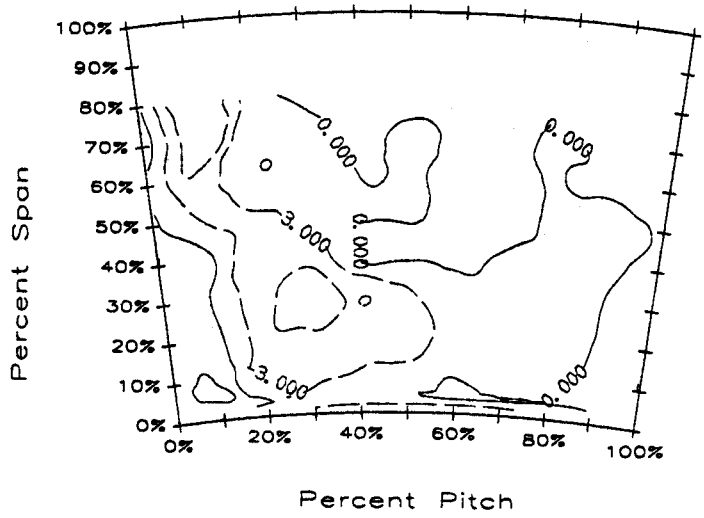

Figure 5.8: Exit pitch angle distribution, degrees.

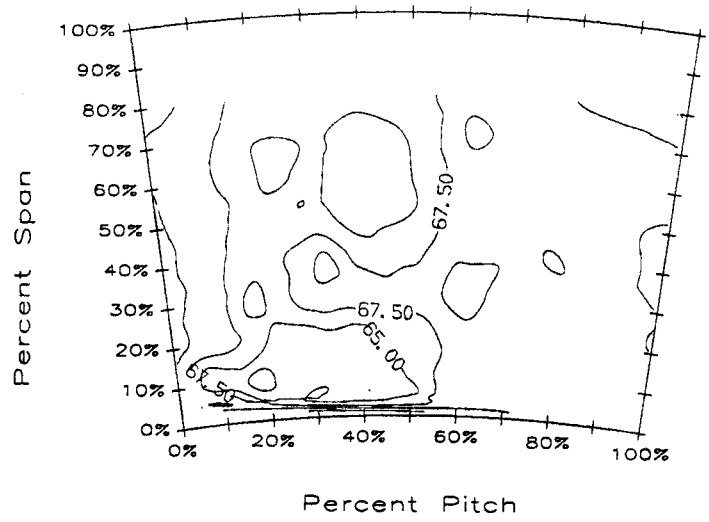

Figure 5.9: Exit yaw angle distribution, degrees.

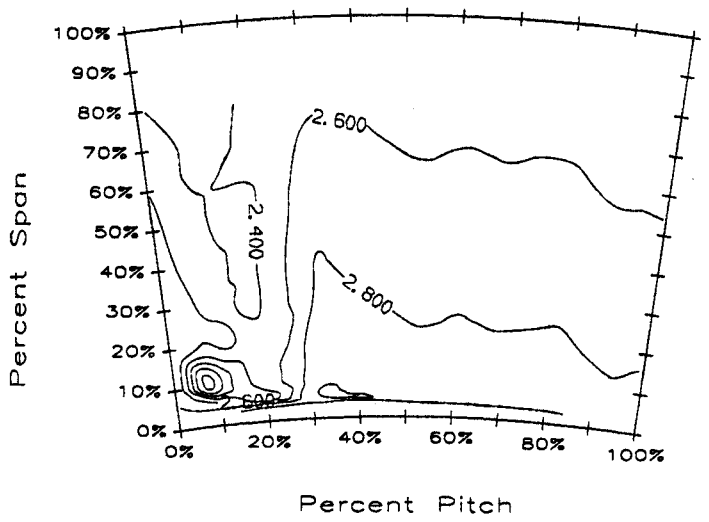

Figure 5.10: Exit velocity magnitude distribution: U/C_x.

three element hot-film probe, the velocity was measured in a plane 11.8% axial chord downstream of the trailing edge. The closely spaced vertical lines at the edges of the wake region indicate a large velocity gradient in the azimuthal direction. The wide spread circumferential lines throughout much of the rest of the passage indicate a low velocity gradient in the radial direction outside of the wake and suction surface exit regions.

Evidence of a high loss region is found in the total pressure contour plot of Fig. (5.11) in which the total pressure loss has been normalized by the dynamic pressure based on average inlet velocity. A high loss region coinciding with the low velocity region described above is clearly distinguishable throughout the wake region of the exit flow as well as in the hub/suction surface corner exit flow. Again there is considerable resemblance to data of Sharma et al. (1985) in spite of the differences in the entrance flow. The total pressure losses determined from this study extend through approximately 70% span in the wake region while the findings of Sharma et al. (1985) indicate the existence of measurable losses throughout the wake.

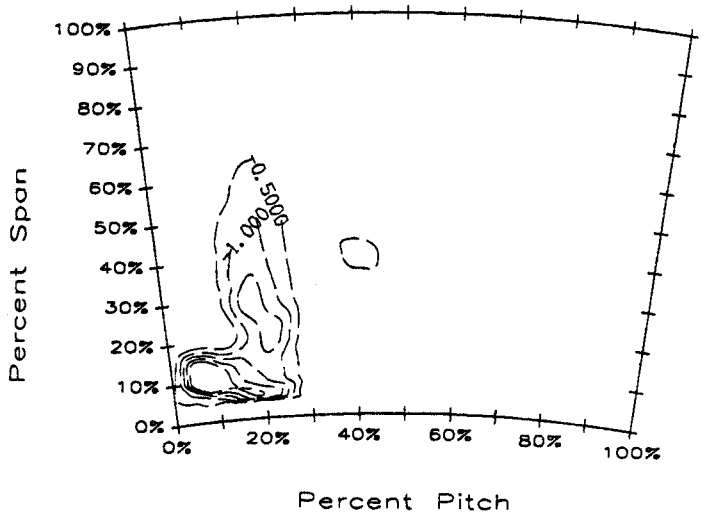

Figure 5.11: Exit total pressure loss distribution: $\frac{P_{t_0}-P_2}{\frac{1}{2}\rho C_x^2}$.

The static pressure contour plot (Fig. (5.12)) is very similar to that shown by Sieverding et al.

(1984) at a plane 11% axial chord downstream of the trailing edge of a similar cascade. A large static pressure gradient into the wake region from the surrounding flow exists at this axial location. There is evidence in the measurements of Sieverding et al. (1984) that this high azimuthal gradient in static pressure will be rapidly nearly eliminated downstream of this location leaving predominately a radial pressure gradient similar to that which appears outside of the wake region in Fig. (5.12).

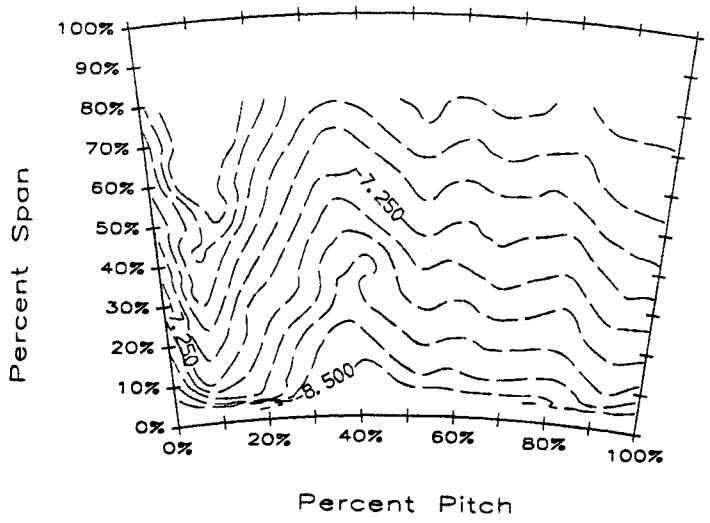

Figure 5.12: Exit static pressure distribution: $\frac{P_t - P_s}{\frac{1}{2}\rho C_x^2}$.

5.3 Airfoil Surface Static Pressure Distributions

One airfoil was instrumented with static pressure ports at twenty-two locations at each of seven equispaced spanwise locations. The pressure ports consisted of 0.0135 inch holes drilled normal to the airfoil surface into 1/16 inch holes drilled 1/16 inch below the surface. The latter pairs of holes were connected to an anemometer bank inclined 30 degrees. Pressure taps located at 0.125, 0.25 and 0.375 percent span were connected to the hub access holes while those located at 0.5, 0.625, 0.75 and 0.875 percent span were connected to the shroud access holes. A thin transparent tape was used to

seal off the pressure ports at all spanwise locations except the two (one with access via the hub, and the other with access via the shroud) spanwise locations being investigated (v. Gregory-Smith and Graves, 1983).

The resulting pressure coefficient distributions for each spanwise location are shown in Figs. (5.13) through (5.20). The gross features of each pressure coefficient distribution are alike. The midspan distribution is shown in Figs. (5.16) and (5.17) together with the results of Dring et al. (1986) for an axial spacing between the rotor and stator of 50% axial chord and flow coefficients of 68% and 96% respectively. There was good agreement between the results of this study and those of Dring et al. (1986) although the suction surface coefficients of pressure found here were higher than those determined in the LSRR. This could possibly be due to the downstream conditions since no rotor was used at the stator exit in this study. The significant effect of the rotor on the stator pressure distribution, especially the suction surface, has been shown by Dring et al. (1982) where the unsteady pressure envelope of the stator in the presence of the rotor was presented.

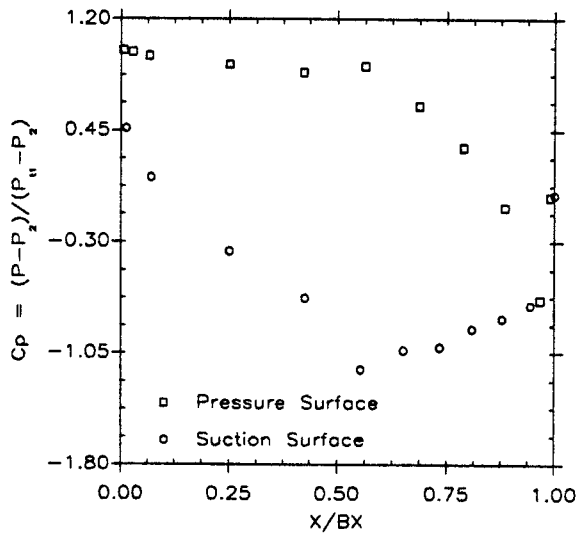

Figure 5.13: Airfoil static pressure distribution at 12.5% span.

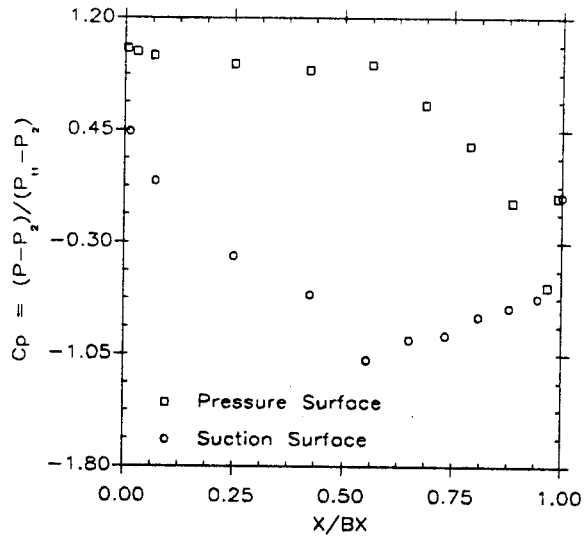

Figure 5.14: Airfoil static pressure distribution at 25% span.

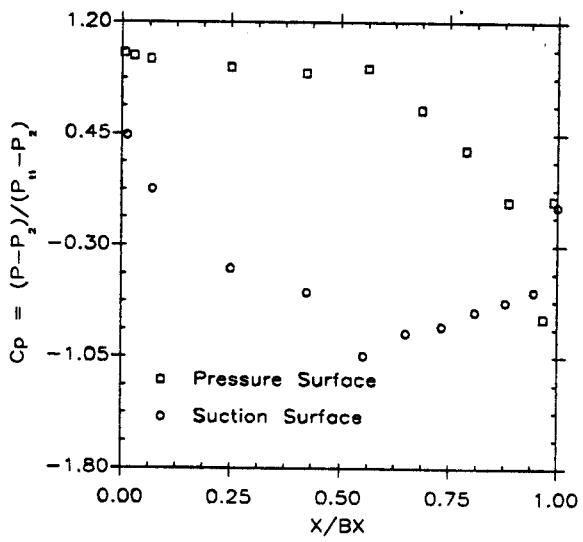

Figure 5.15: Airfoil static pressure distribution at 37.5% span.

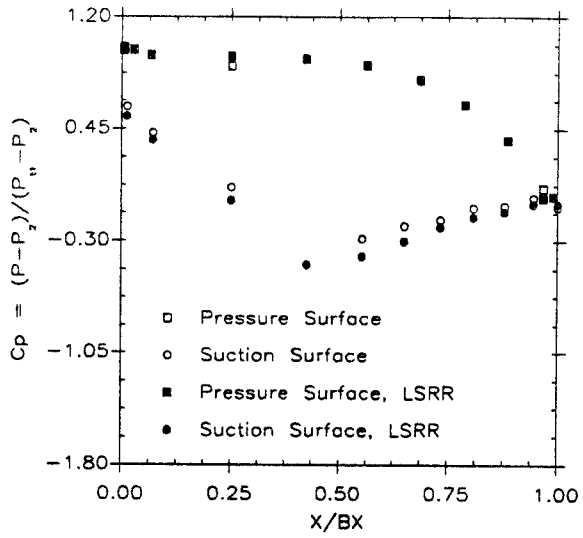

Figure 5.16: Airfoil static pressure distribution at 50% span. Included are the results of Dring et al. (1987) for $\psi = 0.68$.

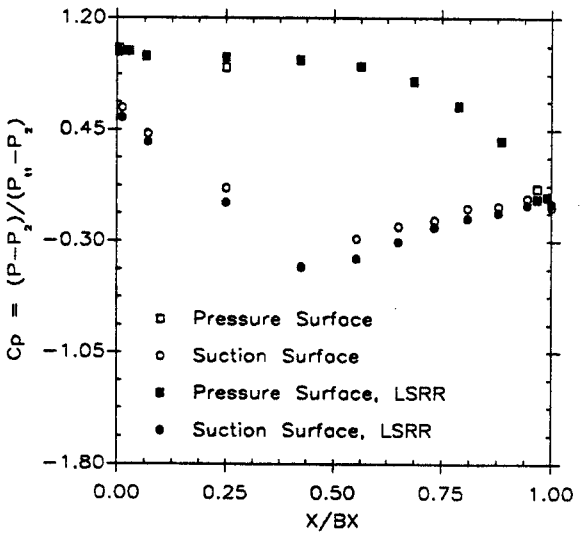

Figure 5.17: Airfoil static pressure distribution at 50% span. Included are the results of Dring et al. (1987) for $\psi = 0.96$.

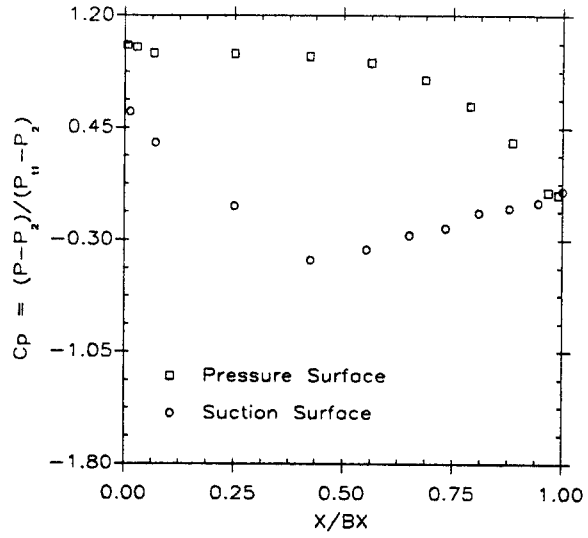

Figure 5.18: Airfoil static pressure distribution at 62.5% span.

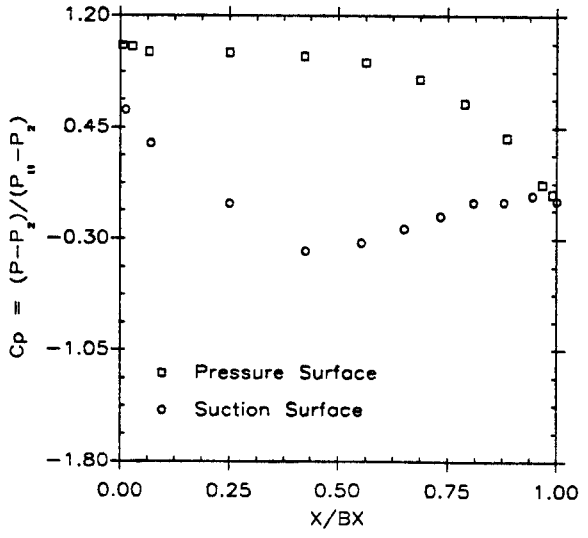

Figure 5.19: Airfoil static pressure distribution at 75% span.

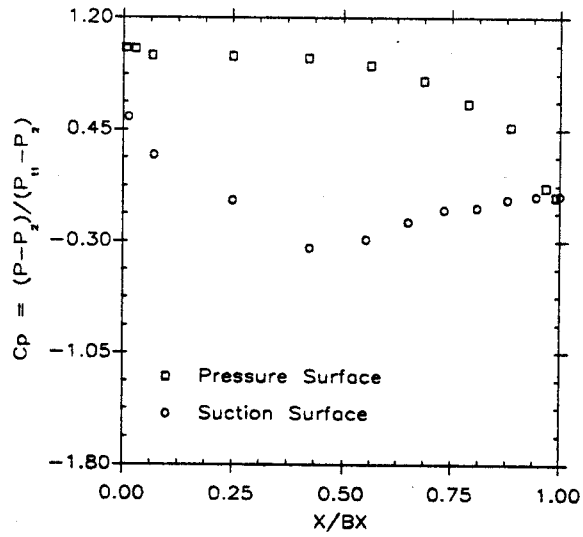

Figure 5.20: Airfoil static pressure distribution at 87.5% span.

Chapter 6

Results and Discussion

Two triple-wire probes were used to measure the midspan cross-correlation tensor across one stator pitch in a plane 10% axial chord downstream of the stator trailing edge. The number of equally spaced azimuthal locations was limited to 11 by probe and traverse geometries. The resulting number of location sets for the two probes was 55. For each of the 55 pairs of probe locations, 500 blocks of 8 channels (two triple-wire probes, pressure and temperature) of voltage data were recorded. The 880 MBytes of raw voltage data were stored on 8 mm videotapes before decoding and writing over the voltage files with the velocity components.

6.1 Reynolds Stresses

The Reynolds normal and shear stresses derived from the three component measurements are shown in Figs. (6.1) and (6.2). The wake takes up approximately 20% of the stator pitch at this axial location. This is consistent with the measurements of Sharma et al. (1985) in which the midspan wake was shown to span approximately 18% of the pitch at 11.8% axial chord downstream of the airfoil trailing edge. The magnitude of the axial and azimuthal normal Reynolds stresses derived from the triple-wire probe measurements were entirely consistent with the results of the preliminary cross-wire measurements. The success of the cross-wire in capturing the essential features of the axial and azimuthal velocity components is attributed to the relatively low turbulence levels across

the midspan and the alignment of the probe in the mean flow direction (v. Beuther et al. 1987).

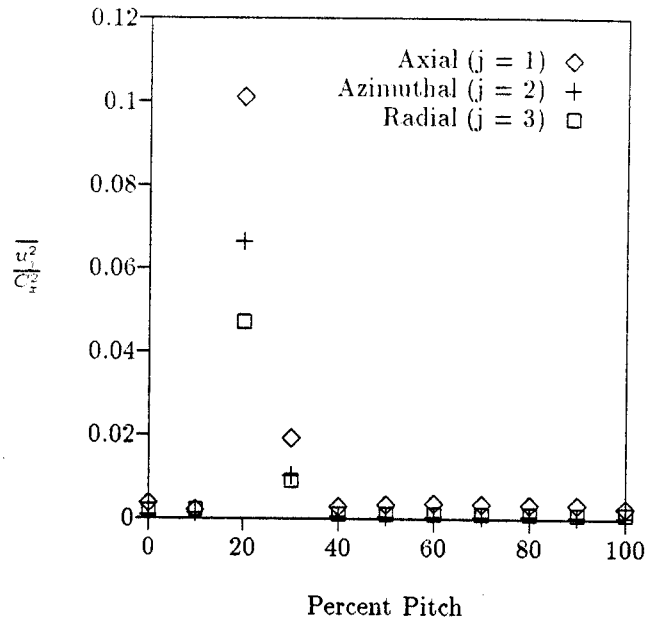

Figure 6.1: Reynolds normal stresses at 50% span.

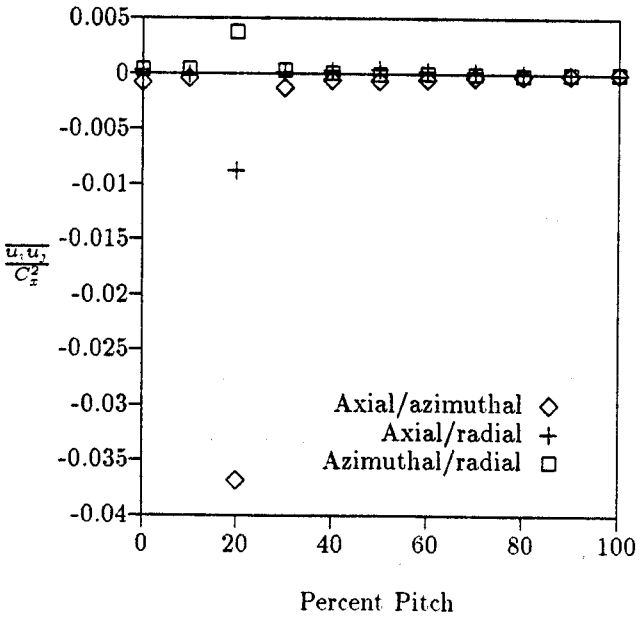

Figure 6.2: Reynolds shear stresses at 50% span.

6.2 Proper Orthogonal Decomposition

The Proper Orthogonal Decomposition was first applied to the entire set of 1089 cross-spectral estimates for the entire stator pitch midspan measurement set. Since there is a large difference in scales between the wake and outer flow regions, the POD was also applied to those two subdomains.

When the POD is applied in inhomogeneous directions after harmonic decomposition in the homogeneous directions, the spectral tensor can be expressed as a bilinear combination of the eigenmodes (Herzog, 1986). The reconstruction of the cross-spectral tensor can be expressed as

$$S_{i,j,k}(\theta_l, \theta_m) = \sum_{n=1}^{\infty} \Lambda_k^{(n)} \Phi_{i,k}^{(n)}(\theta_l) \Phi_{j,k}^{(n)*}(\theta_m) \tag{6.1}$$

Equation (6.1) is analogous to the representation of the cross-correlation tensor shown in Eq. (2.9). The results of this reconstruction for $i = j$ yields the power spectral density (PSD) of the each velocity component. Thus, to evaluate the adequacy of the eigenmodes to represent the flowfield, the measured power spectral densities can be compared to reconstructions based on the eigenmodes and eigenvalues. In the following sections, the PSD data are compared to reconstructions using the first five (dominant) POD modes.

6.2.1 Full Domain: 0-100% Pitch

The eigenspectra of the five dominant modes extracted by the POD are shown in Fig. (6.3). The eigenspectra represent the energy content of each of the eigenmodes. Figure (6.3) resembles the eigenvalue plots of Chambers et al. (1988). In that work, the Karhunen-Loéve expansion was applied to the solution of a randomly forced, one dimensional Burgers' equation with boundary conditions conducive to the development of thin boundary layers at the edges of the computational domain. The spectrum of the interior region of their calculation domain has the same character including the leveling off at high frequencies ('sequencies' in their terminology). It is suggested here that the increased energy content of the high frequency eigenspectra is due to the substantial broadband energy of the wake. As is shown in Section (6.2.2), the high frequency flattening is eliminated when the viscous wake region is not included in the POD domain. The first mode was

found to contain approximately 25% of the total energy of the measured field and three modes were required to capture over 50% of the energy. Another noteworthy feature of Fig. (6.3) is that the first few modes accomodate the high frequency content so that the higher mode eigenspectra decay qualitatively like those of the quasi-homogeneous interior region in the calculations of Chambers et al. (1988).

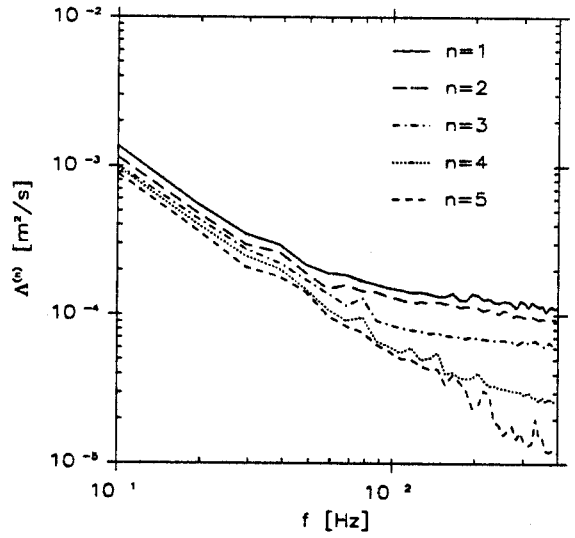

Figure 6.3: Full domain eigenspectra showing the energy distribution among the first five eigenmodes.

The power spectral densities (PSD) for the midspan measurement locations are included as Figs. (6.4) through (6.33). Since the energy content at high frequencies was deemed negligible and the interest in this study was the large-scale flow structures, the POD was applied for frequencies below 400 Hz. The smoothness of the PSD data is an indication of the adequacy of the number of ensembles used for the spectral estimates. The PSD exhibit the same trends at all locations except in the wake where the increased energy of the fluctuations in the axial and circumferential components may be due in part to spatial migration of the wake.

The convergence of the power spectral density expansions in terms of the five dominant eigenmode contributions are also shown in Figs. (6.4) through (6.33). The first five modes represented a large

portion of the energy of the velocity field at most of the measurement locations (as expected from the eigenspectra). The first modes typically contribute most of the energy to the lowest frequencies. The higher frequencies of the PSD are seen to progressively fill in as higher modes are included in the sum. This is consistent with the presumption that the eigenmodes are related to the large scale flow structures. In the vicinity of the wake, this trend is contradicted however (see especially Figs. (6.12) and (6.13)). This corresponds to the eigenspectral compensation for the high energy content at high frequencies discussed above.

The peak just above 200 Hz which appears in many of the PSD plots is at the blower blade crossing frequency. The eigenmode reconstructions consistently peak at that frequency even when no perceptible peak appears in the PSD data (e.g. Fig. (6.30)). The persistence of the POD modes in capturing the peak in the spectra at the blade passing frequency is encouraging in light of the requirement that the POD maximizes the mean squared projection of the modes on the velocity field.

Many of the POD modes have large distinct low frequency peaks (below 200 Hz) although not consistently at the same frequencies. These peaks are probably the result of either inlet flow disturbances or migration of passage generated flow structures. If the low frequency modes are manifestations of inlet disturbances then the disturbances would have to be on the order of 1 m based on an exit velocity of 55 m/s. The rapid acceleration caused by the inlet contraction and high passage turning could result in the lengthening of a shorter inlet disturbance to higher length scales. More detailed measurements are needed however, to determine the nature of the source of these low frequency (apparently large spatial scale) structures.

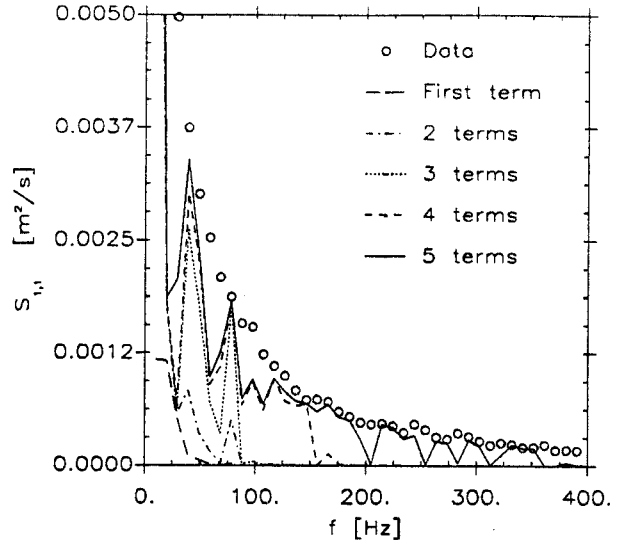

Figure 6.4: Full domain reconstruction of axial velocity component PSD at 0% pitch.

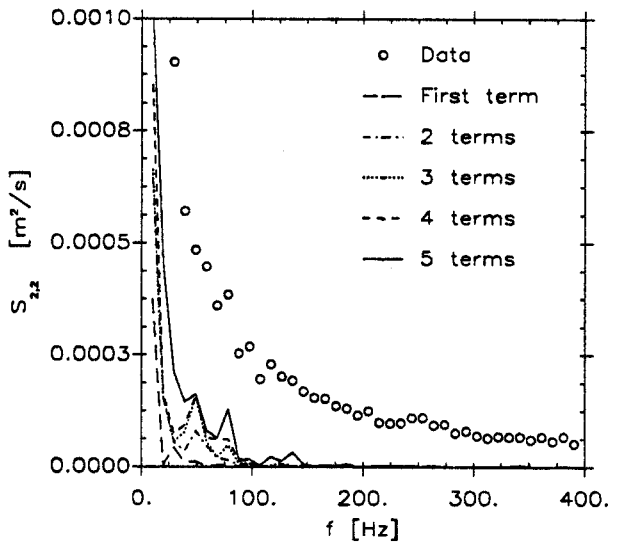

Figure 6.5: Full domain reconstruction of azimuthal velocity component PSD at 0% pitch.

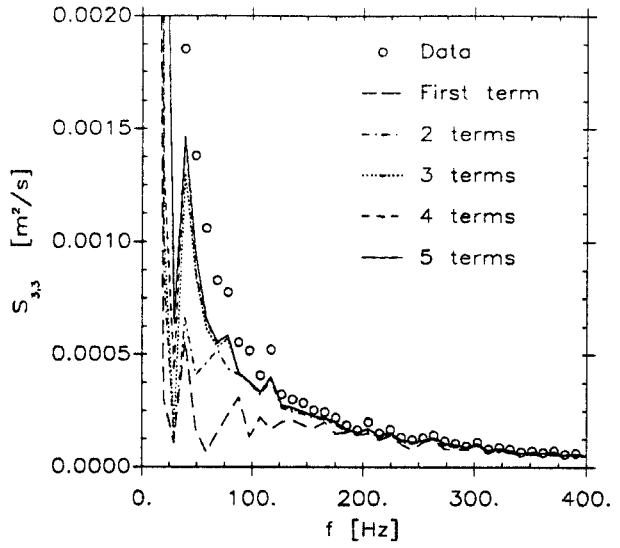

Figure 6.6: Full domain reconstruction of radial velocity component PSD at 0% pitch.

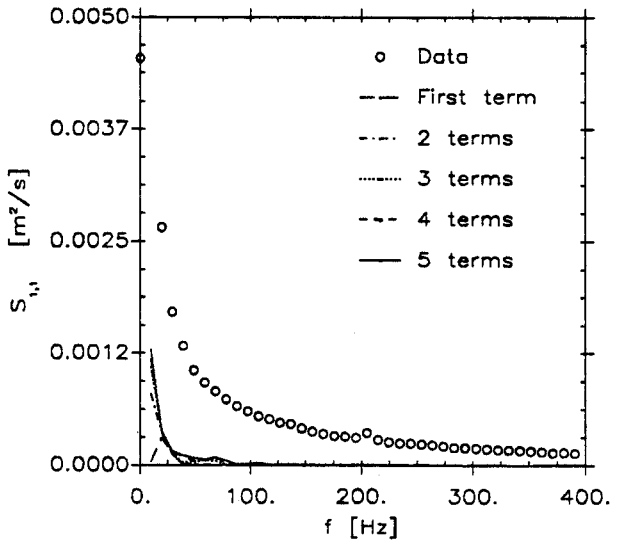

Figure 6.7: Full domain reconstruction of axial velocity component PSD at 10% pitch.

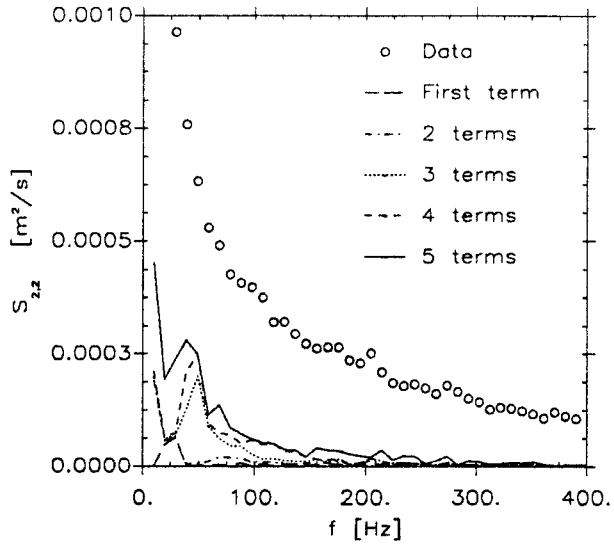

Figure 6.8: Full domain reconstruction of azimuthal velocity component PSD at 10% pitch.

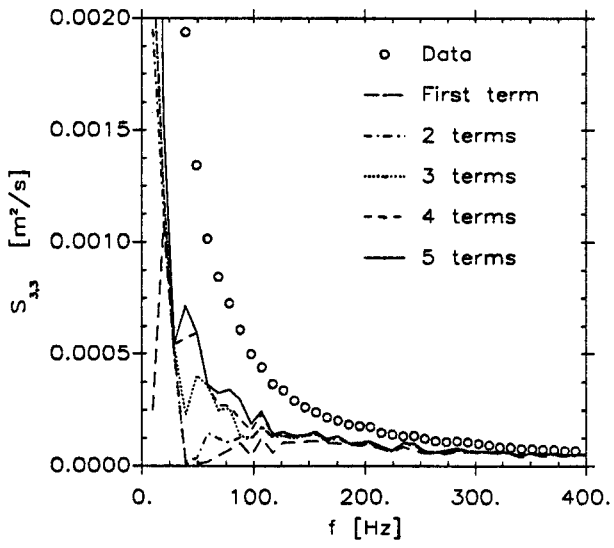

Figure 6.9: Full domain reconstruction of radial velocity component PSD at 10% pitch.

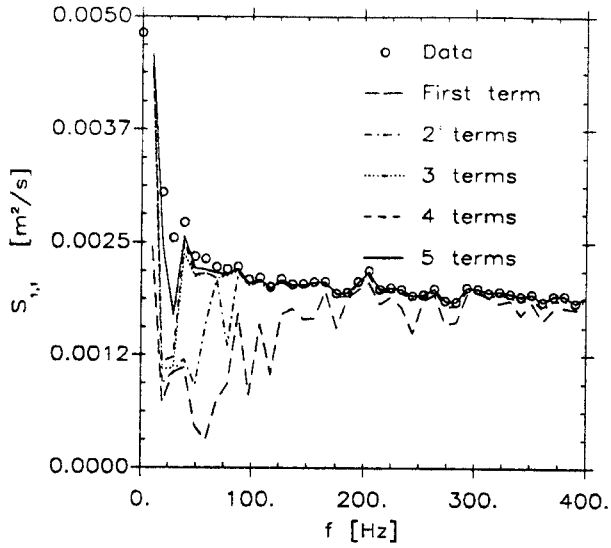

Figure 6.10: Full domain reconstruction of axial velocity component PSD at 20% pitch.

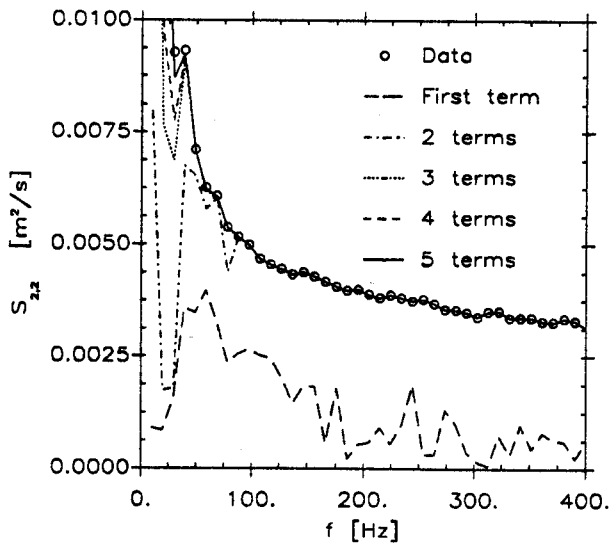

Figure 6.11: Full domain reconstruction of azimuthal velocity component PSD at 20% pitch.

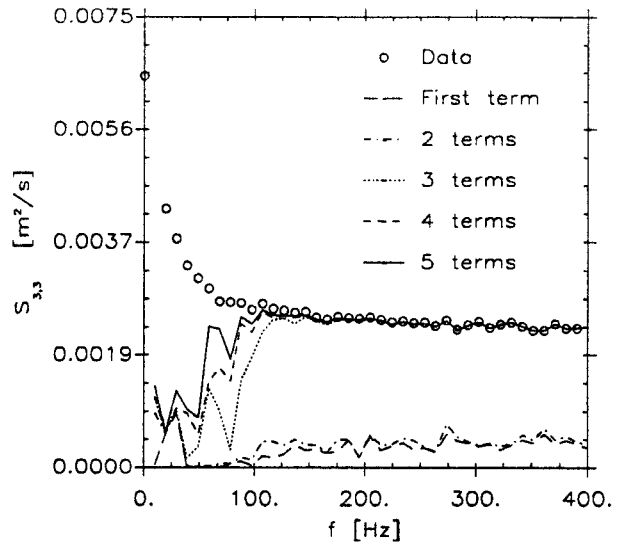

Figure 6.12: Full domain reconstruction of radial velocity component PSD at 20% pitch.

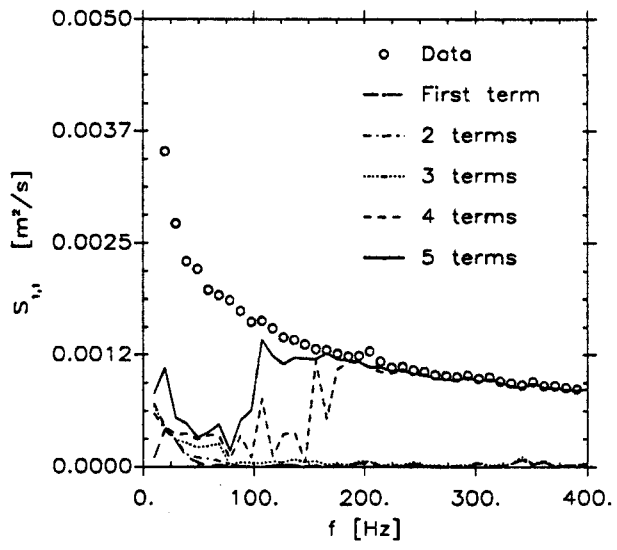

Figure 6.13: Full domain reconstruction of axial velocity component PSD at 30% pitch.

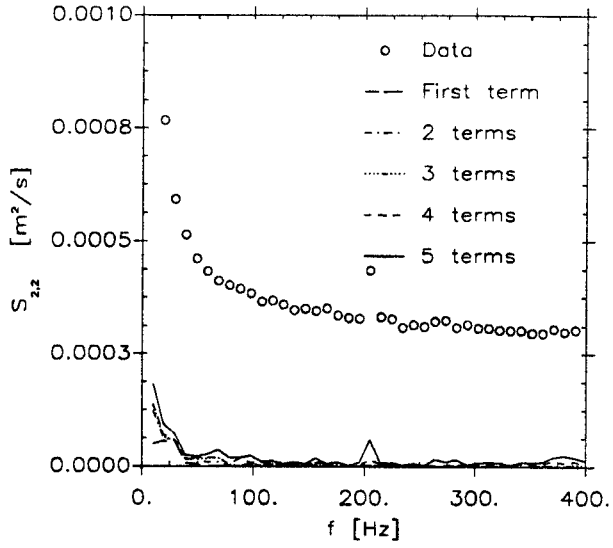

Figure 6.14: Full domain reconstruction of azimuthal velocity component PSD at 30% pitch.

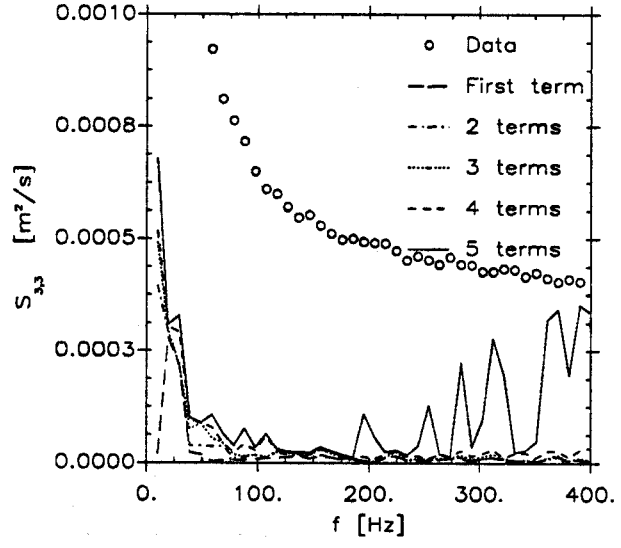

Figure 6.15: Full domain reconstruction of radial velocity component PSD at 30% pitch.

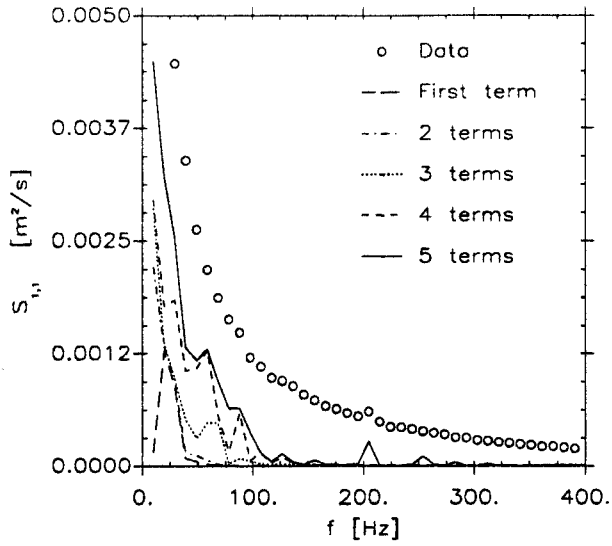

Figure 6.16: Full domain reconstruction of axial velocity component PSD at 40% pitch.

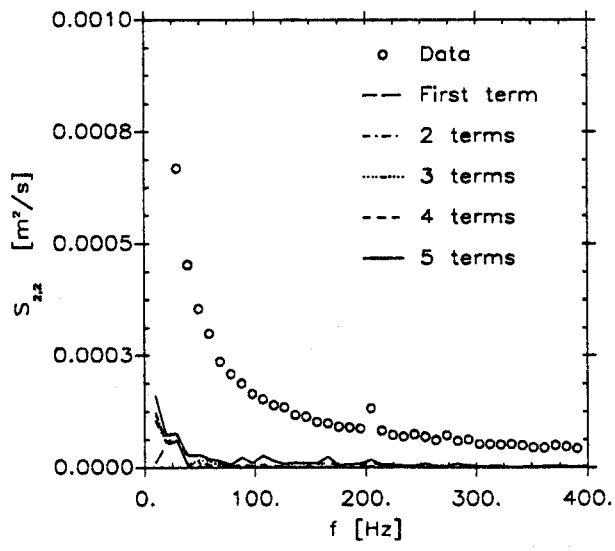

Figure 6.17: Full domain reconstruction of azimuthal velocity component PSD at 40% pitch.

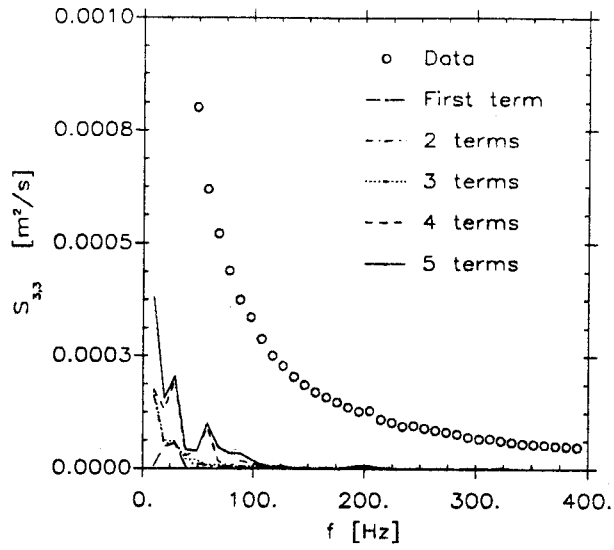

Figure 6.18: Full domain reconstruction of radial velocity component PSD at 40% pitch.

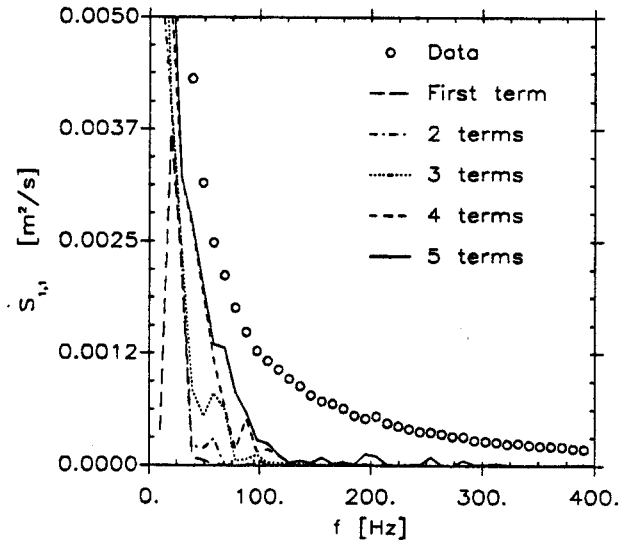

Figure 6.19: Full domain reconstruction of axial velocity component PSD at 50% pitch.

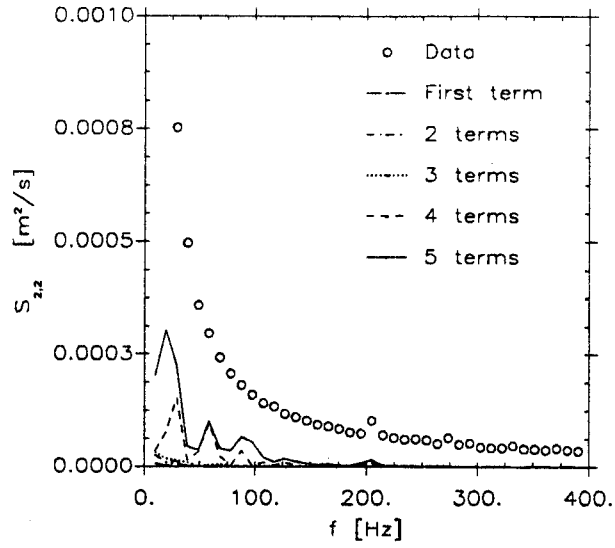

Figure 6.20: Full domain reconstruction of azimuthal velocity component PSD at 50% pitch.

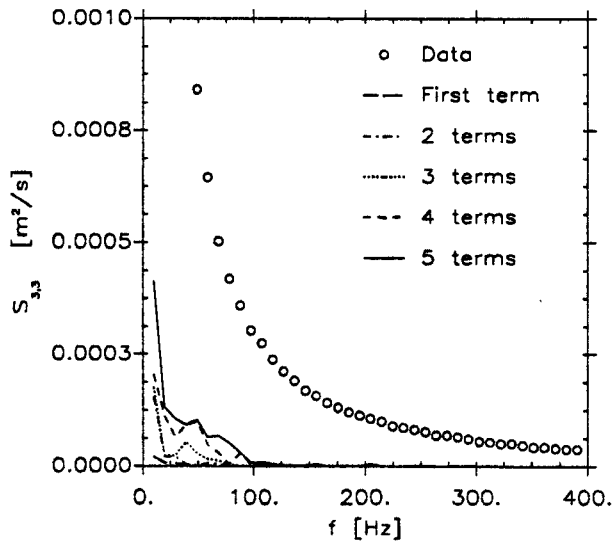

Figure 6.21: Full domain reconstruction of radial velocity component PSD at 50% pitch.

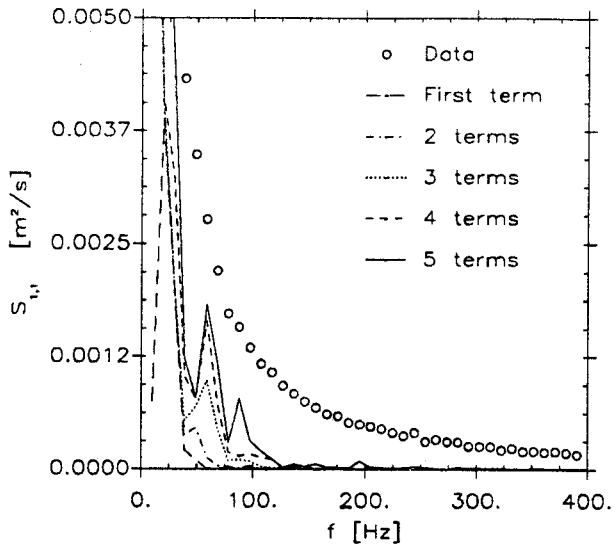

Figure 6.22: Full domain reconstruction of axial velocity component PSD at 60% pitch.

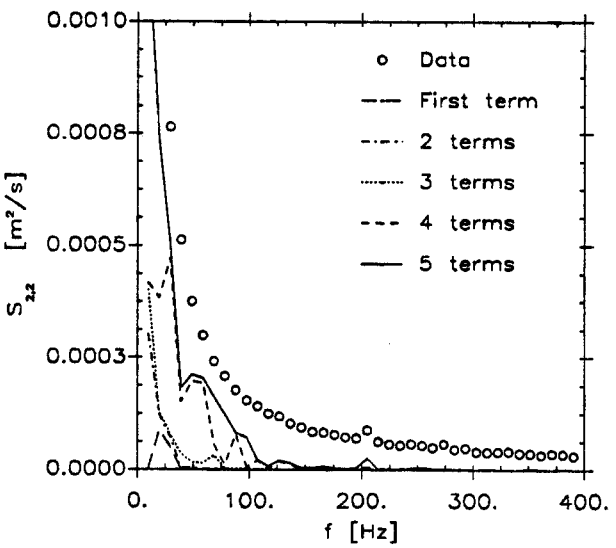

Figure 6.23: Full domain reconstruction of azimuthal velocity component PSD at 60% pitch.

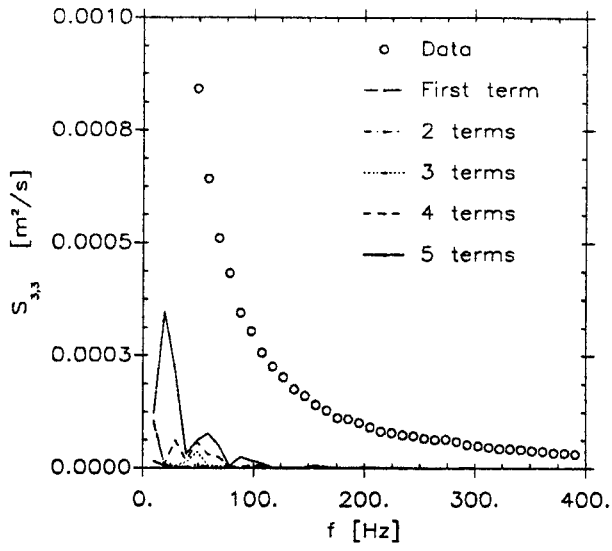

Figure 6.24: Full domain reconstruction of radial velocity component PSD at 60% pitch.

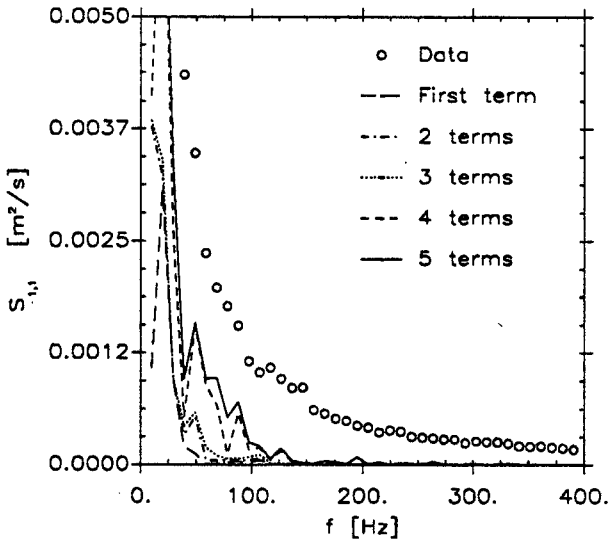

Figure 6.25: Full domain reconstruction of axial velocity component PSD at 70% pitch.

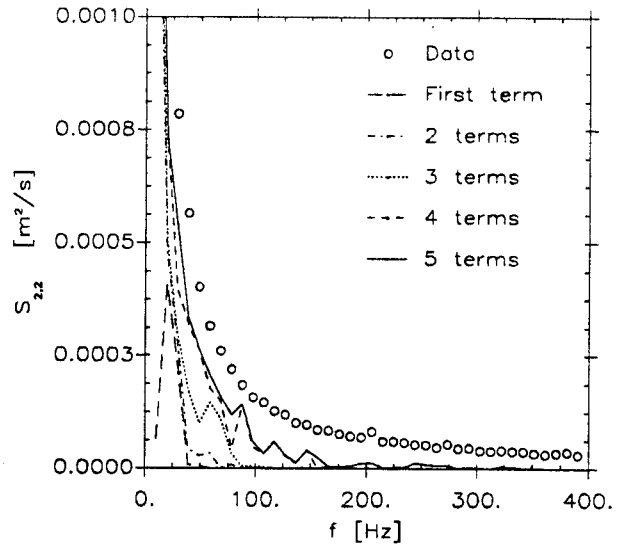

Figure 6.26: Full domain reconstruction of azimuthal velocity component PSD at 70% pitch.

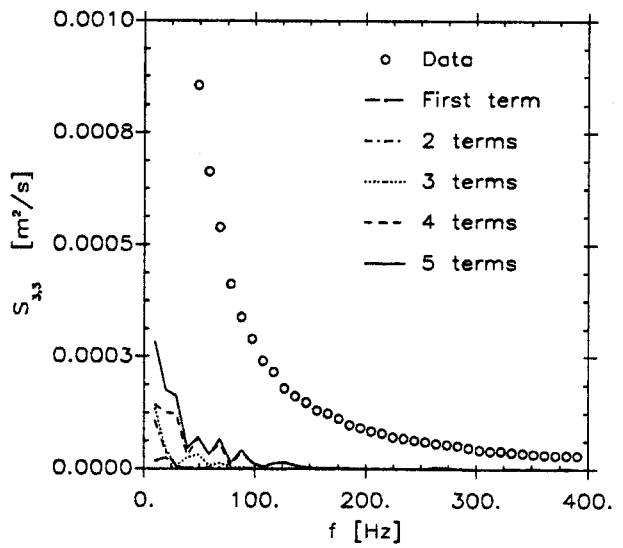

Figure 6.27: Full domain reconstruction of radial velocity component PSD at 70% pitch.

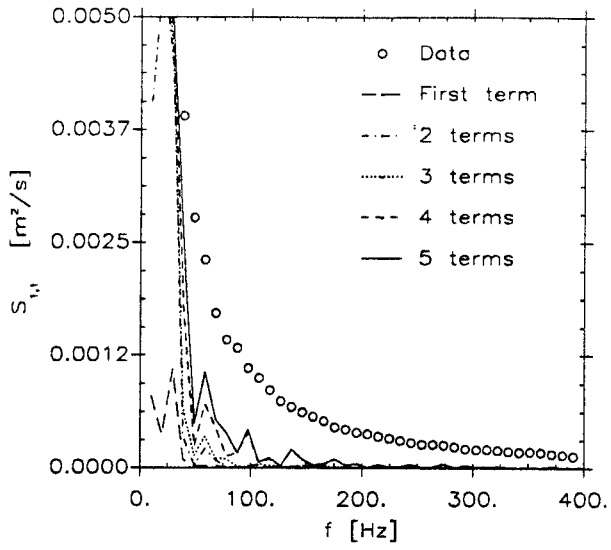

Figure 6.28: Full domain reconstruction of axial velocity component PSD at 80% pitch.

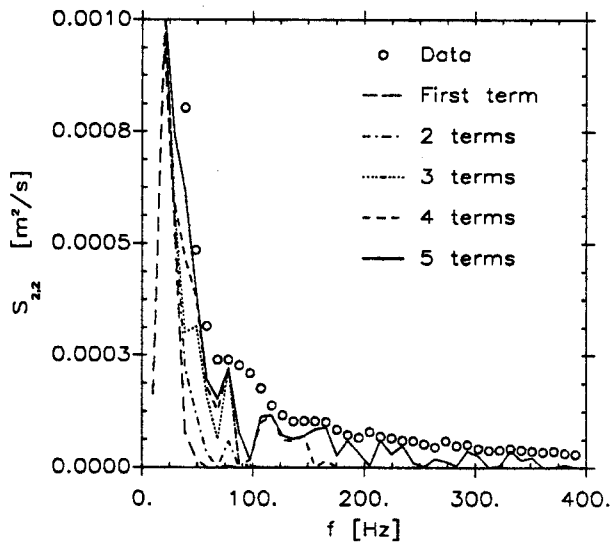

Figure 6.29: Full domain reconstruction of azimuthal velocity component PSD at 80% pitch.

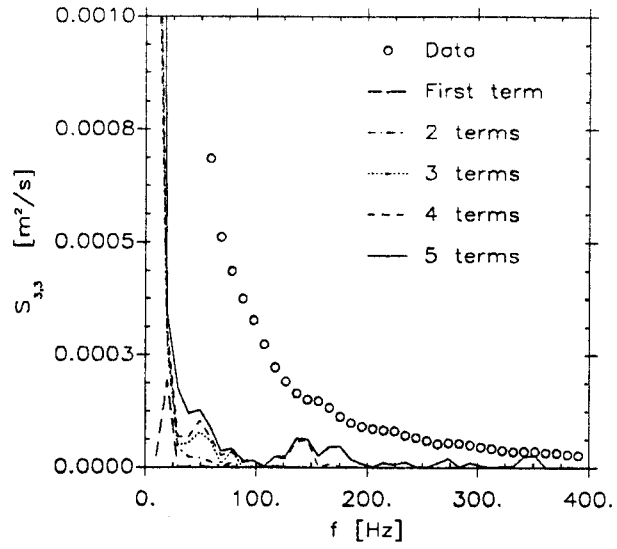

Figure 6.30: Full domain reconstruction of radial velocity component PSD at 80% pitch.

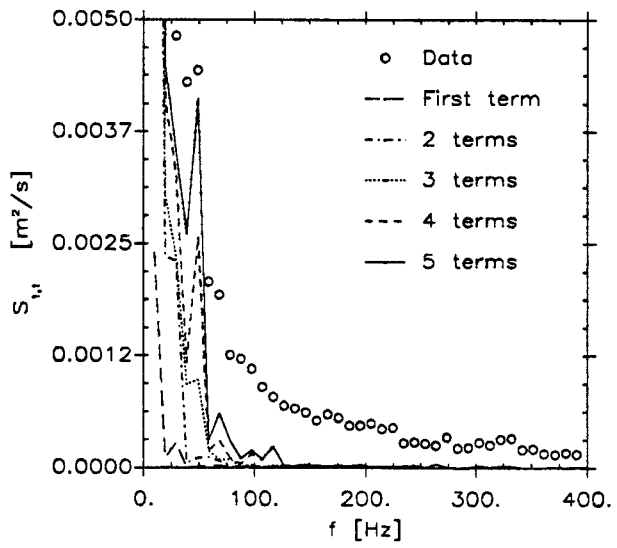

Figure 6.31: Full domain reconstruction of axial velocity component PSD at 90% pitch.

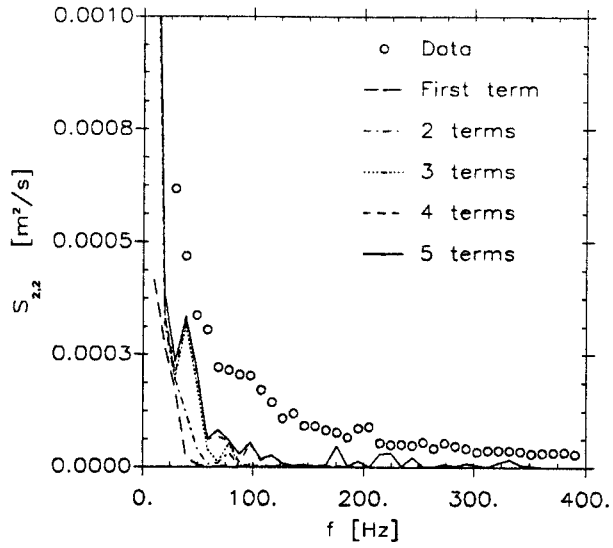

Figure 6.32: Full domain reconstruction of azimuthal velocity component PSD at 90% pitch.

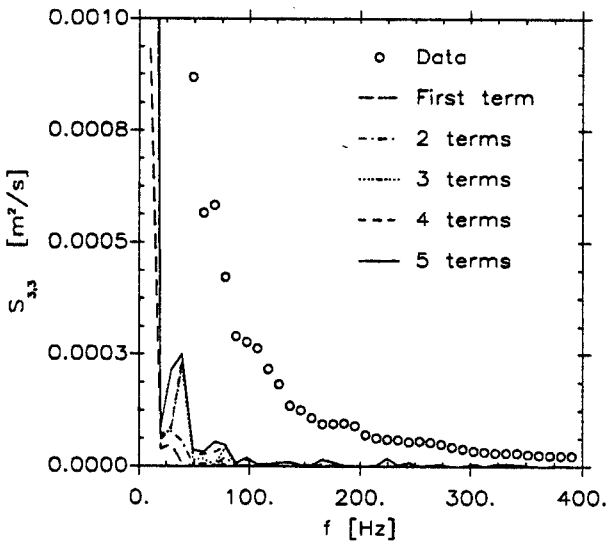

Figure 6.33: Full domain reconstruction of radial velocity component PSD at 90% pitch.

6.2.2 Subdomain Decomposition

Moin and Moser (1989) pointed out that division of the flowfield into subdomains may supplement the convergence of the expansions of the original field. George and Glauser (1991) have attributed this to the inner-outer character of boundary layer flows and suggest criteria for determining the number of modes required for each subdomain. In this study, outside of the hub and shroud boundary layers, the passage exit flow consists primarily of two domains, the wake and the outer flow regions. Because of the large difference in scales between these regions, the orthogonal decomposition was applied separately to the two domains in order to see if better convergence of the expansion could be achieved. The full domain (denoted by FD), five term PSD reconstructions have been plotted with the subdomain reconstructions in the following sections in order to gauge the advantage of such a division.

Wake Region: 0 - 40% Pitch

The wake spanned approximately 20% of the stator pitch at the measurement plane. The decomposition was therefore applied to cross-spectra from 0 to 40% pitch in order to fully capture the wake in the subdomain. The first five eigenspectra for the wake subdomain POD expansion are shown in Fig. (6.34). The broad spectrum of the wake disturbances produced the broadband flattening of the eigenspectra for high frequencies. The first mode contained approximately 33% of the energy of the subdomain. Only the first two terms were required to represent over 50% of the subdomain energy (compared to three terms for the full domain expansion). Again there exists a similarity between the eigenspectra for this subdomain and the eigenspectra calculated by Chambers et al. (1988). The concentrated effect of the wake was to broaden the eigenspectra to higher frequencies over a wide frequency range. The first few modes of this subdomain expansion accomodate the high energy content at the high frequencies as did those of the full domain expansion. This is illustrated in the PSD reconstructions at 20 and 30% pitch (Figs. (6.41) through (6.46) excluding Fig. (6.45)) where the PSD reconstruction fills in progressively from high frequency to low frequency.

The first five modes of the expansion of the wake domain were able to capture a significantly larger

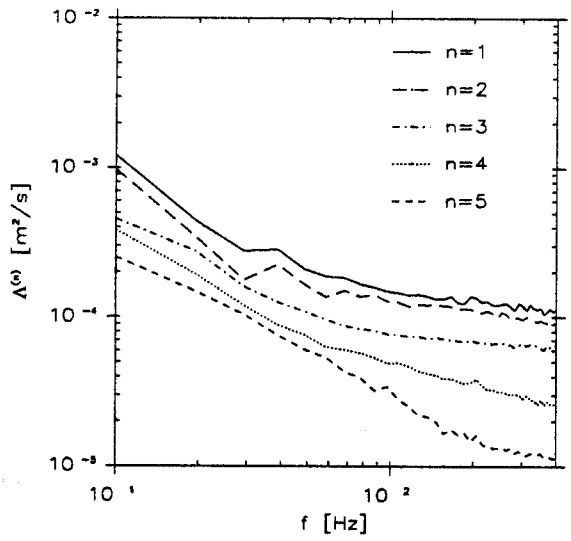

Figure 6.34: Wake subdomain eigenspectra showing the energy distribution among the first five eigenmodes.

amount of the energy at frequencies below 200 Hz. For higher frequencies, only the representation of the energy of the radial velocity component at 30% pitch was significantly improved.

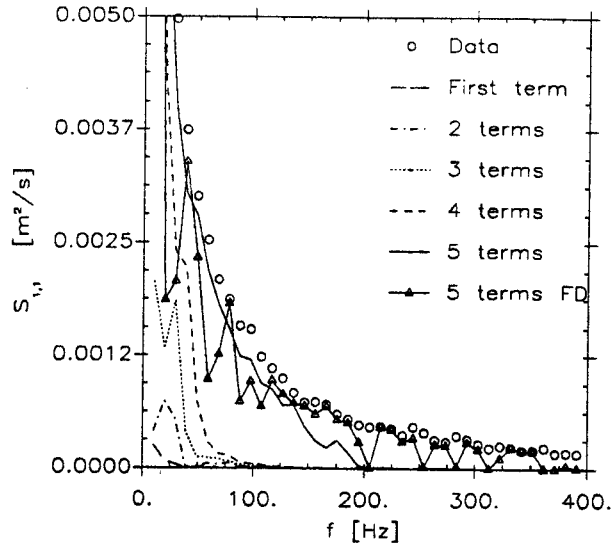

Figure 6.35: Wake subdomain reconstruction of axial velocity component PSD at 0% pitch.

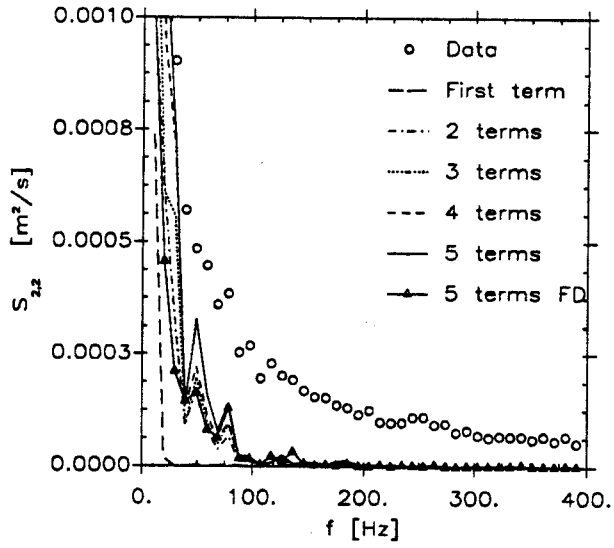

Figure 6.36: Wake subdomain reconstruction of azimuthal velocity component PSD at 0% pitch.

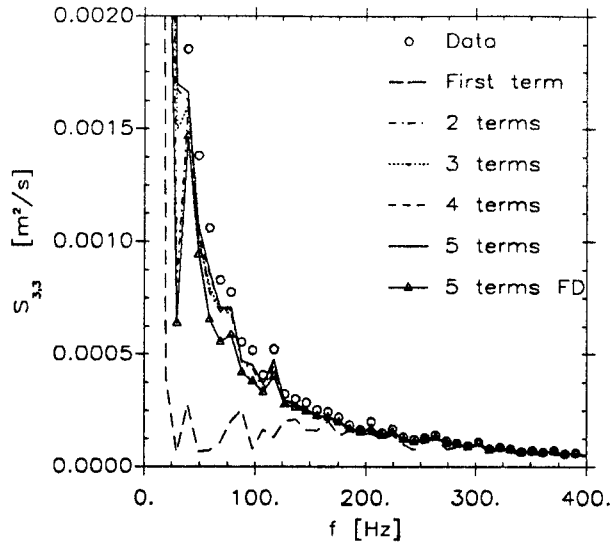

Figure 6.37: Wake subdomain reconstruction of radial velocity component PSD at 0% pitch.

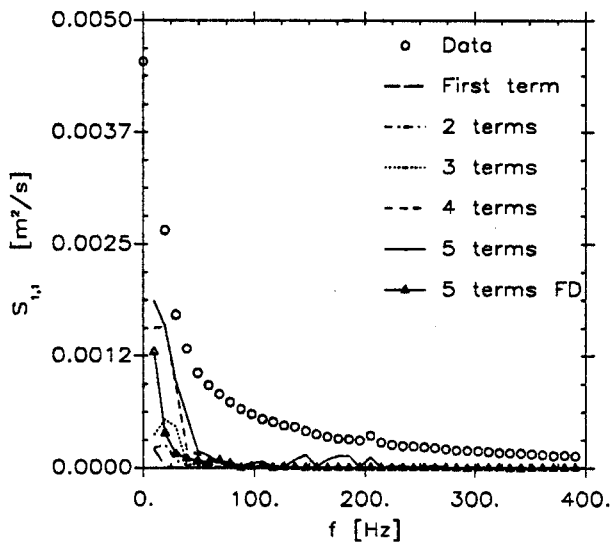

Figure 6.38: Wake subdomain reconstruction of axial velocity component PSD at 10% pitch.

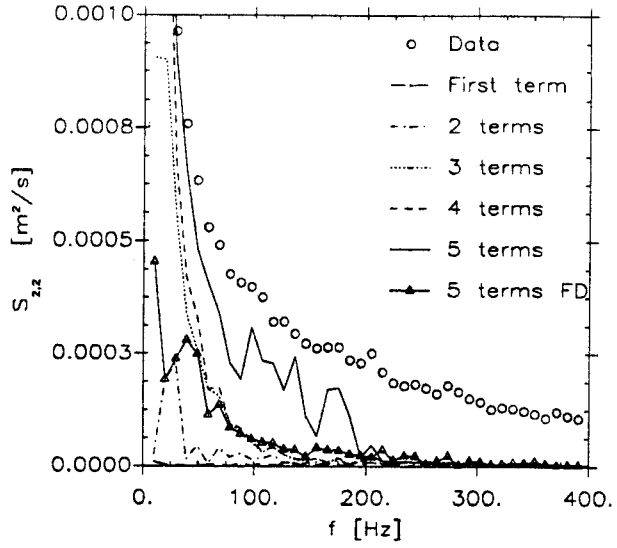

Figure 6.39: Wake subdomain reconstruction of azimuthal velocity component PSD at 10% pitch.

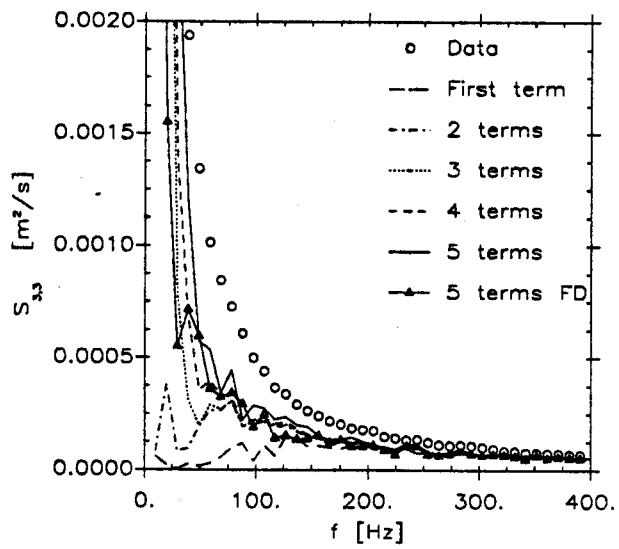

Figure 6.40: Wake subdomain reconstruction of radial velocity component PSD at 10% pitch.

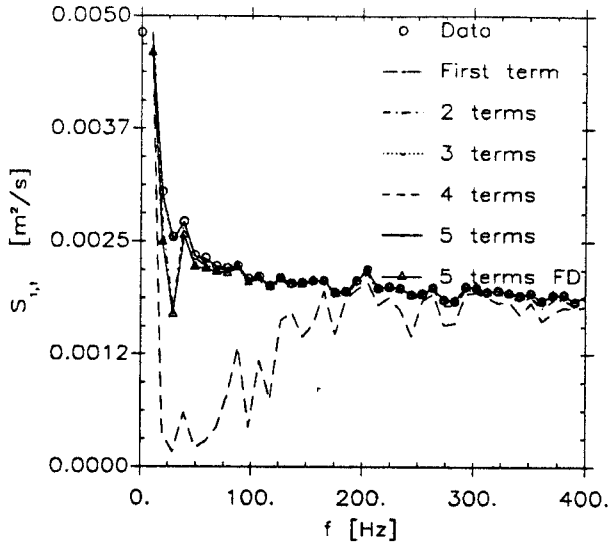

Figure 6.41: Wake subdomain reconstruction of axial velocity component PSD at 20% pitch.

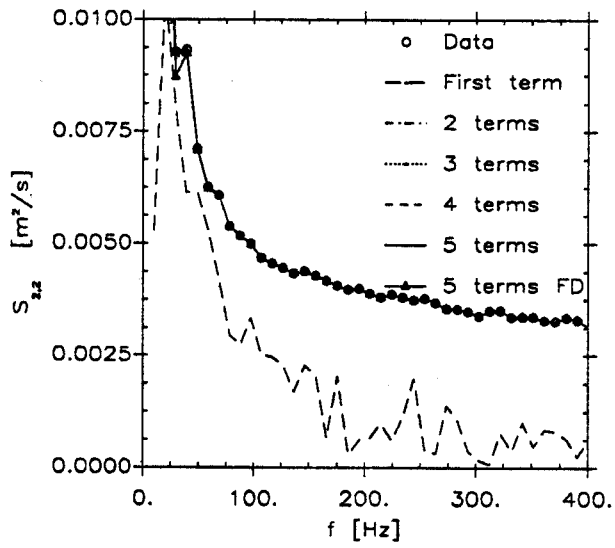

Figure 6.42: Wake subdomain reconstruction of azimuthal velocity component PSD at 20% pitch.

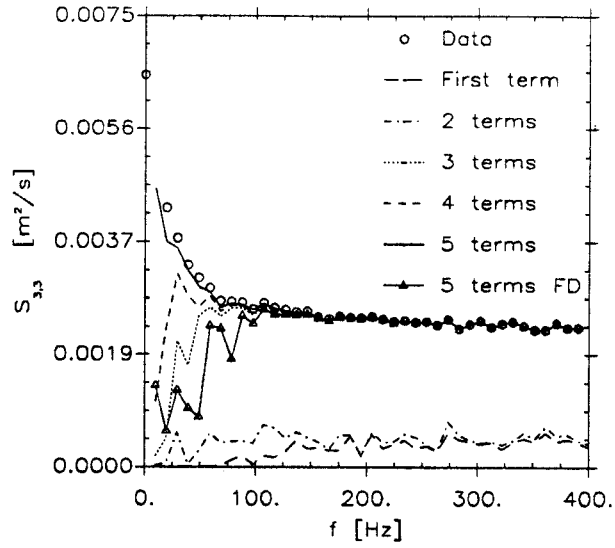

Figure 6.43: Wake subdomain reconstruction of radial velocity component PSD at 20% pitch.

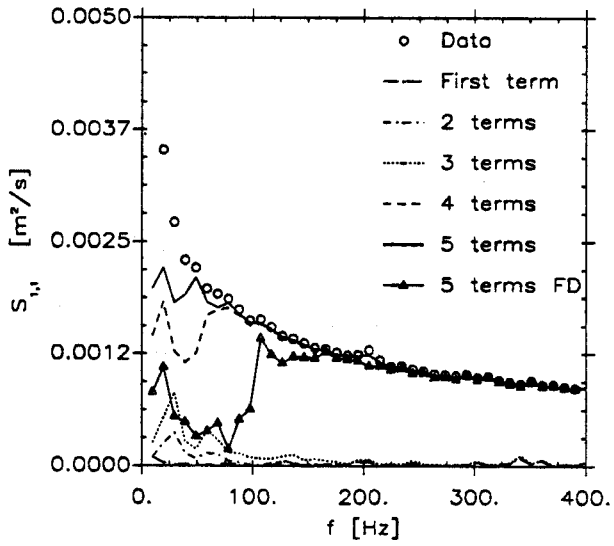

Figure 6.44: Wake subdomain reconstruction of axial velocity component PSD at 30% pitch.

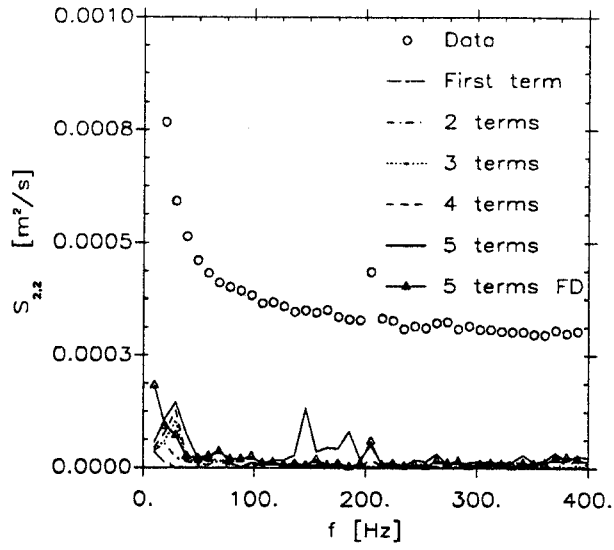

Figure 6.45: Wake subdomain reconstruction of azimuthal velocity component PSD at 30% pitch.

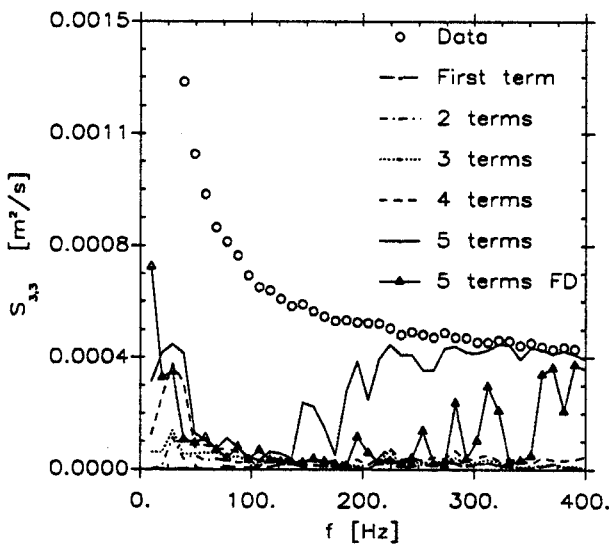

Figure 6.46: Wake subdomain reconstruction of radial velocity component PSD at 30% pitch.

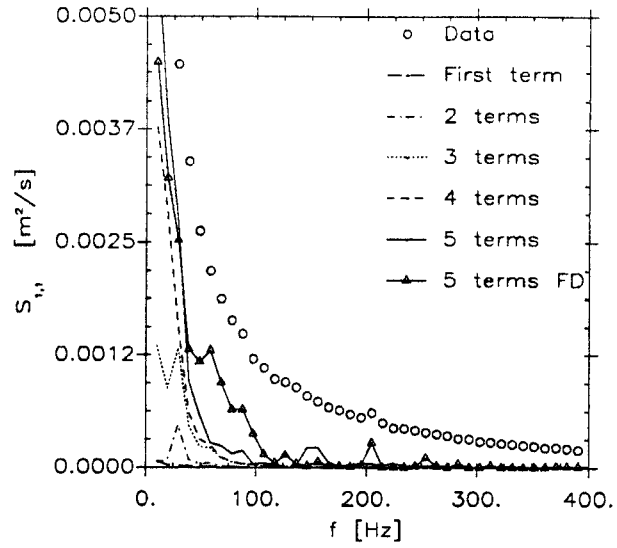

Figure 6.47: Wake subdomain reconstruction of axial velocity component PSD at 40% pitch.

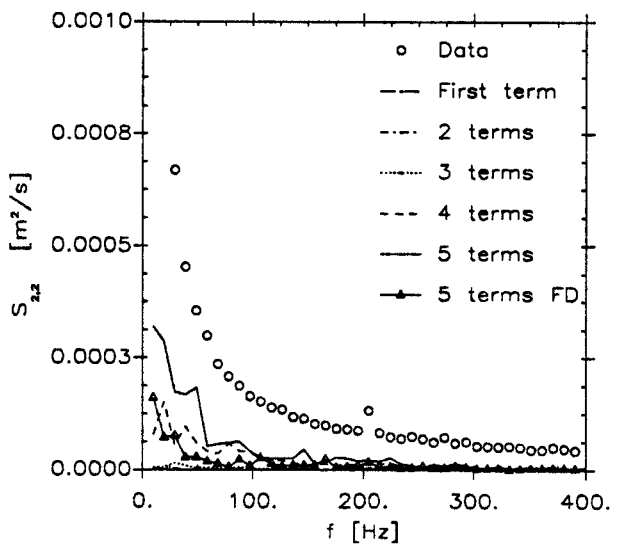

Figure 6.48: Wake subdomain reconstruction of azimuthal velocity component PSD at 40% pitch.

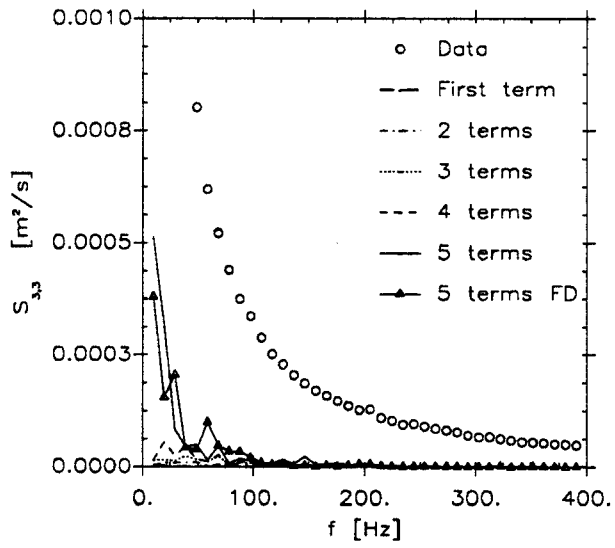

Figure 6.49: Wake subdomain reconstruction of radial velocity component PSD at 40% pitch.

Outer Flow Region: 40 - 90% Pitch

The outer flow was decomposed using measured cross-spectra from 40 to 90% pitch. The dominant eigenspectra of the outer flow subdomain expansion are shown in Fig.(6.50). The high energy content at high frequencies was eliminated (relative to the wake and full domain expansions) by limiting the domain to the outer flow. Consequently, the eigenspectra of the expansion of this region show no signs of the high frequency leveling off associated with the viscous flow regions. The first term of this subdomain expansion characterized only 17% of the total subdomain energy and four modes were required to represent over 50% of the subdomain energy. Thus the expansion of the outer flow converges less rapidly than the domains including the wake region. This is consistent with the calculation results of Chambers et al. (1988) in which the viscous boundary layers were small relative to the quasi-homogeneous interior region and the Karhunen-Loéve expansion was found to be slowly converging. It implies that the unsteady flow in this region is not dominated by large scale turbulence, but rather a complete range of scales.

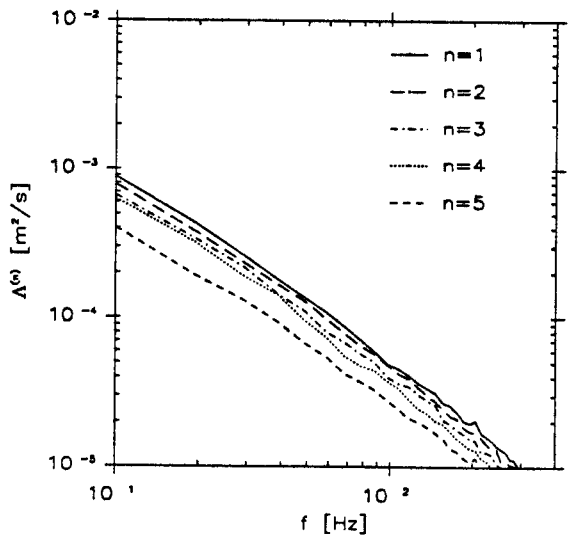

Figure 6.50: Outer flow subdomain eigenspectra showing the energy distribution among the first five eigenmodes.

Five term PSD reconstruction using the outer flow eigenmodes gave very good representations of the power spectral densities of the axial velocity component except at 90% pitch. Reconstruction of the other component spectra were only moderately improved over the reconstruction using five terms of the full domain decomposition.

Since the 40% pitch location was common to all three decomposition domains, a direct comparison was made of the 5 term reconstructions of the three component power spectral densities. Figures (6.69) through (6.71) compare the five term reconstructions of the velocity power spectral densities at 40% pitch using the eigenmodes and eigenvalues from the full domain (FD), wake domain (WD) and outer flow domain (OD) POD applications. The reconstruction of the axial and radial component spectra were best achieved using the outer flow subdomain eigenmodes. The wake domain eigenmodes produced a faster converging reconstruction of the azimuthal velocity spectra.

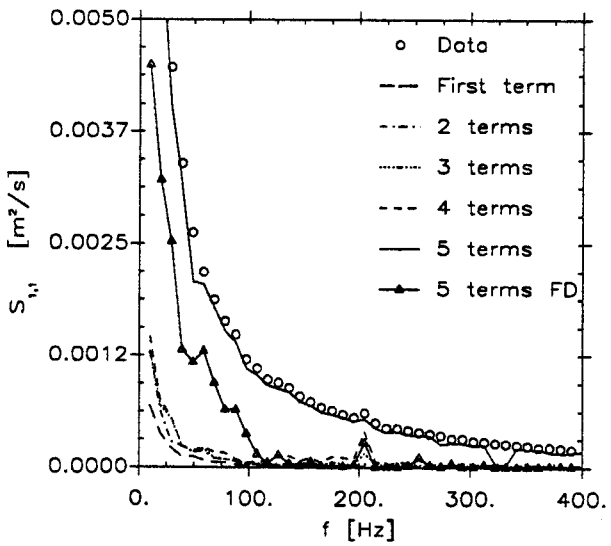

Figure 6.51: Outer flow subdomain reconstruction of axial velocity component PSD at 40% pitch.

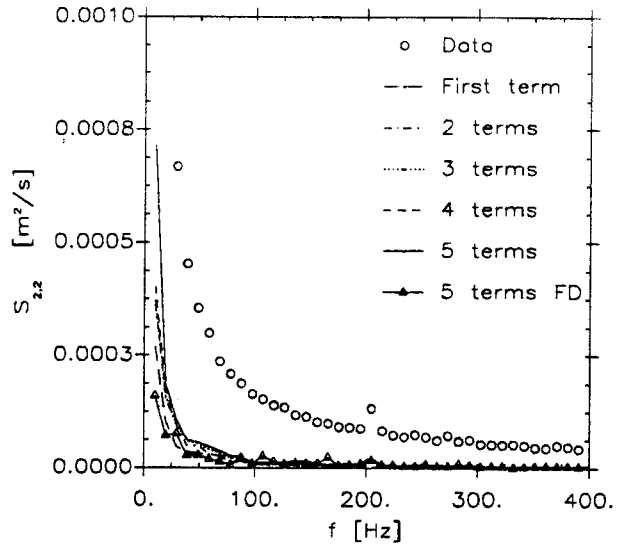

Figure 6.52: Outer flow subdomain reconstruction of azimuthal velocity component PSD at 40% pitch.

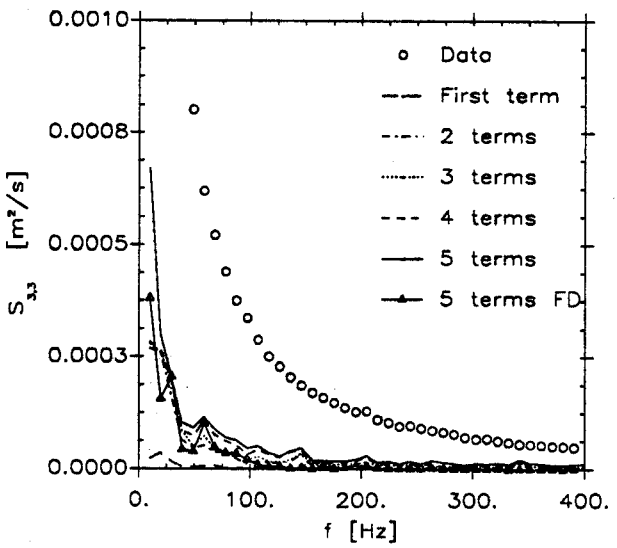

Figure 6.53: Outer flow subdomain reconstruction of radial velocity component PSD at 40% pitch.

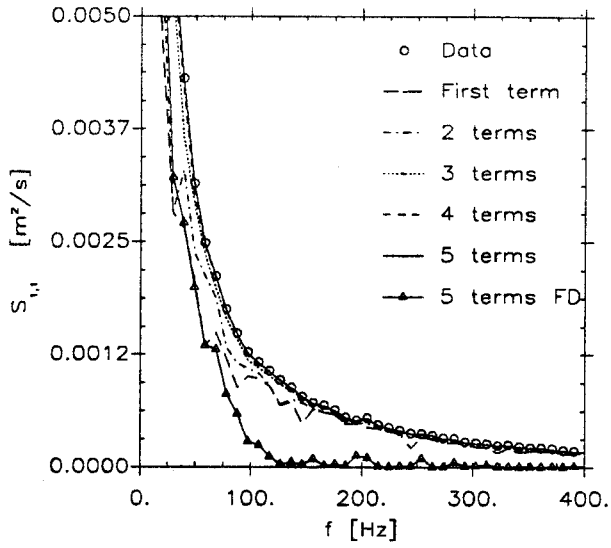

Figure 6.54: Outer flow subdomain reconstruction of axial velocity component PSD at 50% pitch.

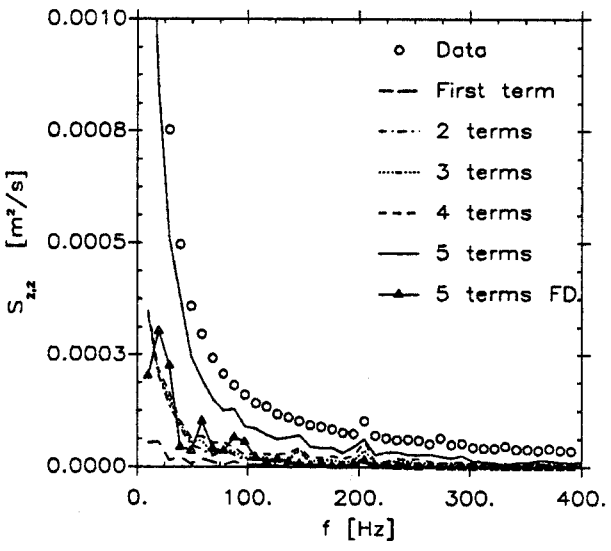

Figure 6.55: Outer flow subdomain reconstruction of azimuthal velocity component PSD at 50% pitch.

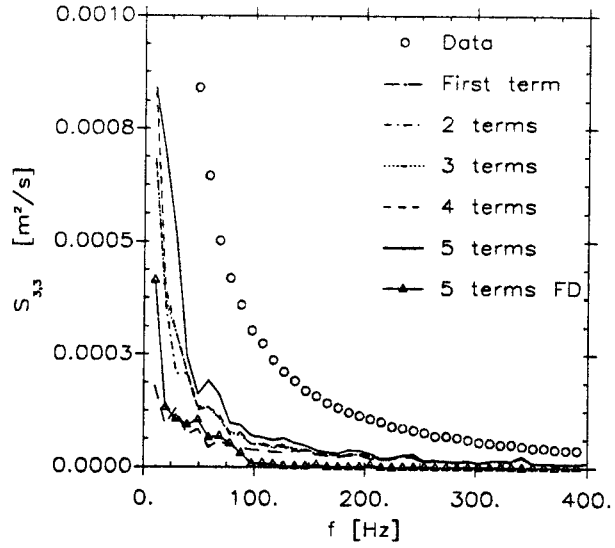

Figure 6.56: Outer flow subdomain reconstruction of radial velocity component PSD at 50% pitch.

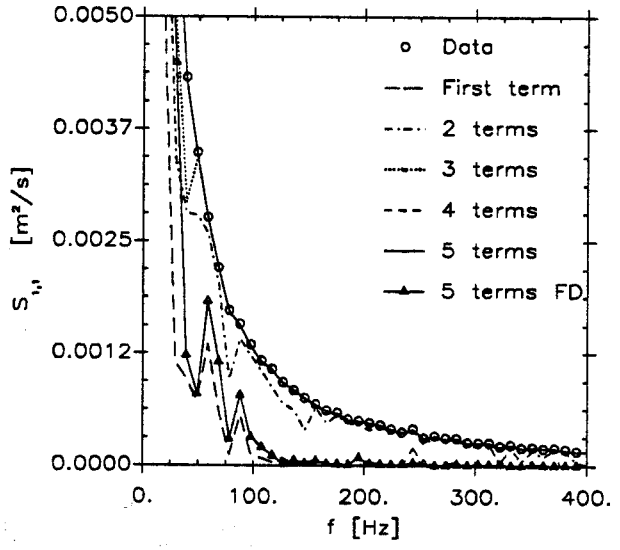

Figure 6.57: Outer flow subdomain reconstruction of axial velocity component PSD at 60% pitch.

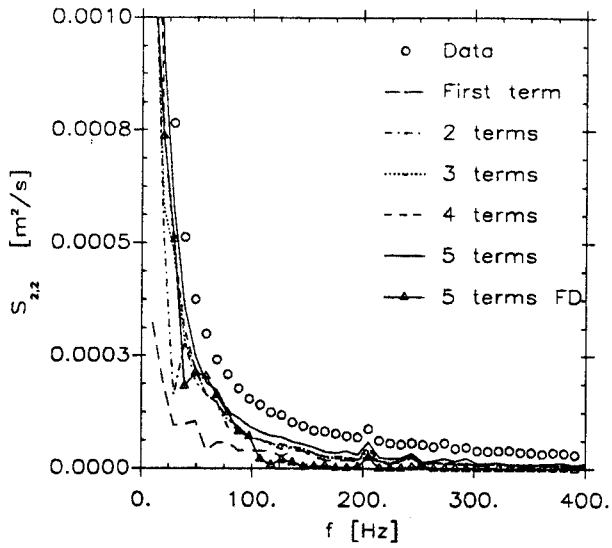

Figure 6.58: Outer flow subdomain reconstruction of azimuthal velocity component PSD at 60% pitch.

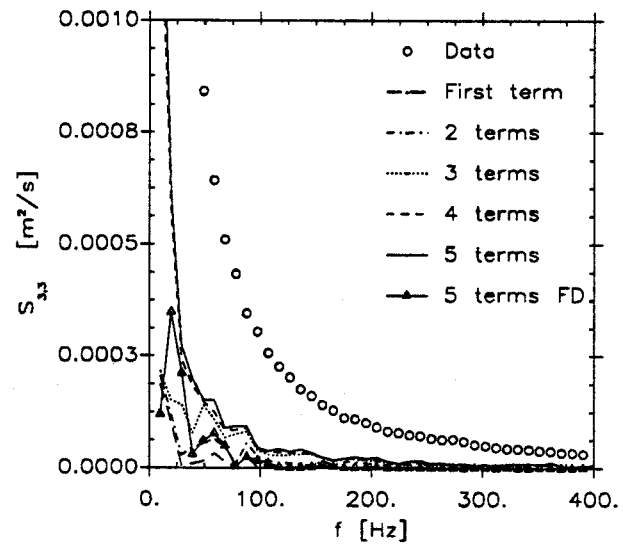

Figure 6.59: Outer flow subdomain reconstruction of radial velocity component PSD at 60% pitch.

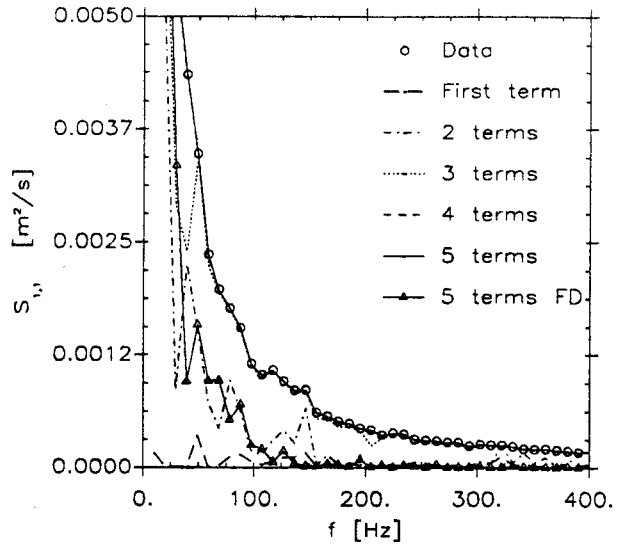

Figure 6.60: Outer flow subdomain reconstruction of axial velocity component PSD at 70% pitch.

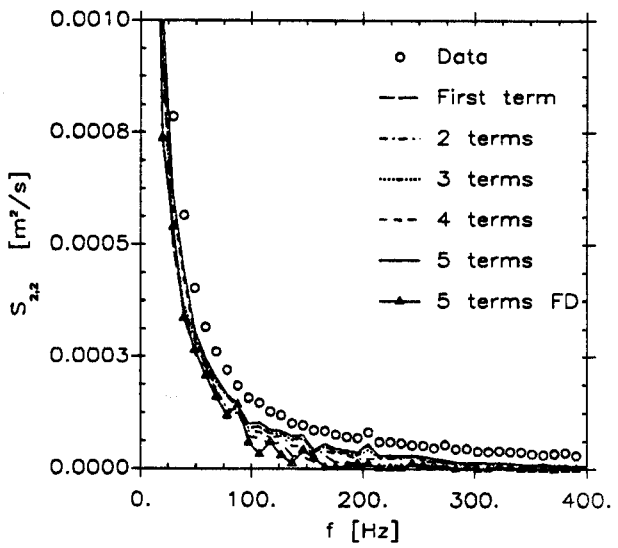

Figure 6.61: Outer flow subdomain reconstruction of azimuthal velocity component PSD at 70% pitch.

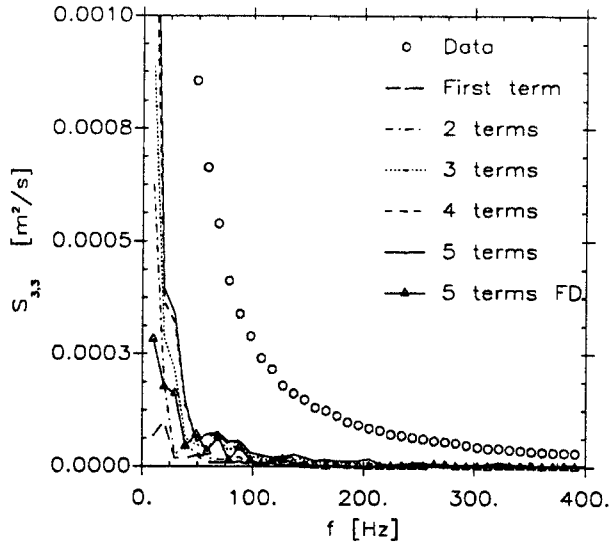

Figure 6.62: Outer flow subdomain reconstruction of radial velocity component PSD at 70% pitch.

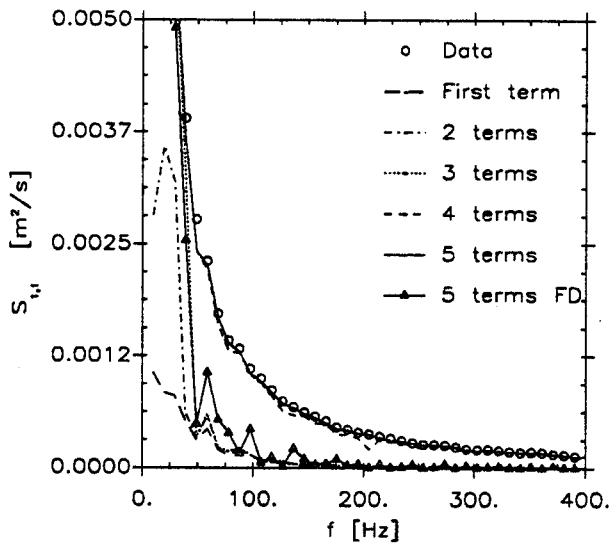

Figure 6.63: Outer flow subdomain reconstruction of axial velocity component PSD at 80% pitch.

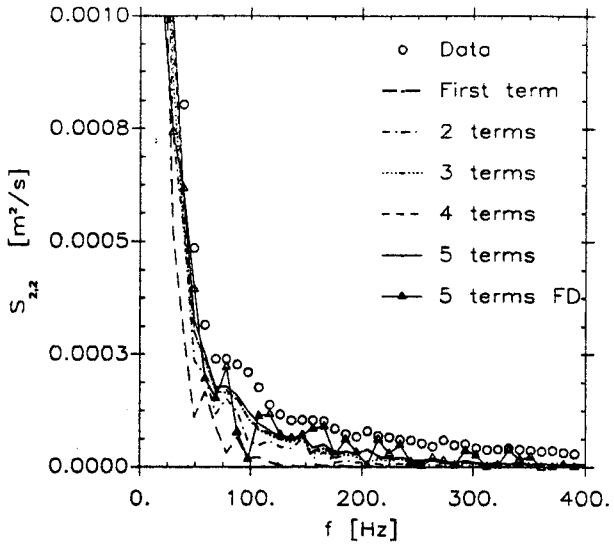

Figure 6.64: Outer flow subdomain reconstruction of azimuthal velocity component PSD at 80% pitch.

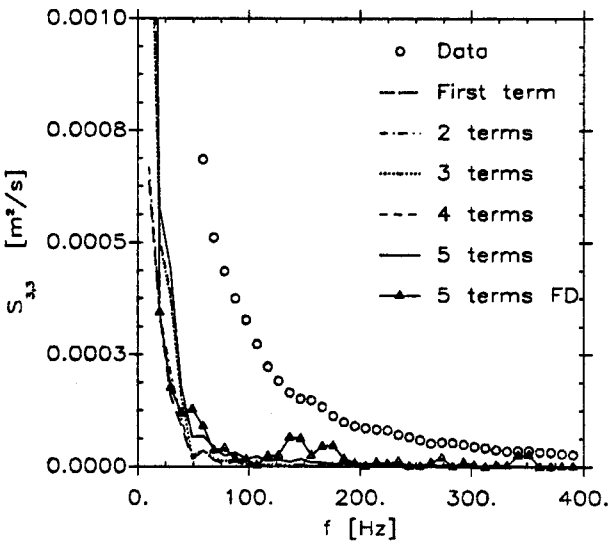

Figure 6.65: Outer flow subdomain reconstruction of radial velocity component PSD at 80% pitch.

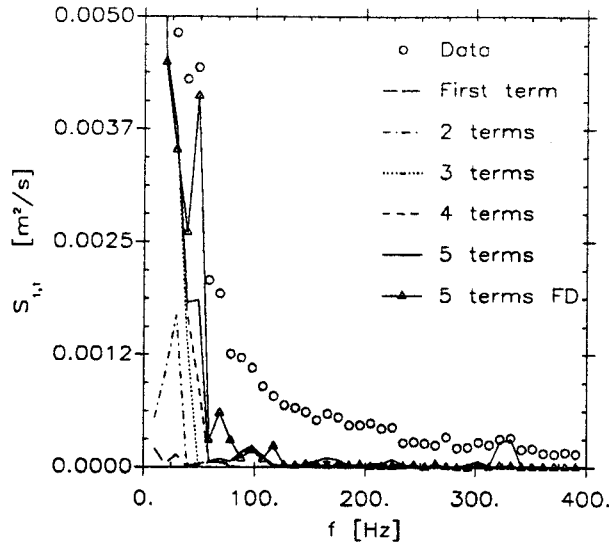

Figure 6.66: Outer flow subdomain reconstruction of axial velocity component PSD at 90% pitch.

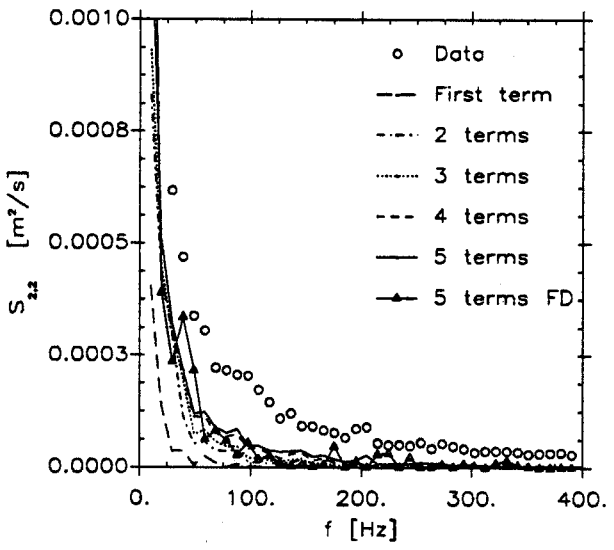

Figure 6.67: Outer flow subdomain reconstruction of azimuthal velocity component PSD at 90% pitch.

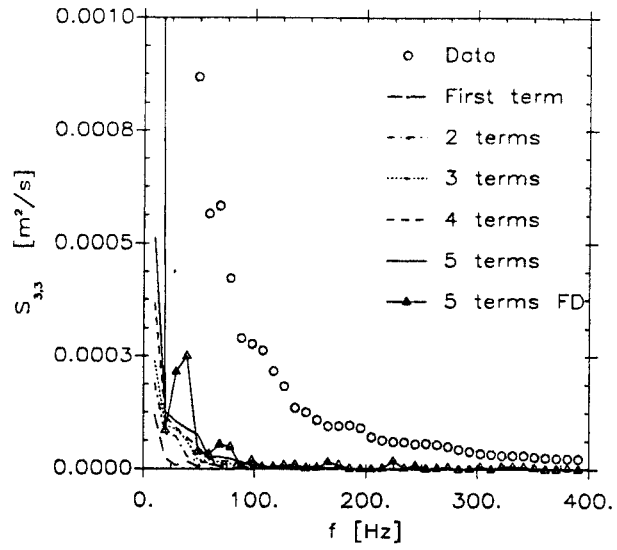

Figure 6.68: Outer flow subdomain reconstruction of radial velocity component PSD at 90% pitch.

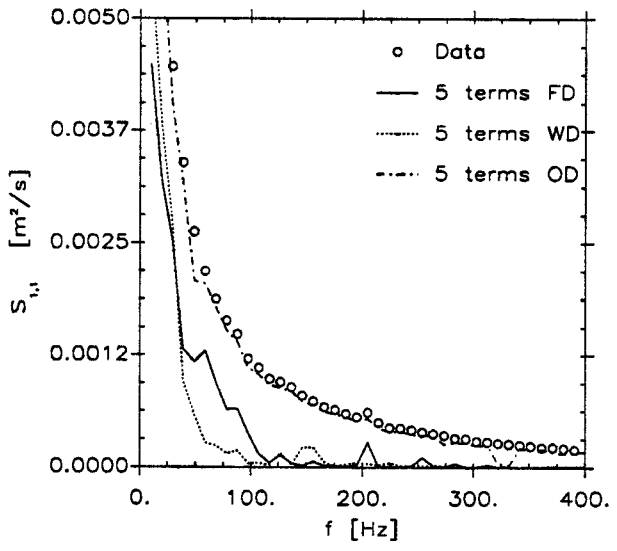

Figure 6.69: Reconstruction of axial velocity component PSD at 40% pitch.

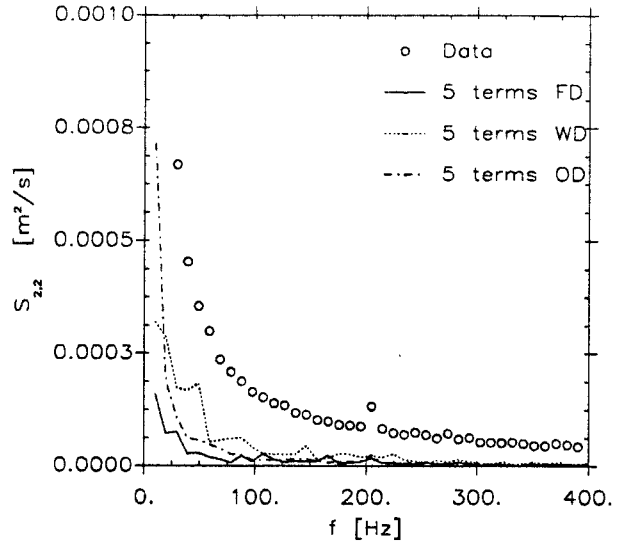

Figure 6.70: Reconstruction of azimuthal velocity component PSD at 40% pitch.

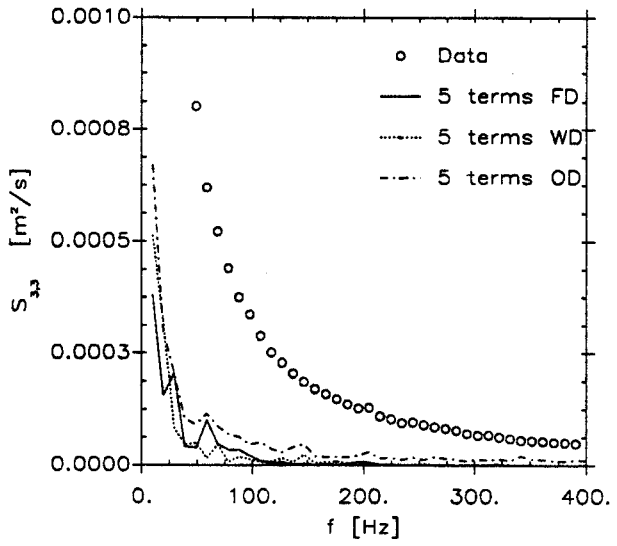

Figure 6.71: Reconstruction of radial velocity component PSD at 40% pitch.

Chapter 7

Conclusions and Recommendations

A more complete understanding of complex turbine flowfields is needed in order to improve on the performance of mean-flow based turbine designs. To understand what is happening in the turbine flowfield, it is essential to know how the turbulence is generated, how it propagates and how it modifies the flow. While identifying turbulence contributions to signals, standard averaging techniques (such as phase locked averaging) leave unanswered questions regarding the spatial and temporal character of the turbulence itself. It was hypothesized at the beginning of this investigation that there exist typical wake and passage flows which possess characteristics important to the rotor dynamics. An investigation of the behavior and content of the hypothesized coherent structures comprising the turbulence contribution to the turbine flowfield was therefore undertaken in this study.

The proper orthogonal decomposition (POD), a technique proposed by Lumley (1967) for the eduction of coherent structures, was selected for this study. The coherent structures are identified by the POD as the set of orthonormal functions (modes) for which the mean square projection on the flowfield is maximized. This method of structure identification was chosen because the dynamical evolution of the modes can be examined and calculated (v. George 1988 and references therein).

The POD was applied to three component triple-wire probe spectral tensor measurements of a large-scale annular stator model exit flowfield. This study represents the first application of the orthogonal decomposition to directly measured three component data, and one of the first application to an applied engineering flow.

The original research proposed to use cross-wire probes and measure the entire field in a plane at the stator exit. However, since the radial flow component was not negligible or uniform, especially in the wake region, it was decided to use triple-wire probes and directly measure all three velocity components. This decision was not without cost however, as long delays in the experimental program were a consequence. As a result of these delays, together with the expiration of funding, the multi-point triple-wire probe measurements had to be limited to a midspan traverse of two probes across one stator pitch at one axial location 10% axial chord downstream of the stator trailing edge.

The POD was applied first to the entire set of 1089 cross-spectral estimates representing the passage exit midspan. Reconstructions of the power spectral densities were examined to gauge the merit of the POD modes to characterize the energy of the flowfield. Only a few POD modes were required to represent a significant amount of the energy of the field (3 terms for over 50% energy representation). Low frequency (below 200 Hz) spikes were found in the eigenmodes at various frequencies and were attributed to either inlet flow disturbances or meandering of coherent structures generated by the blade row. Decomposition of other transverse measurement sets would have assisted in identifying the origin of such spikes. Outside of the wake region, the modes typically represent the energy at progressively higher frequencies and thus capture the large scale structures in the lowest modes. Within the wake however, the POD modes very effectively captured the high frequency, high energy content. The eigenspectra for the full domain decomposition indicate that the first four modes essentially accomodated completely the high energy associated with the wake.

Moin and Moser (1989) and George and Glauser (1991) suggested applying the POD to subdomains with inherently different flow regimes in order to increase the convergence rate of the energy representation by the modes. This premise was based on Lumley's (1967) argument that the convergence of the expansion in terms of energy is a function of the spatial extent divided by the integral

scale. In this study, outside of the hub and shroud boundary layers, the passage exit flow consists primarily of two domains, the wake and the outer flow regions. Because of the large difference in scales between these regions, the orthogonal decomposition was applied separately to the two domains in order to see if better convergence of the expansion could be achieved. Convergence of the POD was found to be affected by the flow regime contained in the domain. The eigenspectra and eigenmodes of the subdomain which included the wake region had a similar character to those of the full domain POD although their convergence was significantly better (2 terms for over 50% energy representation). By applying the POD to a subdomain which excluded the wake, the convergence of the subdomain energy representation was indicative of the expansion of a quasi-homogeneous field (v. Chambers et al. 1988). The first mode represented only 17% of the domain energy and four modes were required to provide over 50% energy reconstruction.

Since the POD eigenmodes have been shown to characterize a significant portion of the stator exit flowfield energy (for the measurements of this study), it would be useful to determine the dynamics of the structures which should relate to the downstream blade row dynamics. The dynamics of a flowfield could be examined by reconstructing the instantaneous flowfield in terms of the POD modes (Eq. (2.7)) and tracking the transfer of energy among the eigenmodes (v. George 1988 and George and Glauser 1991). The data necessary for such a calculation using one dimensional flowfield cuts would have to be taken with rakes of subminiature probes. An alternative approach would be the application of the orthogonal decomposition to numerically simulated data.

The use of dynamical systems theory in conjunction with Galerkin projection of experimentally determined modes on the Navier Stokes equations has been shown (v. Sirovich 1987, Aubrey et al. 1988 and Glauser et al. 1989) to be an effective means for investigating the dynamics of the flowfield coherent structures. This method reduces the problem of finding the complex coefficients for the velocity reconstruction (Eq. (??)) from a set of linear ordinary differential equations. To apply this analysis, it is useful to apply the decomposition to the cross-spectral tensor defined in terms of the cross-correlation tensor (mean in) as opposed to the covariance tensor (fluctuations only). In this study the decomposition was applied only to the fluctuating field since solving the eigensystem

problem can easily be repeated with the entire flowfield at a later time.

To summarize, additional data is needed to ascertain the origin of coherent flowfield structures in the stator exit flowfield and to determine their subsequent dynamics. With the increased computational capability, a combined experimental and computational effort is most likely to achieve the desired objective of not only identifying proper orthogonal decomposition eigenfunctions but also their dynamics and effects on downstream blade row dynamics.

Appendix A

POD Formulation

The extremization of λ in Eq. (2.3) can be found by considering a function in the neighborhood of the maximizing function $\phi_i(\cdot)$

$$\hat{\phi}_i(\cdot) = \phi_i(\cdot) + \epsilon\eta(\cdot) \tag{A.1}$$

where ϵ is an infinitesimal parameter and $\eta(\cdot)$ is well behaved with appropriate boundary conditions. With substitution of Eq. (A.1) with the appropriate conjugation and independent variable into Eq. (2.3), the extremum can be found using the usual method of differential calculus, ie. by setting

$$\left(\frac{d\lambda}{d\epsilon}_{\epsilon=0}\right) = 0. \tag{A.2}$$

Evaluation of Eq. (A.2) for λ given by Eq. (2.3) yields

$$\int\int [\phi_i^*(\cdot)\eta(\cdot') + \phi_i(\cdot')\eta^*(\cdot)]R_{i,j}(\cdot,\cdot')d(\cdot)d(\cdot') - \lambda\int [\phi_j(\cdot)\eta^*(\cdot) + \phi_j^*(\cdot)\eta(\cdot)]d(\cdot) = 0. \tag{A.3}$$

Substitution of $(\hat{\cdot}) = (\cdot)$ and $(\hat{\cdot}') = (\cdot')$ followed by the substitutions $(\cdot) = (\hat{\cdot}')$ and $(\cdot') = (\hat{\cdot})$ effectively switches the independent variable in an expression. Applying these substitutions and using the identity

$$R_{i,j}(\cdot',\cdot) = R_{i,j}^*(\cdot,\cdot') \tag{A.4}$$

for the first term only in Eq. (A.3) yields

$$\int \left\{ \int [\phi_i^*(\cdot')\eta(\cdot)R_{i,j}^*(\cdot,\cdot') + \phi_i(\cdot')\eta^*(\cdot)R_{i,j}(\cdot,\cdot')]d(\cdot') - \lambda[\phi_j(\cdot)\eta^*(\cdot) + \phi_j^*(\cdot)\eta(\cdot)] \right\} d(\cdot) = 0. \tag{A.5}$$

Since the integral over $(\cdot)$ is for arbitrary bounds, the integrand is itself zero. Factoring $\eta(\cdot)$ and $\eta^*(\cdot)$ out of the resulting equation yields

$$\eta(\cdot)[\int \phi_i^*(\cdot')R_{i,j}^*(\cdot,\cdot')d(\cdot') - \lambda\phi_j^*(\cdot)] + \eta^*(\cdot)[\int \phi_i(\cdot')R_{i,j}(\cdot,\cdot')d(\cdot') - \lambda o_j(\cdot)] = 0 \qquad \text{(A.6)}$$

which is the sum of complex conjugates. Since the auxiliary function $\eta(\cdot)$ is well behaved and non-zero, the bracketed terms must themselves be identically zero. Further manipulation of either term yields the integral equation

$$\int R_{i,j}(\cdot,\cdot')\phi_j(\cdot')d(\cdot') = \lambda\phi_i(\cdot) \qquad \text{(A.7)}$$

which can be solved for the deterministic, but randomly distributed candidate functions ϕ.

Bibliography

Adrian, R.J., 1979, "Conditional Eddies in Isotropic Turbulence," Physics of Fluids, Vol. 22, pp. 2065-2070.

Andreopoulos, J., 1983, "Improvements of the Performance of Triple Hot Wire Probes," Rev. Sci. Instrum., Vol. 54(6), pp. 733-740.

Andreopoulos, J., 1983, "Statistical Errors Associated with Probe Geometry and Turbulence Intensity in Triple Hot-Wire Anemometry," J. Phys. E: Sci. Instrum., Vol. 16, pp. 1264-1271.

Antonia, R.A., 1981, "Conditional Sampling in Turbulence Measurement," Ann. Rev. Fluid Mech., Vol. 13, pp. 131-156.

Aubry, N., Holmes, P., Lumley, J.L. and Stone, E., 1988, "The Dynamics of Coherent Structures in the Wall Region of a Turbulent Boundary Layer," J. Fluid Mechanics, Vol. 192, pp. 115-173.

Bailey, D.A., 1979, "Study of Mean- and Turbulent- Velocity Fields in a Large-Scale Turbine-Vane Passage," NASA Contractor Report 3076.

Baker, C.T.H., 1977, *The Numerical Treatment of Integral Equations*, Clarendon Press, Oxford.

Bakewell, H.P., and Lumley, J.L., 1967, "Viscous Sublayer and Adjacent Wall Region in Turbulent Pipe Flow," The Physics of Fluids, Vol. 10, No. 9, pp. 1880-1889.

Beuther, P.D., 1980, *Experimental Investigation of the Axisymmetric Turbulent Buoyant Plume*, Ph.D. Dissertation, SUNY at Buffalo.

Beuther, P.D., Shabbir, A. and George, W.K., 1987, "X-Wire Response in Turbulent Flows of High-Intensity Turbulence and Low Mean Velocities," ASME Symposium on Thermal Anemometry - FED - Vol. 53, Ed. D.E. Stock.

Blair, M.F., Dring, R.P. and Joslyn, H.D., 1989a, "The Effects of Turbulence and Stator/Rotor Interactions on Turbine Heat Transfer: Part I-Design Operating Conditions," ASME J. Turbomachinery,

Vol. 111, pp. 87-96.

Blair, M.F., Dring, R.P. and Joslyn, H.D., 1989b, "The Effects of Turbulence and Stator/Rotor Interactions on Turbine Heat Transfer: Part II-Effects of Reynolds Number and Incidence," ASME J. Turbomachinery, Vol. 111, pp. 97-103.

Bruun, H.H., 1979, "Interpretation of Hot-Wire Probe Signals in Subsonic Airflows," J. Phys. E: Sci. Instrum., Vol. 12, pp. 1116-1128.

Butler,T.L. and Wagner, J.W., 1983, "Application of a Three-Sensor Hot-Wire Probe for Incompressible Flow," AIAA Journal, Vol. 21, No. 5, pp. 726-732.

Chambers, D.H., Adrian, R.J., Moin, P., Stewart, D.S. and Sung, H.J., 1988, "Karhunen-Loéve Expansion of Burgers' Model of Turbulence," Phys. Fluids, Vol. 31 (9), pp. 2573-2582.

Champagne, F.H., Sleicher, C.A. and Wehrmann, O.H., 1967, "Turbulence Measurements with Inclined Hot-Wire, Part 1. Heat Transfer Experiments with Inclined Hot-Wire," J. Fluid Mech. 28 Part 1, pp. 153-175.

Dring, R.P., Joslyn, H.D. and Blair, M.F., 1987, "The Effects of Inlet Turbulence and Rotor/Stator Interactions on the Aerodynamics and Heat Transfer of a Large-Scale Rotating Turbine Model; IV-Aerodynamic Data Tabulation," NASA Contractors Report 179469.

Dring, R.P., Joslyn, H.D., Hardin, L.W. and Wagner, J.H., 1982, "Turbine Rotor-Stator Interaction," ASME J. Engineering for Power, Vol. 107, pp. 729-742.

Dring, R.P., Blair, M.F., Joslyn, H.D., Power, G.D. and Verdon, J.M., 1986, "The Effects of Inlet Turbulence and Rotor/Stator Interactions on the Aerodynamics and Heat Transfer of a Large-Scale Rotating Turbine Model; I-Final Report," NASA Contractor Report 4079.

Dunn, M.G., 1986, "Heat-Flux Measurements for the Rotor of a Full-Stage Turbine: Part I-Time-Averaged Results," ASME Paper No. 86-GT-77.

Dunn, M.G., George, W.K., Rae, W.J., Woodward, S.H., Moller, J.C. and Seymour, P.J., 1986, "Heat Flux Measurements for the Rotor of a Full-Stage Turbine: Part II-Description of Analysis Technique and Typical Time-Resolved Measurements," ASME Paper No. 86-GT-78.

Dunn, M.G., Bennett, W., DeLaney, R. and Rao, 1990, "Investigation of Unsteady Flow Through a Transonic Turbine Stage, Parts II and III: Comparison of Time-Averaged and Phase Resolved Heat-Flux Data on Blade and Vane with Predictions," AIAA Paper No. 90-2409 and 90-2410.

Evans, R.L., 1975, "Turbulence and Unsteadiness Measurements Downstream of a Moving Blade

Row," ASME J. Engineering for Power, pp. 131-139.

Fabris, G., 1978, "Probe and Method for Simultaneous Measurement of "True" Instantaneous Temperature and Three Velocity Components in Turbulent Flow," Rev. Sci. Instrum., Vol. 49, No. 5.

George, W.K., 1988, "Insight into the Dynamics of Coherent Structures from a Proper Orthogonal Decomposition," Proceedings Symposium on Near Wall Turbulence, Dubrovnic, Yugoslavia, May 16-20.

George, W.K., Beuther, P.D. and Lumley, J.L., 1978, "Processing of Random Signals," Proceedings of the Dynamic Flow Conference.

George, W.K., Beuther, P.D. and Shabbir, A., 1987, "Polynomial Calibrations for Hot Wires in Thermally-Varying Flows," ASME Symposium on Thermal Anemometry - FED - Vol. 53, pp. 1-6.

George, W.K. and Glauser, M.N., 1991, "Flow Structure Identification From Multi-Point Measurements," 2nd World Conference on Heat Transfer, Fluid Mechanics and Thermodynamics, Dubrovnic, Yugoslavia, June.

Glauser, M.N., 1987, *Coherent Structures in the Axisymmetric Turbulent Jet Mixing Layer*, Ph.D. Dissertation, SUNY at Buffalo

Glauser, M., Zheng, X. and Doering, C.R., 1989, *Turbulence and Coherent Structures*, Kluwer Academic Publishers.

Gorton, C.A. and Lakshminarayana, B., 1976, "A Method of Measuring the Three-Dimensional Mean Flow and Turbulence Quantities Inside a Rotating Turbo-Machinery Passage," ASME J. Engineering for Power, pp. 137-146.

Graham, R.W., 1980, "Fundamental Mechanisms That Influence the Estimate of Heat Transfer to Gas Turbine Blades," Heat Transfer Engineering, Vol. 2, No. 1, pp. 39-47.

Graziani, R.A., Blair, M.F., Taylor, J.R. and Mayle, R.E., 1980, "An Experimental Study of Endwall and Airfoil Surface Heat Transfer in a Large Scale Turbine Blade Cascade," ASME J. Engineering for Power, Vol. 102, pp. 257-267.

Gregory-Smith, D.G. and Graves, C.P., 1983, "Secondary Flows and Losses in a Turbine Cascade," Viscous Effects in Turbomachines, AGARD CP 351.

Guenette, G.R., Epstein, A.H., Giles, M.B., Haimes, R. and Norton, R.J.G., 1989, "Fully Scaled Transonic Turbine Rotor Heat Transfer Measurements," ASME J. Turbomachinery, Vol. 111, pp. 1-7.

Herzog, S., 1986, *The Large Scale Structure in the Near-Wall Region of Turbulent Pipe Flow*, Ph.D. Dissertation, Cornell University.

Hinze, J.O., 1959, *Turbulence*, McGraw-Hill, New York.

Hodson, H.P., 1985, "Measurements of Wake Generated Unsteadiness in the Rotor Passages of Axial Flow Turbines," ASME J. Engineering for Gas Turbines and Power, Vol. 107, pp. 467-476.

Jorgenson, F.E., 1971, "Directional Sensitivity of Wire and Fiber-film Probes," DISA Information, No. 11, pp. 31-37.

Junkins, J.L., 1978, *An Introduction to Optimal Estimation of Dynamical Systems*, Sijthoff and Noordhoff, Alphen aan den Rijn, The Netherlands.

Ketter, R.L. and Prawel, S.P., 1969, *Modern Methods of Engineering Computation*, McGraw-Hill Book Co., New York.

King, L.V., 1914, "On the Convection of Heat From Small Cylinders in a Stream of Fluid: Determination of the Convection Constants of Small Platinum Wires with Applications to Hot-Wire Anemometry," Phil. Soc. A., 214, pp. 373-432.

LeBoeuf, R.L., 1990, "A New Approach to the Calibration of Non-Orthogonal Triple-Wire Probes," Presented at American Physical Society, Forty-Third Annual Meeting of the Division of Fluid Dynamics, Cornell University.

LeBoeuf, R.L. and George, W.K., 1990, "The Calibration and Use of Non-Orthogonal Cross-Wire Probes," ASME FED-Vol. 97, The Heuristics of Thermal Anemometry, Eds. D.E. Stock, S.A. Sherif and A.J. Smits, pp. 59-63.

Lekakis, I.C., Adrian, R.J. and Jones, B.G., 1989, "Measurement of Velocity Vectors With Orthogonal and Non-Orthogonal Triple-Sensor Probes," Experiments in Fluids, Vol. 7, pp. 228-240.

Loéve, M., 1955, *Probability Theory*, Van Nostrand, New York.

Lovitt, W.V., 1950, *Linear Integral Equations*, Dover Publications Inc., New York.

Lumley, J.L., 1967, "The Structure of Inhomogeneous Turbulent Flows," *Atmospheric Turbulence and Radio Wave Propagation*, Nauka, Moscow.

Lumley, J.L., 1970, *Stochastic Tools in Turbulence*, Academic Press Inc., New York.

Mayle, R.E., 1991, "The Role of Laminar-Turbulent Transition in Gas Turbine Engines," ASME Paper No. 91-GT-261, Presented at the International Gas Turbine and Aeroengine Congress and

Exposition, Orlando, Florida, June 3-6.

Moin, P. and Moser, R.D., 1989, "Characteristic-Eddy Decomposition of Turbulence in a Channel," J. Fluid Mech., Vol. 200, pp. 471-509.

Moore, J. and Adhye, R.Y., 1985, "Secondary Flows and Losses Downstream of a Turbine Cascade," ASME J. Engineering for Gas Turbines and Power, Vol. 107, pp. 961-968.

Moustapha, S.H., Paron, G.J. and Wade, J.H.T., 1985, "Secondary Flows in Cascades of Highly Loaded Turbine Blades," ASME J. Engineering for Gas Turbines and Power, Vol. 107, pp. 1031-1038.

Oppenheim, A.V. and Willsky, A.S., 1983, *Signals and Systems*, Prentice-Hall, Englewood Cliffs, New Jersey.

Raj, R. and Lakshminarayana, B., 1973, "Characteristics of the Wake Behind a Cascade of Airfoils," J. Fluid Mechanics, Vol. 61, Part 4, pp. 707-730.

Sharma, O.P., Butler, T.L., Joslyn, H.D. and Dring, R.P., 1985, "Three-Dimensional Unsteady Flow in an Axial Flow Turbine," AIAA J. Propulsion and Power, Vol. 1, No. 1, pp. 29-38.

Sidall, R.G. and Davies, T.W., 1972, "An Improved Response Equation for Hot-Wire Anemometry," Int. J. Heat Mass Trans., 15, pp. 367-368.

Sieverding, C.H., 1985, "Recent Progress in the Understanding of Basic Aspects of Secondary Flows in Turbine Blade Passages," ASME J. Engineering for Gas Turbines and Power, Vol. 107, pp. 248-257.

Sieverding, C.H., Van Hove, W. and Boletis, E., 1984, "Experimental Study of the Three-Dimensional Flow Field in an Annular Turbine Nozzle Guidevane," ASME J. Engineering for Gas Turbines and Power, Vol. 106, pp. 437-444.

Sirovich, L., Maxey, M and Tarman, H., 1987, "Analysis of Turbulent Thermal Convection," 6th Symposium on Turbulent Shear Flows.

Smith, B.T., Boyle, J.M., Dongarra, J.J., Garbow, B.S., Klema, V.C. and Moler, C.B., 1976, *Matrix Eigensystem Routines - EISPACK Guide*, Springer-Verlag, New York.

Swaminathan, M.K., Rankin, G.W. and Sridhar, K., 1984, "Some Studies on Hot-Wire Calibration Using Monte Carlo Technique," J. Phys. E: Sci. Instrum., 17, pp. 1148-1151.

Tan-atichat, J. and George, W.K., 1985, "Use of Computer for Data Aquisition and Processing," *Handbook of Fluids and Fluid Machinery*, John Wiley & Sons, Inc., Allen E. Fuhs, ed.

Tennekes, H. and Lumley, J.L., 1972, *A First Course in Turbulence*, The MIT Press, Cambridge, Massachussettes.

Touloukian, Y.S., Saxena, S.C. and Hestermans, P., 1975, *Viscosity*, IFI/Plenum, New York.

Touloukian, Y.S., Liley, P.E. and Saxena, S.C., 1970, *Thermal Conductivity: Nonmetallic Liquids and Gases*, IFI/Plenum, New York.

Treaster, A.L. and Houtz., H.E., 1986, "Fabricating and Calibrating Five-Hole Probes," presented at the AIAA/ASME 4th Fluid Mechanics, Plasma Dynamics, and Lasers Conference, Atlanta, Georgia, May 11-14.

Treaster, A.L. and Yocum, A.M., 1979, "The Calibration and Application of Five-Hole Probes," ISA Transactions, Vol. 18, No. 3.

Ukeiley, L., Varghese, M., Glauser, M. and Valentine, D., 1991, "An Examination of Coherent Structures in a Lobed Mixer Using Multifractal Measures in Conjunction with the Orthogonal Decomposition," AIAA Paper 91-0521.

Ukeiley, L., Wick, D. and Glauser, M., 1990, "A Novel Hot-Wire Rake Design," ASME FED-Vol. 97, The Heuristics of Thermal Anemometry, Eds. D.E. Stock, S.A. Sherif and A.J. Smits, pp. 87-92.

Webster, C.A.G., 1962, "A Note on the Sensitivity to Yaw of a Hot-Wire Anemometer," J. Fluid Mech., 13, pp. 307-312.

Welz, J.P., 1986, "An Algorithm for Using the Five-Hole Probe in the Nonnulled Mode," presented at the AIAA/ASME 4th Fluid Mechanics, Plasma Dynamics, and Lasers Conference, Atlanta, Georgia, May 11-14.